SCHALLAMACH WAVES AND FRICTION-INDUCED SELF-OSCILLATIONS IN A PROTOTYPICAL BELT DRIVE SYSTEM

A Dissertation
Presented to
The Academic Faculty

by

Yingdan Wu

In Partial Fulfillment
of the Requirements for the Degree
Doctor of Philosophy in the
George W. Woodruff School of Mechanical Engineering

Georgia Institute of Technology
August 2020

COPYRIGHT © 2020 BY YINGDAN WU

SCHALLAMACH WAVES AND FRICTION-INDUCED SELF-OSCILLATIONS IN A PROTOTYPICAL BELT DRIVE SYSTEM

Approved by:

Dr. Michael Varenberg, Co-Advisor
School of Mechanical Engineering
Georgia Institute of Technology

Dr. Michael J. Leamy, Co-Advisor
School of Mechanical Engineering
Georgia Institute of Technology

Dr. Itzhak Green
School of Mechanical Engineering
Georgia Institute of Technology

Dr. Aldo A. Ferri
School of Mechanical Engineering
Georgia Institute of Technology

Dr. Matthew Brake
Department of Mechanical Engineering
Rice University

Date Approved: May 19th, 2020

In memory of Zifen Han, Wenlong Wu and Yuqin Sun

ACKNOWLEDGEMENTS

First of all, I wish to thank my advisors Dr. Varenberg and Dr. Leamy for offering me the opportunity to do research under their guidance four years ago. I am so lucky that I have been able to learn all the merits of an outstanding scholar from both of them day by day for the last four years. Throughout this lovely journey, they have always been patient, inspiring and insightful advisors, as well as caring, loving and encouraging mentors. I really appreciate all the time, discussions and passion they have contributed to develop me into a researcher. Without their guidance, I do not believe I would have been able to successfully navigate the completion of my PhD.

In addition, I am grateful to my reading committee: Dr. Itzhak Green, Dr. Aldo A. Ferri and Dr. Matthew Brake for sharing their breadth of expertise and knowledge during the completion of the work contained in this dissertation. Dr. Green and Dr. Ferri also helped me develop a great foundation in tribology and dynamics, respectively, in their courses during the first year in graduate school. Moreover, Dr. Brake provided insightful idea on the measurement of shear stress via digital image correlation, which has been used in the follow-up project. I would also like to thank the members of the Montgomery Machining Mall, Electronics Lab and Invention Studio, specifically Steven Sheffield, Scott Elliot, Louis Boulanger, Nathan Mauldin, Matthew Carroll and Kyle French, for the help provided in fabricating the experimental setup and specimens presented in this dissertation. Additionally, I am also indebted to the Dr. Jeffrey A. Donnell for his patient instructions and kind helps on the language issues with my manuscripts.

I would also like to thank National Science Foundation for the funding support during the first three years of my graduate studies. Additionally, I would like to extend my thanks to Dr. Wayne Whiteman, Dr. David E Torello and Dr. David R Smith for offering me the teaching assistant opportunities with financial support for the last year of my graduate studies. All of these supports helped me to devote myself to the completion of the work in this dissertation. For that I am very grateful.

Sincere appreciation is also expressed to my friends who are the ones that have made my time here more delightful. Firstly, the members of Dr. Varenberg's group have always been there for me while I was experiencing ups and downs in research and life. I am grateful for those time spent with Jaekang Kim, Ye Qi and Yuan Gao. Without the coffee breaks or doing work out with Jaekang, my time in graduate school would have been a lot harder. Additionally, I am thankful and appreciative of the help from the members of Dr. Leamy's group: Dr. Amir Darabi, Dr. Justin Wilbanks, Dr. Matt Fronk and Lezheng Fang, who made conference experience more pleasant. Outside the lab groups, I have also met brilliant and fantastic people. I am thankful for the discussions about research and life with Huaidong Yang, who, as the only tribology student outside our group, has always been a great roommate, classmate and friend for me. I am also thankful for the adventures around Quebec and Los Angela that I had with Yiwei Xia and Lezheng during conference time. I am also grateful for the help from Ye, Jaekang, Yutong Guo and Scott Schoen during qualifying exams. I am also grateful for the weekly soccer games with Dudong Feng, Chao Li and the whole Local Panda team that keep me well-being both mentally and physically. Additionally, I want express me especial appreciation to Huaidong, Jiangpeng

Pan, Zixiao Wang and Chenan Ni for the pleasant time spent together when we first came here.

Lastly, I wish to express my deepest love and appreciation to my family for their endless support and love; especially, my mother, Yurong Sun, and father, Shucai Wu. My parents have always been there for me and encouraged me to work hard throughout my life time. I am also thankful to my grandfather, Zicai Sun, for his guidance for my pursuit of a degree in mechanical engineering. I am eager to see what awaits me in the future with the knowledge that I have gained here at Georgia Institute of Technology.

TABLE OF CONTENTS

LIST OF TABLES

LIST OF FIGURES

LIST OF SYMBOLS AND ABBREVIATIONS

A Cross sectional area of the belt, mm^2

a Lattice constant, mm

$A_{T,de}$ Amplitude of the detachment event-related fluctuations in tension difference signal, N

$A_{T,po}$ Amplitude of the pulley oscillation-related fluctuations in tension difference signal, N

AR Aspect ratio of the pattern projections

A_s Amplitude of the belt extension, μm

A_t Tension member cross section area, mm^2

$A_{\alpha, de}$ Amplitude of the detachment event-related fluctuations in angular velocity signal, rad s^{-1}

$A_{\alpha, po}$ Amplitude of the pulley oscillation-related fluctuations in angular velocity signal, rad s^{-1}

B Width of the belt, mm

c_1 Damping coefficient of the pulley, kg s^{-1}

c_2 Damping coefficient of the belt, kg s^{-1}

D Diameter of the inscribed circle of the pattern, mm

E Young's modulus of PDMS, MPa

E' Storage modulus of the PDMS, MPa

E'' Loss modulus of the PDMS, MPa

E_t Elastic modulus of tension member, GPa

F_T Tension force in the belt, N

F_S Shear force in the belt, N

F_{TS} Tension at the slack span, N

F_{TT} Tension at the tight span, N

ΔF_{T_dw} Tension fluctuation, N

f_{dw} Detachment wave frequency, Hz

$f_{\mathrm{T,de}}$ Frequency of the detachment event-related fluctuations in tension difference signal, Hz

$f_{\mathrm{T,po}}$ Frequency of the pulley oscillation-related fluctuations in tension difference signal, Hz

$f_{\alpha,\,\mathrm{de}}$ Frequency of the detachment event-related fluctuations in angular velocity signal, Hz

$f_{\alpha,\,\mathrm{po}}$ Frequency of the pulley oscillation-related fluctuations in angular velocity signal, Hz

G Shear modulus of the belt, MPa

g Gravitational acceleration constant, m s^{-2}

h The height of the pattern projection, mm

H_0 Work of adhesion, mJ m^{-2}

I Moment of inertia of the pulley, kg·mm^2

l_{01} Initial length of exit span of the belt, m

l_{02} Initial length of entry span of the belt, m

M The mass of the tension weight, kg

m The mass of the torque weight, kg

M_S Moment at the slack span of the belt, N·m

M_T Moment at the tight span of the belt, N·m

R Radius of the pulley, m

R_{a} The standard roughness average of profile irregularities, μm

$s(t)$ Detachment-driven extension in the exit zone, m

S_{m} The mean spacing of profile irregularities, μm

t Thickness of the belt, mm

t_n Normal traction at the belt/pulley interface, N

t_t	Tangential (shear) traction at the belt/pulley interface, N
T_{de}	The detachment wave-related component of the fluctuations in tension difference
T_{po}	The pulley oscillation-related component of the fluctuations in tension difference
V	Driving speed, mm s^{-1}
v_0	Characteristic crack speed, μm s^{-1}
$\overline{W_V}$	The dissipated energy due to volumetric hysteresis per unit volume, J m^{-3}
$x(t)$	The linear displacement of the exiting span of the belt, m
$y(t)$	The computed linear displacement of the tension weight, m
α	Exponent describing the relation between the energy change and the crack propagation speed
$\alpha(t)$	The computed angular displacement of the pulley, rad
β	The slip arc angle, °
$\delta(t)$	The elongation of the exiting span of the belt, m
ε_a	The given strain value for which the energy loss is calculated
μ_k	The kinetic friction coefficient between belt and pulley
μ_s	The static friction coefficient between belt and pulley
ν	Poisson's ratio
γ_{a_en}	Max. shear strain at the entry zone
γ_{a_ex}	Max. shear strain at the exit zone

SUMMARY

The high adhesive friction between an elastomer and its counterpart generally impedes sliding in the accepted sense. Instead, displacement is accommodated by Schallamach waves of detachment, which are surface wrinkles that move across the contact zone. However, this has received little research attention in belt drive systems; sliding-based friction models are invariably employed for belt drive mechanics studies. In light of this discrepancy, the rolling contact mechanics in a simple flat belt drive will be explored by considering Schallamach waves of detachment, with particular focus as follows. 1) A thorough understanding of the mechanism of detachment events and friction generated at the belt-pulley interface will be developed. 2) The characteristics of detachment wave-induced oscillations, including the belt and pulley's oscillations, will be studied, focusing on their dependence on driving speed, loading conditions and the system's inertia. Also, it is of interest to examine these waves and the global system oscillations in a fully-coupled manner such that 3) downstream effects of detachment events couple to the dynamic response of the belt drive system, and 4) the system's dynamics couple to the generation of detachment waves. Further, the research intends 5) to propose a rolling friction model for elastomers, capable of computing mechanical energy losses associated with the contact instabilities. 6) A novel surface design will be examined to check the ability to influence, control and tailor the presence of detachment wave-induced oscillations in belt drives. 7) Belts incorporating tensile cords, which are more comparable to belts used in industry, will be examined to find whether detachment waves are universal in belt drive systems.

CHAPTER 1. INTRODUCTION

1.1 Motivation

Belt drives find applications in manufacturing processes and power transmission at nearly every scale. Belts (including poly-V, V and flat) are used for mechanical power transmission in manufacturing machines and equipment, typically to connect an electric motor to various driven shafts in machines such as printing presses, pumps, diesel engines for power generation, compressors, mixers, etc. Belt drives are also used as accessory drives for cars and trucks; data tape reels and consumer devices powered by electric motors; household appliances (such as washing machines and dryers) and garden equipment; and as synchronous belts in precision positioning systems. They are also used in material/people transport applications such as conveyor belts and elevators. Belt length can vary from a few centimeters in electronic equipment, to 31 kilometers for the longest mining conveyor belt. Although properly installed and maintained belt-drives are efficient and can preserve up to 95% of the input energy [1], their efficiency and performance are affected by complex system dynamics arising primarily from excitation at the belt-pulley interface, fluctuations in the pulleys' angular velocities and span tensions, and belt misalignment. These in turn lead to energy loss, undesired vibration and noise, wear, and speed loss between the driver and driven pulleys. For these reasons, it is critical to understand belt-drive mechanics/dynamics for robust system design and energy efficiency.

The relative displacement between an elastomer and its counterpart is often accommodated by Schallamach waves of detachment [2], instead of stable sliding. These waves should also affect the belt drive system, which has long been known to involve

relative displacement over part of the belt-pulley interface [3]. However, though the investigation of belt drives has been extensive, contact instabilities in belt drive systems have received little research attention. As a consequence, traditional stable sliding-based models of friction are invariably employed in the analysis of the belt drives. A detachment wave-informed study on belt drive systems needs to be conducted to uncover the corresponding contact mechanics and the system's dynamic response. A simple belt drive with two pulleys (Fig. 1-1) will be the prototypical system explored throughout this research.

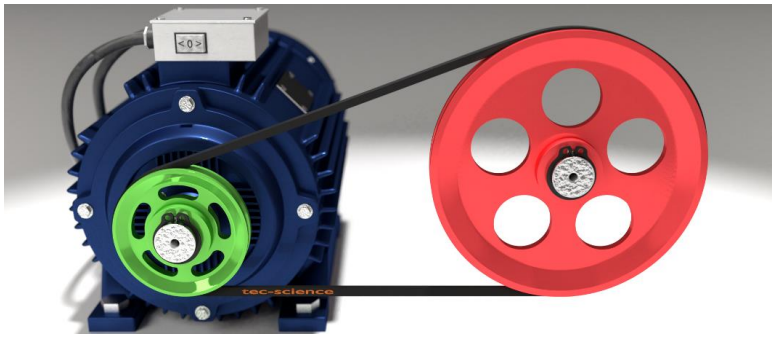

Figure 1-1. Prototypical two-pulley belt drive.

1.2 Belt Drive Mechanics

The efficiency of belt drives vary with the operating torque of the drive and the resulting amount of belt slip incurred in the belt-pulley contact region. It is critical to understand belt drive mechanics/dynamics and friction behavior in order to achieve a design which optimizes this efficiency while providing the requisite power transmission with minimal noise and vibration. It is also critical to impart robustness in the design of belt drives in order to prevent loss of efficiency over time, and worse scenarios. For most belts, the belt cross-section mainly consists of stiff steel, polyester, aramid or Kevlar cords

along the length of the belt and a rubber (elastomer) matrix (or carcass) in which the cords are embedded (Fig. 1-2). The rubber matrix provides the frictional interface between the belt and the pulleys through which tangential forces are transmitted. In order to increase the power transmission capacity of V-belts, multiple belts are installed on the same pulley to share load. The evolution of this concept led to the development of poly-V ribbed belts (Fig. 1-2c) which integrate the features of both flat belts and V-belts.

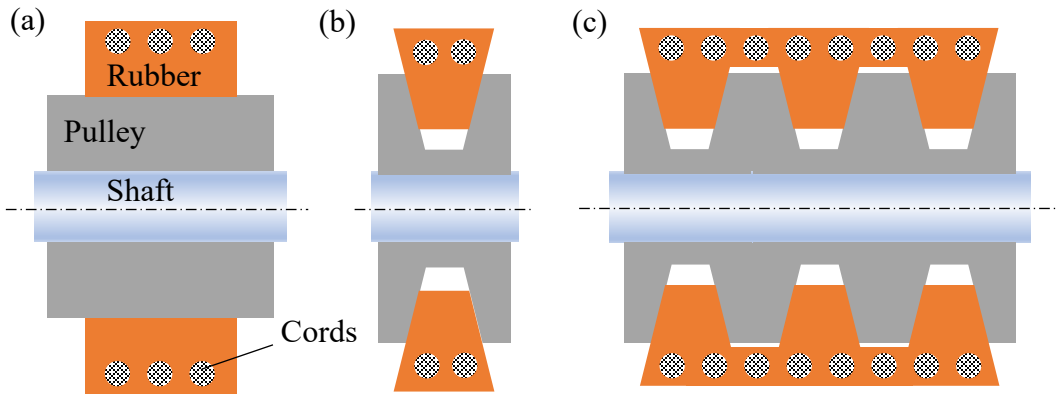

Figure 1-2. Typical cross-section of (a) flat, (b) V and (c) poly-V ribbed belts.

The literature regarding belt-drive mechanics is extensive; two of the earliest belt-pulley mechanics studies were Leonard Euler's analysis of a belt wrapped around a fixed pulley [4] and Grashof's study of the frictional mechanics of belt-drives under steady operation [5]. These studies together developed the classical belt creep theory in which a Coulomb friction law governs the belt pulley contact, and the belt is treated as a flexible one-dimensional string adhering to a pulley in an initial adhesion arc and creeping longitudinally against the pulley in a subsequent slip arc (Fig. 1-3).

In classical creep theory, the belt tension remains constant in the adhesion arc (and the friction force is zero), and all tension transition occurs in the slip arc due to microslip

of the belt against the pulley. Due to fully developed friction forces in this slip zone, the tension change is an exponential function of the arc length s such that the tension change from tight F_T to slack F_S is given by the 'capstan' formula $F_S = F_T e^{-\mu\varphi_s}$ where μ denotes the friction coefficient and φ_s denotes the extent of the slip arc. Review papers on the belt drive mechanics and belt creep theory are given by Fawcett [6] and Johnson [7]. Belt creep theory was updated with inertial effects by Bechtel *et al.* [8]. Townsend and Salisbury [9] derived the power loss expression and the efficiency limit of a belt drive based on the belt creep theory. Leamy and Wasfy [10] used a creep rate dependent friction law to predict the friction force and belt tension distribution over the pulleys. This creep-rate-dependent friction law also considered the effect of the sliding velocities on friction for cases with small sliding velocities [11, 12] in addition to the assumption on the dependence of the kinematic friction on the applied normal force (Coulomb's friction law). It was shown that this creep-rate-dependent friction law is implemented easier into numerical analysis because friction in this law is a continuous function of sliding velocity, unlike the Coulomb's law, where friction has a discontinuity at zero sliding velocity.

Firbank [13] proposed a belt shear theory which considered the mechanics of the belt drives based on both Coulomb friction and shear deformation of the carcass. Shear occurs when the tension-carrying cords rest on a thick belt carcass, which contacts the pulley. Tangential force at the belt/pulley interface and tension in the cords leads to a shear straining of the carcass (Fig. 1-4). Presently, shear theory considers the belt to enter the pulley with zero shear strain, at which point the belt carcass begins to shear as it moves through the adhesion zone until reaching a maximum sustainable shear corresponding to static belt-pulley friction. The belt then enters the slip arc where it experiences sliding

friction. Gerbert [14, 15] extended the theory to include seating/unseating and radial compliance effects. Alciatore and Traver [16] studied the effect of belt bending stiffness and compared shear and creep theories. Kong and Parker [17-21] incorporated belt inertia effects in the belt shear theory, and compared shear and creep theory friction, and normal and belt tension distributions over the pulleys. A major issue with the belt-shear theory [13-16, 19] is that it assumes zero shear strain when the belt first encounters the pulleys, and predicts non-zero shear when the belt leaves the pulley. Thus in a system of at least two pulleys, the theory predicts belt spans with non-zero shear strain at one end and zero shear strain at the other—an apparent paradox recently pointed out by Leamy [22] and investigated preliminarily by Wasfy [23].

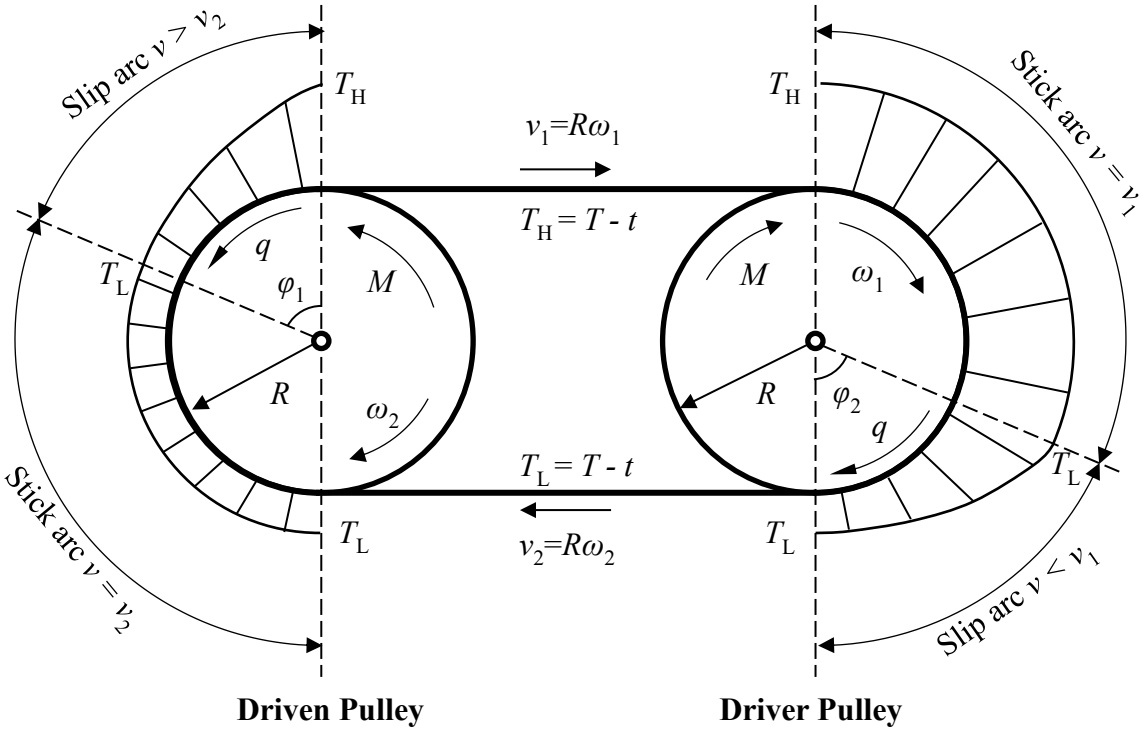

Figure 1-3. Creep of a flexible belt transmitting a torque *M* between pulleys rotating at ω_1 and ω_2.

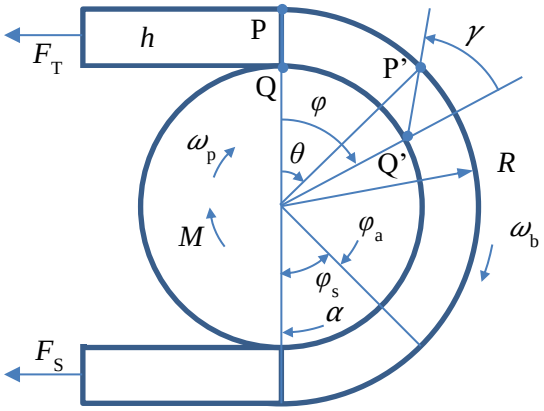

Figure 1-4. Identification of adhesion arc φ_a, slip arc φ_s, and belt shear γ on a rotating driver pulley of radius R. Also identified are the transmitted moment M, the pulley angle from the inlet φ, the pulley and belt angular velocities ω_p, ω_b, and tight and slack side tensions F_T and F_S.

Recently, analytical and numerical models (e.g., based on finite element modeling) have extended analyses to unsteady operation due to harmonic excitation, with some also considering bending stiffness and one-way clutches. Leamy et al. [22, 24-26] attempted to bridge the gap between belt pulley mechanics and system dynamics research by studying simplified dynamic models for small and large rotational speeds. These studies considered individual pulleys only, and did not calculate the global response of the entire belt drive. Furthermore, the case of medium rotational speeds was not addressed. In Leamy and Wasfy [10, 23, 27-30], an explicit time integration finite element code was used to model belt drives. The belt was modeled using a truss element. A penalty formulation was used to model the normal contact constraint between the belt and the pulleys. Friction was modeled using a creep rate dependent friction law, due to its physical relevance [11, 12, 31], its ability to accurately approximate Coulomb friction [10], and its numerical friendliness in the context of explicit time integration. The finite element solution was validated by

comparing it to an exact analytical steady-state solution of a two-pulley belt drive presented in Leamy and Wasfy [10]. This was the first model that bridged the gap between belt mechanics and dynamics. The model could accurately reproduce the steady-state distributions of tangential (friction) force, normal force, belt tension over the rotational motion of the pulleys, belt spans vibrations and tensioner motion [32, 33]. However, in the studies presented in [26, 34, 35], the element types and the discretization sizes chosen were insufficient to accurately capture stick-slip motion and to predict Schallamach waves of detachment.

Most of the investigations of the power losses in belt transmission (mostly for flat and V belts) were initiated by Gerbert [36]. However, the complex time and temperature dependent hysteretic properties [37] of the belt material were not considered. Instead, constant elastomeric properties of the belt rubber (storage and loss moduli) were used. Chen et al. [38] experimentally studied the global energy efficiency of a rubber V-belt continuously variable transmission (CVT) and Greenberg et al. [39] compared the global power loss of belt transmission with various types of belt (flat, V and synchronous belts). Regarding poly-V belts, Manin et al. [40] conducted experiments to study the effects of tensioner and belt properties on the pulley-belt slip in serpentine belt drives. Cepon et al. [41] carried out experiments to identify the friction coefficient between a V-ribbed belt and a pulley. Recently, Balta et al. [42] studied the speed losses in poly-V belt drives with two identical pulleys. Silva et al. [43] focused on predicting the power loss related to the hysteresis dissipation in a belt submitted to dynamic loading, improving the model originally developed by Manin et al. [44]. Silva's model considered the bending, flank and

radial compression, stretching and shear belt-hysteresis phenomenon causing the loss of energy in poly-V belt transmissions [43].

1.3 Elastomer Friction and Schallamach Waves

Friction of elastomers arises from two main mechanisms: deformation and adhesion [45, 46]. The deformational component of friction is connected to the elastomer's viscoelastic properties and results in incomplete recovery of deformation energy during sliding [47]. The adhesive component is pictured as being due to molecular bonding between the elastomer chains and molecules of the interacting counterpart [48], and it is also connected to the bulk viscoelastic properties of the substance [45]. A close correlation between the sliding friction at various speeds and temperatures, and the viscoelastic properties of elastomers, is explained in terms of the manner in which the area of contact and the interfacial shear strength vary with rates of deformation and temperature [49].

Large contact areas formed between deformable elastomers and their interacting counterparts inevitably lead to high adhesive friction [50], which often prevents sliding in the accepted sense. Instead, the displacement of contacting bodies is accommodated by stick-slip [51] or Schallamach waves, which are narrow lines of lost contact that move across the contact area in (or against) the sliding direction (Fig. 1-5). Importantly, no relative movement is discerned between these lines and thus all gross displacement of the elastomer is solely associated with wave motion [2]. Schallamach waves, which form due to the buckling of elastomeric surfaces [52-55], lead to uncontrollable and unstable surface behavior (Fig. 1-6) [54], resulting in vibration, noise, diminished accuracy, energy loss and increased wear that affect the function and shorten the service life of machine components.

Interestingly, in some cases even the lubricant present between the elastomer and its counterpart cannot prevent the appearance of stick-slip instabilities [56, 57].

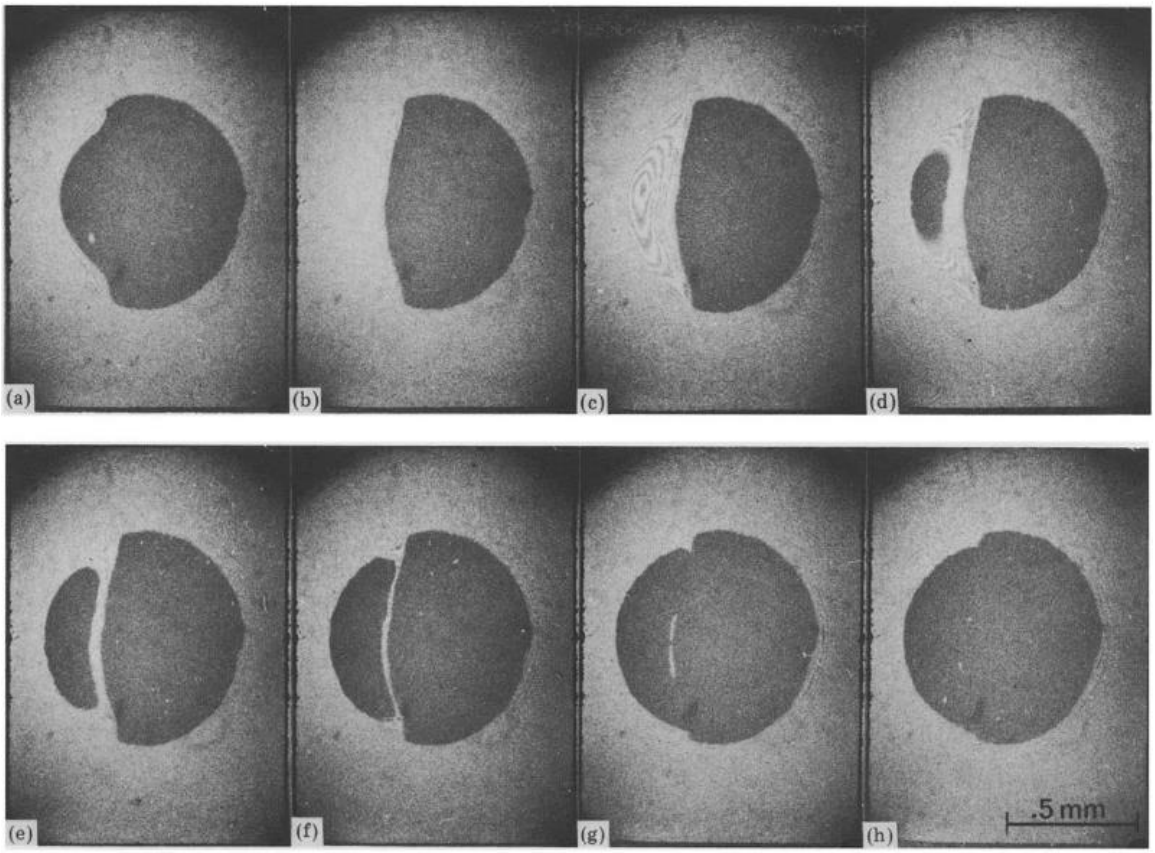

Figure 1-5. Views of the contact area illustrating the successive stages of formation of a re-attachment fold in sliding (curvature radius R = 8 ram; normal load P = 20 mN; sliding speed V = 20 pm s^{-1}): (a), (b) peeling; (c) slip and viscoelastic bulge formation; (d) sticking; (e)-(g) healing; (h) beginning of peeling as in (a).[58]

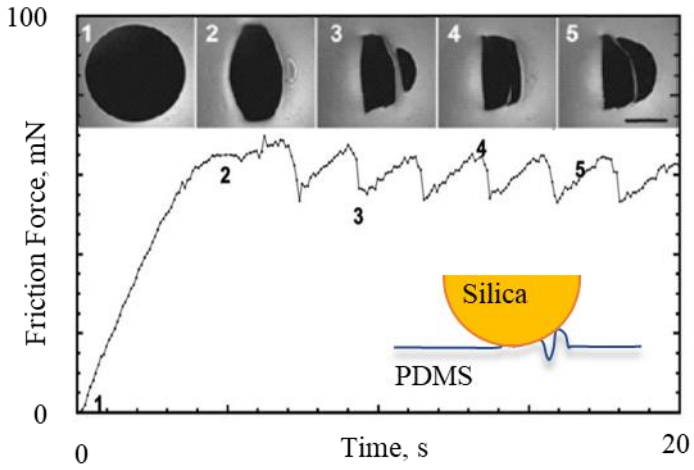

Figure 1-6. Unstable friction force with associated images of contact area. Insert presents a schematic of Schallamach waves.[54]

The present understanding of contact instabilities at the local interface level does not extend to models capable of predicting the onset of surface buckling and the appearance/disappearance of detachment waves in either sliding or rolling. Herein we term this the requisite local model, which will then be subsumed in a larger global, or system-level, model. Similar studies (i.e., those which elucidate the relationship between applied force and relative speed on the generation of detachment waves) are sparse and related only to Schallamach waves of detachment associated with sliding. Barquins [58] characterized Schallamach waves in terms of energy dissipation and found a power law relationship between the propagating speed of the waves and the sliding velocity (Fig. 1-7). Rand [54] proposed a fundamental model addressing the wavelength dependence of Schallamach waves on the sliding velocity and the properties of elastomer, especially its interfacial adhesion and complex modulus. Both Wu-Bavouzet [59] and Viswanathan [60] reported a linear frequency dependence of the occurrence of Schallamach waves with sliding velocity, but not with normal loads. Maegawa [61, 62] observed a more complicated relationship, in the form of a general power law, between the frequency of Schallamach waves and sliding

velocity and normal loads applied, which couples the effects of the sliding velocity and the normal loads.

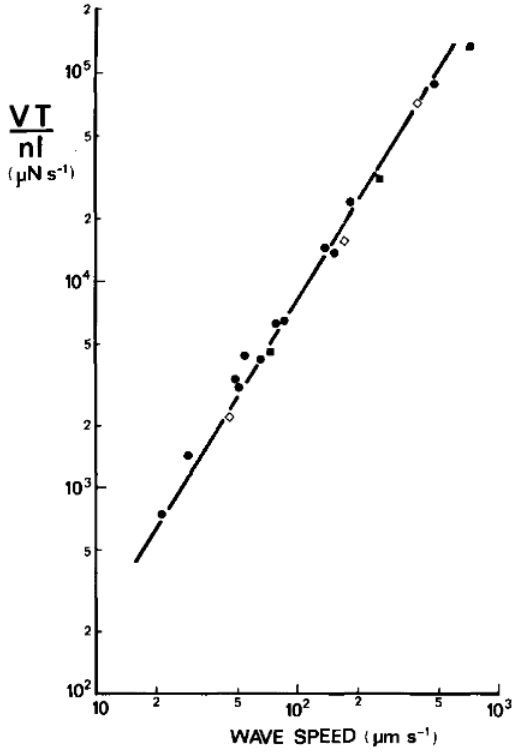

Figure 1-7. Relation between the propagating speed of the waves and the parameter *VT/nl*, where *V*, *T*, *n*, and *l* denote the sliding velocity, tangential forces, number of waves at interface and width of folds, respectively.[58]

It is anticipated that the requisite local model required in the proposed studies (based on perfect stick or Tresca friction) will result in a complex relationship between wave frequency, global motion velocity, normal load, and, in addition, surface stresses. The model recently developed by Yamaguchi et al. [63] offers a good starting point for the necessary local analysis (Fig. 1-8). There, a polyethylene-type adhesive gel-sheet, with a rigid top surface, undergoes gross motion due to a prescribed pull velocity *V*. Unlike the model necessary herein, the system is considered to be inextensible and not carrying a tension force. Instead, only bending and shearing are allowed. However, similar to the

model needed herein, and based on analogs in fracture mechanics, the work required to overcome adhesion (G_0), and thus to form a buckle, is related to the critical release energy (G_c), known from fracture mechanics, via a parameterized relationship with the crack tip velocity (v),

$$G_c(v) = G_0 \left(\frac{v}{v_0}\right)^{\alpha} \tag{1.1}$$

where α and v_0 denote parameters related to the material viscoelasticity. The adhesion work can be equated to the released elastic strain energy, which is ultimately related to the average frictional force exerted on the sample,

$$F_{ave} \approx \frac{\sqrt{6}\mu LW}{2} \left(\frac{G_0}{3\mu H}\right)^{\frac{1}{2(1+\alpha)}} \left(\frac{V}{v_0}\right)^{\frac{1}{2(1+\alpha)}} \tag{1.2}$$

where μ denotes the gel's shear modulus, L the sample length, W its width, and H its height. Thus, the analysis yields the average frictional force F_{ave} as a function of pull velocity V (Eq. 1.2.), as well as the relationship between the separation distance between detachment waves L_c and the pull velocity V (Eq. 1.3.).

$$L_c = \sqrt{6}H \left(\frac{3\mu H}{G_0}\right)^{\frac{1}{2(1+\alpha)}} \left(\frac{V}{v_0}\right)^{-\frac{\alpha}{2(1+\alpha)}} \tag{1.3}$$

Yamaguchi et al. have shown reasonable agreement between their model and experiments.

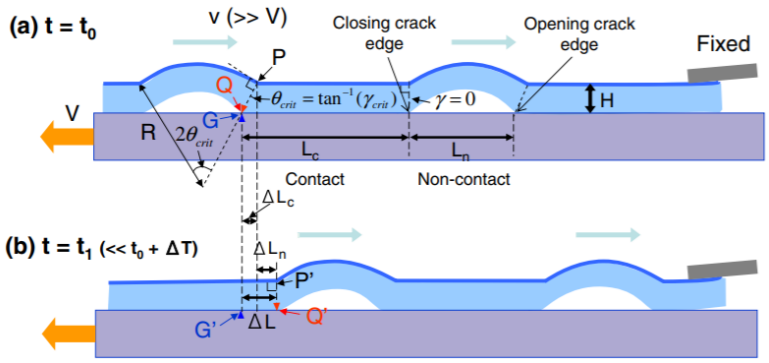

Figure 1-8. Gel (blue) on a rigid substrate (purple).[63]

The appearance of Schallamach waves may be affected by the presence of surface films and surface asperities, which may reduce adhesion forces [64]. To this end, modifying the surface chemistry or topography allows disrupting the formation and propagation of the detachment waves, and thus may stabilize the elastomer friction. There are many types of chemical surface modification. In most cases, different functional groups are introduced at the elastomer surface by treatment with strong acids or chlorinating agents [65]. Atmospheric plasma treatments [66] are also used to introduce adhesion-oriented functional groups [67, 68] on elastomer surfaces as well as to deposit a plasma polymerized coating on top of them [69, 70]. Laser cladding was also recently used to produce polymer-based coating on elastomer substrates [70]. However, these methods are time-consuming and often based on substances that are not environmentally friendly. Moreover, the large elasticity of elastomers makes coating them challenging, as it necessitates a strong adhesion over a wide range of strains. Modification of surface topography, on the other hand, does not produce any of the above mentioned problems and can be achieved by either material removal processes, such as laser surface texturing [71, 72] or simply during the polymer

curing against the template wall. It is clear that the latter method is preferable, as it allows securing the desired surface texture directly without any additional operation.

There is a virtually endless variety of different surface textures that can be tested to find solution to the problem of friction instabilities in elastomers, and it is not a simple task to identify the appropriate one. However, bearing in mind that frictional surfaces evolved in the biological world are known for generating either smooth sliding or complete stop due to stiction (or interlocking), but never intermediate stick-slip motion (except for, maybe, in sick tissues) [73], it is possible to learn from nature's existing solutions [74] to narrow the search. One of the most promising biological surface textures is the hexagonal one found in attachment pads of representatives of tree frogs [75] and bush crickets [76]. The inner construction of these pads is characterized by a dendrite-like structure branching in the proximity of the surface, while the remaining volume is filled up with a liquid [77], which enables these biological composite materials to perform similarly to elastomers [78-80]. It has been previously hypothesized that the hexagonal surface micropattern may function as a friction-oriented feature, preventing hydroplaning and optimizing the thickness of the fluid film in the presence of secretion fluid.

To test this hypothesis experimentally, Varenberg *et al.* [81-83] recently fabricated and examined a cricket-inspired hexagonal elastomeric surface texture (Fig. 1-9). Surprisingly, this surface micropattern not only prevented hydroplaning in wet conditions, but also eliminated stick-slip instabilities in dry conditions and allowed elastomeric friction to be adjusted from as low as approximately 50% to nearly 100% of that for the unmodified surface. This renders this texture as potentially attractive for many tribological applications based on rubber-like material [84-86].

The disappearance of stick-slip instabilities has also been observed with other more sophisticated biomimetic textured elastomer surfaces [87, 88], which suggests that this phenomenon may be intrinsic to the frictional response of textured elastomer [89], such as wrinkle-patterned surfaces for example [90]. However, only very limited experimental and theoretical work has been performed so far to uncover the mechanism responsible for this intriguing frictional performance of textured elastomer surfaces. Moreover, there is another class of relative motion, namely, rolling, which is widely used in various elastomer-based driving devices, and is likely to be affected by surface texturing, as it inevitably involves elements of sliding [64]. Rolling of regularly textured elastomers remains, however, essentially unexplored. Though there is evidence that random micro-texture may improve the tribological performance of belt drives [91], which utilize rolling for power transmissions, the mechanics of how friction or wear in rolling are (if at all) affected by surface texturing is unknown.

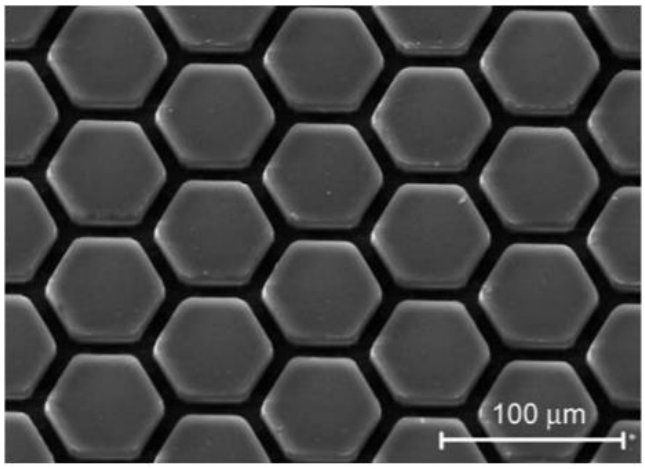

Figure 1-9. Biomimetic hexagonal surface texture.[81]

1.4 Research Goals

Although investigation of belt drive systems is extensive, contact instabilities associated with Schallamach waves remain unaddressed. As stated in Section 1.3, the inability to accommodate relative displacement by sliding should also affect rolling of elastomeric surfaces, which has long been known to involve slip over part of the contact area, for instance, in the so-called 'slip' arc in a belt drive system. Consequently, the current belt drive models employing traditional sliding-based friction law can be intrinsically inaccurate. Further, the local frictional instabilities at the contact region may affect the dynamic response of the global system, which in turn may also influence the generation of the contact instabilities. These events can be harmful to the belt drive system, increasing noise and vibration, reducing the energy efficiency, and shortening the service life. However, the interrelation between the local instabilities and global oscillations in belt drives remains unexplored, which may also hinder further progress in designing green machinery.

In light of the above, it is proposed to investigate, through experiment and modeling, the Schallamach waves of detachment and friction-induced self-oscillations in belt drive systems. The Schallamach waves will be discerned on a custom-built tribometer, and the effects of the loading conditions and the system's properties will be explored. Friction mechanisms, contact mechanics and system dynamics for belt drives will be studied. Of particular interest is the investigation of the coupling between local contact instabilities (including but not limited to Schallamach waves) and the global system's dynamic response. Models capturing contact instabilities coupling to the dynamic response of the belt drive system as well as the system's dynamics coupling to the generation of

Schallamach waves will be developed. Then, biomimetic patterning will be adopted on the belt surface in order to explore the possibility to disrupt the occurrence of detachment-based contact instabilities. Lastly, belts incorporating tension cords, which are comparable to industrial belts, will be investigated to answer the question of whether the detachment events are universal in belt drive systems.

CHAPTER 2. DETACHMENT WAVES

In this chapter, we present an experimental study of the rolling contact mechanics in a simple flat belt drive. Given that the elastomeric belt surface is unable to slide, we explore the mechanism of relative displacement and friction generated at the belt/pulley interface in both driver and driven cases. Then, we continue studying the formation of detachment waves as functions of the applied torque, the operating speed (all speeds are limited to slow operation), and the system moment of inertia. In so doing, we uncover contact instabilities in the form of periodic detachment waves leading to pulley oscillations, which grow in time.

2.1 Method and Means

2.1.1 Apparatus

The experimental apparatus is built on the basis of a one-pass-slide tribometer [92, 93] able to measure forces in the direction of the stage motion. Fig. 2-1 represents a schematic and a 3D CAD model of the test rig incorporating the driving, loading and measuring systems. The driving system consists of a linear translation stage drawn by a dead weight and an electric motor releasing the stage at a constant controlled speed. The loading system consists of another linear translation stage moving in the same direction and a stationary pulley with a replaceable flywheel used to change the inertia of the system. Loading is realized using two adjustable dead weights: one to apply tension to the belt, and another to apply torque to the pulley, while reversing the direction of the torque allows the user to switch between the driver (as shown in Fig. 2-1a) and driven cases. The measuring system consists of an S-beam load cell LRM200 (FUTEK, Irvine, CA) and a linear encoder

LM10IC (Renishaw, West Dundee, IL) mounted on the driven stage, a bending beam load cell LBB200 (FUTEK, Irvine, CA) and another LM10IC encoder mounted on the driving stage, a rotary encoder RE36IC (Renishaw, West Dundee, IL) mounted on the pulley, and a monochrome digital camera DMK 23UP1300 (Imaging Source, Charlotte, NC) with an optical lens Zoom 12X (Navitar, Rochester, NY) mounted in front of the trailing (slip) side of the belt/pulley contact zone.

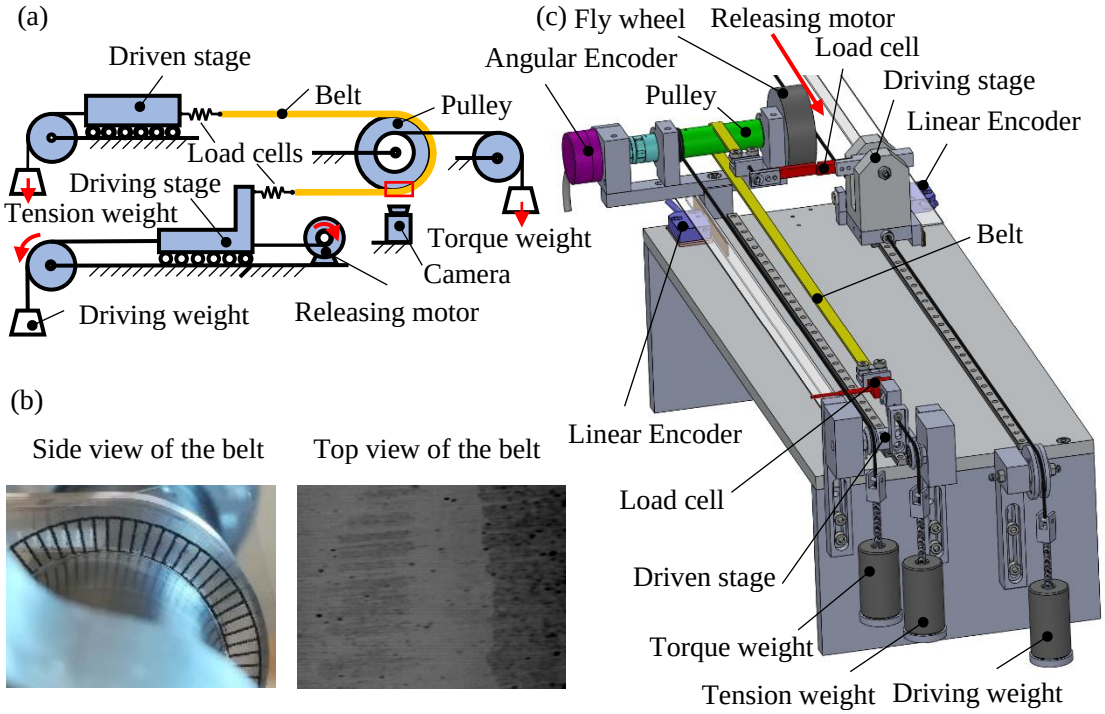

Figure 2-1. Experimental apparatus in (a) schematic representation and (b) 3D CAD model, and (c) side and top view of the belt.

The belt specimen is wrapped over the pulley and clamped to the stages through the load cells, such that when the driving stage is set in motion, the belt rotates the pulley and forces the driven stage. The forces acting on the belt ends, as well as the linear and

rotary displacements of the stages and the pulley, are sampled with a multifunctional data acquisition board PCIe-6351 (National Instruments Co., Austin, Texas). The data are processed with a custom application written using a LabVIEW software package (National Instruments Co., Austin, Texas). Visualization of the shear strain is based on the comparison of the tick marks created on the belt sidewall and on the transparent reference, which rotates with the pulley. The real contact area is seen as a darker region due to optical interference at the belt/pulley interface (Fig. 2-1c).

2.1.2 Belt Specimen Preparation

The belt specimens were produced by molding polydimethylsiloxane (PDMS, Sylgard 184, Dow Corning, Midland, MI), which is a transparent elastomer. A 10:1 mixture of Sylgard 184 pre-polymer and its cross-linker was cured for 14 h at 65 ^{o}C in a flat smooth template. To drive out the air bubbles trapped inside by mixing the polymer, the curing took place in light vacuum. To trace the shear strain distribution alongside the belt while in operation, evenly distributed tick marks with 1 mm interval were created on the belt sidewall during molding by using a standard ruler as one of the template sidewalls. Finally, a belt specimen of 400 mm in length, 8 mm in width and 3 mm in thickness was cut from the mold. Limited by the strength of PDMS, we chose to work with a maximum allowable belt tension of 6 N. Hence, the torque and tension weights were adjusted so that the belt tension ranged from 2 N to 6 N.

2.1.3 Operating Conditions

Previous investigations on Schallamach waves in sliding find that the frequency and the amplitude of the detachment waves depend on sliding velocity and loading

conditions [52, 53, 55, 58, 94]. To study the same quantities in our belt drive system, we varied the stage driving velocity from 3 mm s^{-1} to 11 mm s^{-1} using incremental changes of 2 mm s^{-1}.

Note that there is a distinction between the dead weight used to apply torque and the "net torque weight" effectively acting on the pulley. This difference arises due to the parasitic resistance from friction in the bearings and the rotary encoder. As a result, the cases of driver and driven pulley need different dead weights to achieve the same net torque applied to the pulley. Bearing this in mind, we adjusted the loading such that the net torque weight applied to the pulley ranged from 3.5 N to 5.5 N with an increment of 0.5 N for both driver and driven cases.

For all tests performed, the high tension (on the entering side for the driver case and on the exiting side for the driven case) remained at 6 N, the maximum tension that our belt specimen can bear without failure. The travel distance of the driving stage was 200 mm (~3.3 revolutions of the pulley). Tables 2-1 and 2-2 list detailed operating conditions for variation of driving speed and load, respectively. Each test was repeated at least 5 times. All statistical tests were performed using one-way ANOVA; all pairwise multiple comparison procedures (Holm-Sidak method), with overall significance level 0.05, were performed using the SigmaPlot software package (Systat Software Inc., San Jose, CA). The temperature and relative humidity in the laboratory during the tests were 23°C and 35%, respectively.

Table 2-1. Experimental conditions for variation of driving speed.

Speed	3 mm s^{-1}	5 mm s^{-1}	7 mm s^{-1}	9 mm s^{-1}	11 mm s^{-1}
Net torque weight			4 N		
Flywheel			None		

Table 2-2. Experimental conditions for variation of load.

Speed			3 mm s^{-1}		
Net torque weight	3.5 N	4 N	4.5 N	5 N	5.5 N
Flywheel			None		

2.2 Detachment Wave-Induced Instabilities

Figure 2-2 documents the forces measured during the operation of the system and the characteristic sequences of images representing the contact area evolution in both the driver (Fig. 2-2a) and the driven (Fig. 2-2b) cases. Regardless of the drive type, the entering side of the belt experiences more or less constant tension, which results from the "load control" boundary conditions. The exiting side of the belt operates under the "speed control" boundary conditions, which leads to fluctuations in tension that are defined by the changes in the contact stresses generated at the belt/pulley interface. The fluctuations become larger after the initial transient period is over and the steady state rolling conditions are established. It is also worth noting that because the rolling contact mechanics appears

to be different in the driver and the driven cases, we had to adjust both the direction and the magnitude of the pulley torque in order to have comparable force measurements.

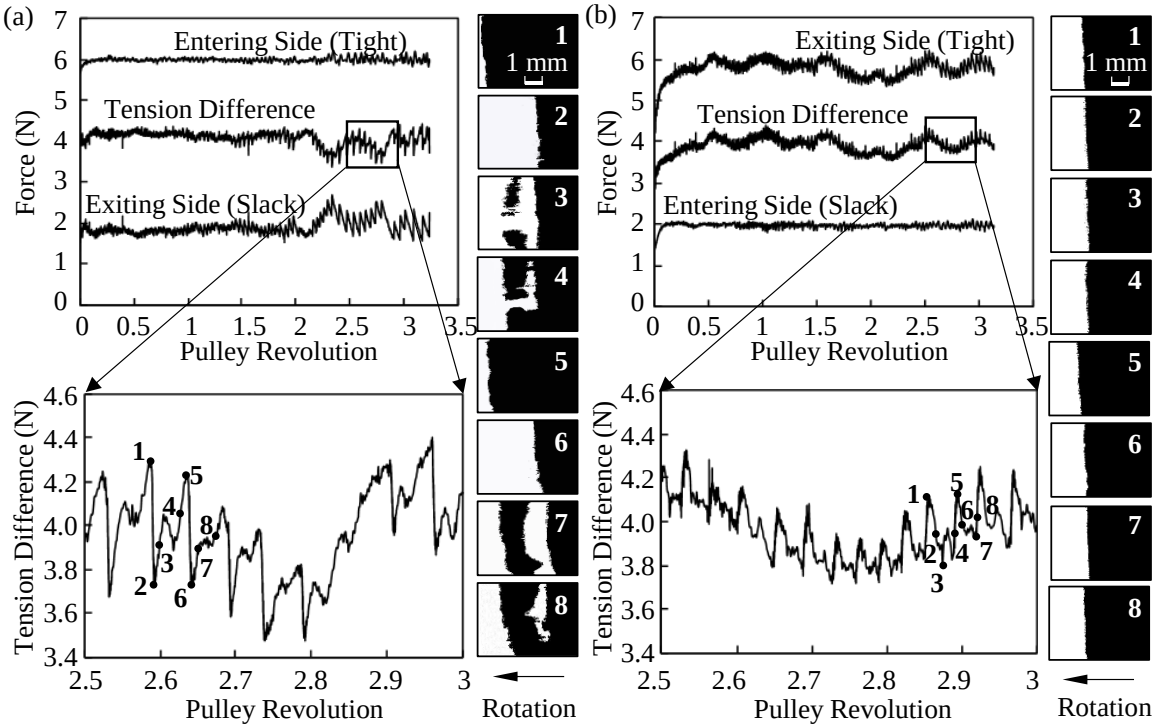

Figure 2-2. Forces measured during the operation and characteristic sequences of images representing evolution of the contact area (shown in black) in the driver (a) and driven (b) cases.

2.2.1 Contact Instabilities

The difference between the tight and the slack side tensions integrates the stresses developing along the contact arc and allows us to capture the global large-scale instabilities associated with the stick-slip motion. Interestingly, because the low-inertia pulley operates under "load control" conditions in our experiments, the stick-slip events disturb rotational motion in the pulley. Once the pulley's angular velocity starts oscillating, it effectively stores a belt tension pattern in the entry zone, which serves as an additional excitation

source when this pattern is released on the exit side of the belt. This demonstrates once again that stick-slip events, though being local, are able to affect the global dynamics of the system.

The tension difference curves obtained for the driver and the driven cases demonstrate clear differences in both the amplitude and the frequency of the stick-slip events, which appear to be more pronounced in the driver case. A close-up of the tension difference signal is presented to enable correlation with the characteristic images of the contact area, which are shown in a black-and-white mode to differentiate clearly between the contact (black) and non-contact (white) zones. It should be noted here that before processing the images, we closely studied the contact area evolution and, as expected, we did not find any evidence of sliding in either the driver or the driven case. Instead, the relative displacement between the belt and the pulley was achieved by means of cyclic detachment.

In the driver case (Fig. 2-2a), the process of detachment/re-attachment appears to be asymmetric in both time and space. The sequence of the real contact area images starts at point 1, where both the tension difference and the contact area reach their maxima. Then, a large fraction of the contact area detaches nearly at once by fast motion of the peeling front running backwards (with respect to the rotation direction), which results in a steep drop of the tension difference at point 2. Next, a much slower process of re-attachment starts. A newborn contact forms approximately in the center of the detached zone and grows in both forward and backward directions, which is accompanied by an increase in the tension difference from point 2 to point 5. The loading phase is occasionally interrupted by the precursor relaxation/detachment events that run through this secondary newborn

contact and lead to local drops of the tension difference. After the contact area is rebuilt completely at point 5, the process repeats. Thus, it becomes evident that waves of detachment take place in the belt drive, though their appearance differs from that described previously [2].

In the driven case (Fig. 2-2b), the fluctuations in both the tension difference and the contact area size appear to be more symmetric and have smaller amplitudes. The most important difference, however, manifests in that detached regions never come in contact again, and the contact area growth happens on account of the pulley rotation, which pulls the adhesive zone forward until it peels backwards again when a critical load is achieved. Thus, no waves of detachment are seen and the observed fluctuations in tension difference and contact area can be associated with the effect of adhesive hysteresis [95].

To visualize shear deformation along the contact arc, we have plotted shear strain (a tangent of the angle between tick marks on the belt sidewall and on the transparency reference) as a function of angular position measured from the belt entry point to the belt exit point (Fig. 2-3). One can see clearly that the shear-affected zone is much larger in the driver case, which fits well the observations of the real contact area presented in Fig. 2-2. Comparison of the slip arc angles obtained by different methods (Table 2-3) should also be instructive, as follows.

The experimental boundary between the stick and the slip zones was defined based on: (a) the position of the maximum shear strain (relative displacement is a relaxation mechanism, so stresses should fall when a relative motion is enabled), (b) the largest size of the detachment zone (white region in the images shown in Fig. 2-2), and (c) optical

observation of the belt sidewall appearance. The average values calculated for both the driver and the driven cases are presented in Fig. 2-3 as a grey/white border.

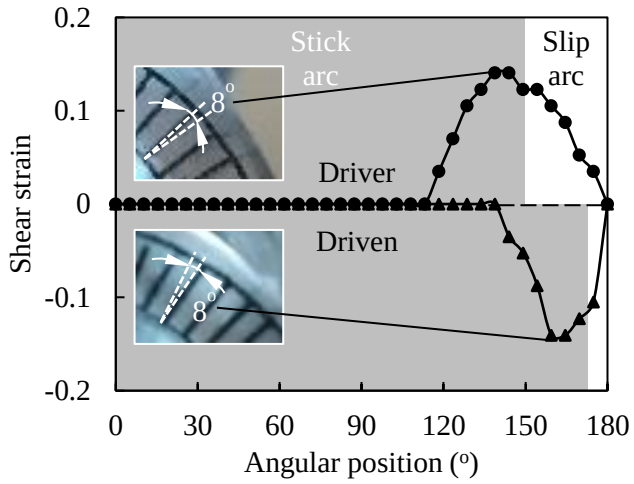

Figure 2-3. Shear strain as a function of angular position in the driver and driven cases.

The theoretical boundary between the stick and the slip zones, which is identical for the driver and the driven cases, was computed based on the capstan formula $e^{\mu\varphi} = T_H/T_L$, where T_H and T_L are the high and low tensions on the tight and slack sides, respectively, μ is the friction coefficient and φ is the slip arc angle [3]. Though the Amontons' laws of friction are not applicable to elastomers, and the idea of friction coefficient is of little value when elastomers are discussed [96], this simple approach is widely used for analysis of rolling contact mechanics. Given that the coefficient of friction of PDMS can range between 1.3 and 2.3 [81], it is evident that the theoretical slip arc angle does not agree well the experimental observations, which calls into question the validity of this approach in the case of elastomeric contact.

Table 2-3. Slip arc angles obtained by different methods.

Method	Slip arc angle (°)	
	Driver	Driven
Max. shear strain position	36.0	15.4
Contact area observation	25.7	2.6
Sidewall observation	28.3	3.0
Average	30	7
Theoretical, $\mu = 1.3 - 2.3$	48 – 27	48 – 27

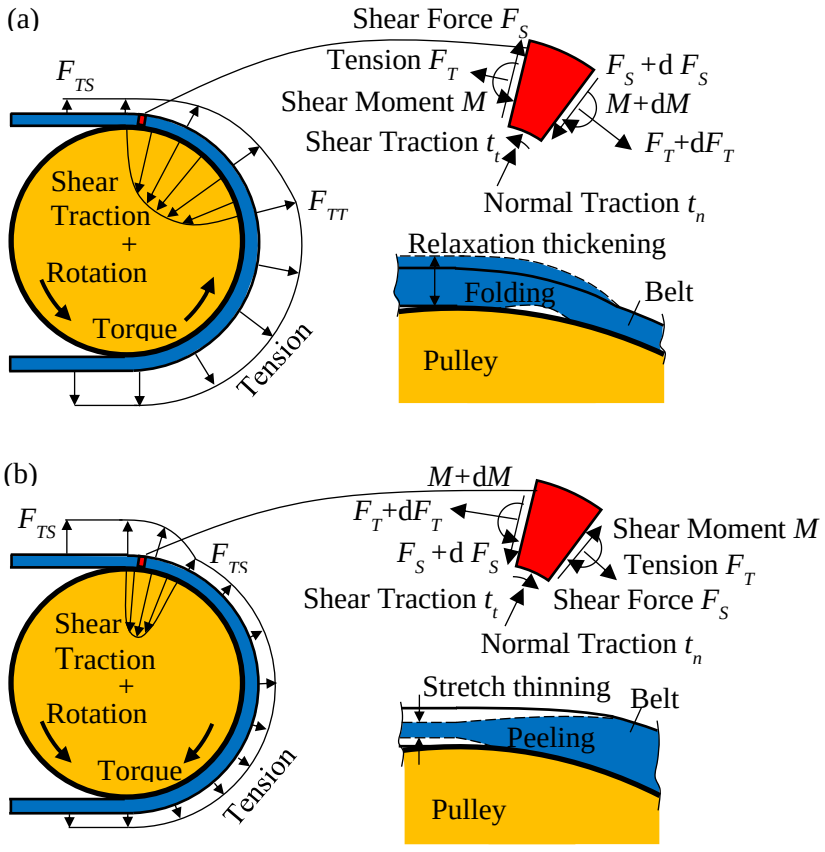

Figure 2-4. Schematic of the contact behavior in the driver (a) and driven (b) cases.

Following the above measurements and observations, Fig. 2-4 presents a schematic of the contact behavior; it is based on a free body diagram of the belt segment taken from the region subjected to shear traction. In both the driver and the driven cases, the forces acting on the belt segment in the circumferential and radial directions are in equilibrium. However, because the difference in tension, which is acting at the neutral axis of the belt, is balanced by the shear traction, which is acting at the belt/pulley interface, there is a moment acting on the belt.

In the driver case, this traction-initiated moment tends to lift the belt from the pulley. When the belt detaches, the shear traction disappears and the traction moment relaxes, which brings the belt back in contact due to the restoring action of the tension forces' radial components. This sequence leads to the generation of a surface fold that can travel along the interface in the backward direction until it closes because of increasing normal load at smaller angles. The question is whether this surface fold can be associated with the classic buckling-based surface instabilities [2, 52-55]. Interestingly, the inner belt surface can experience some compression due to bending when the belt detaches from the pulley and the shear traction disappears, which could lead to buckling. However, the fact that the width of this surface fold can change (Fig. 2-2a), while the classic buckling-based wrinkles maintain a constant and much smaller width during their lifetime [2, 52-55], makes it highly improbable that buckling is involved in the formation of the folds observed in this work. It should be stated though that this question calls for further in-depth investigation.

In the driven case, the traction-initiated moment acts in the opposite direction, which results in the belt being pressed further against the pulley. However, the belt tends

to become thinner because of the increasing tension. This thinning may pull the belt out of the contact, leading to local detachment at the contact area edge. This effect is not expected to be large, though, and the relatively small amplitude of fluctuations in the contact area size (Fig. 2-2b) supports this assumption. Once detached from the pulley, the belt does not attach again, and the contact area simply moves forward together with the pulley until the belt peels off again. Thus, in a process similar to ball-on-flat rolling [97], the contact mechanics of the driving and the braking pulleys differs significantly, which may explain the different vibrational characteristics of the two belt drive cases.

2.2.2 Oscillations in Belt Tension

Contact instabilities formed in both driver and driven cases lead to oscillations in belt tension and in pulley rotation. Figure 2-5 documents the tension difference and angular velocity, as a function of pulley revolution, obtained experimentally at a driving speed of 3 mm s^{-1} using a net torque weight of 4 N in both the driven (Figure 2-5a) and the driver (Figure 2-5b) cases. The difference between the tight and slack side tensions measured by the force transducers with a resolution of 0.04 N. The angular velocity is computed via a central difference scheme from the angular displacement registered by the rotary encoder with a resolution of 8192 counts per revolution.

The subfigures in the top row clearly document growing oscillations, with similar frequency content, in both measured quantities. A zoomed-in plot (middle row) shows the correlation between the tension difference and angular velocity such that the period of the tension difference oscillations coincides with that of the pulley oscillations (each period denoted by two adjacent dashed-dot lines). It is also evident that the tension difference

signal exhibits additional, higher frequency content associated with belt detachment at the exit of the pulley. This is borne out by comparisons of the tension difference signal with the contact area in the exiting region of the belt-pulley interface (see numbered points on the tension difference, middle subfigure, and corresponding numbers on the contact area snapshots), where black areas denote contact, and white areas denote loss of contact between the belt and the pulley. Similar to the results in Section 2.2.1, waves of detachment (see isolated detached pocket on third contact snapshot in the driver case) are detected only in the driver case.

The tension difference fluctuations were analyzed further via wavelet transform routines available in Matlab and were decomposed into two primary components: 1) a high-frequency component (dashed line) associated with the detachment events at the belt-pulley interface (T_{de}); and 2) a low-frequency component (solid line) associated with the pulley oscillation (T_{po}). Interestingly, the T_{po} signals in the driver and driven cases exhibit distinct reverse saw-tooth shapes, and this becomes more evident as the system inertia increases (see Section 2.3.3). This result can be explained in the following way. Comparing the T_{po} signal to the angular velocity oscillations (left-bottom sub-figure in Figure 2-5), we can see that the minute halts in the pulley rotation are associated with the tension difference drop in the driver case and with the tension difference rise in the driven case. In the driver case, when the pulley drives the belt, the pulley motion cessation leads to decrease of the difference between the tight and slack side tensions (the belt is relaxed). On the other hand, in the driven case, when the belt drives the pulley, the pulley motion cessation leads to increase of the difference between the tight and slack side tensions (the belt is loaded).

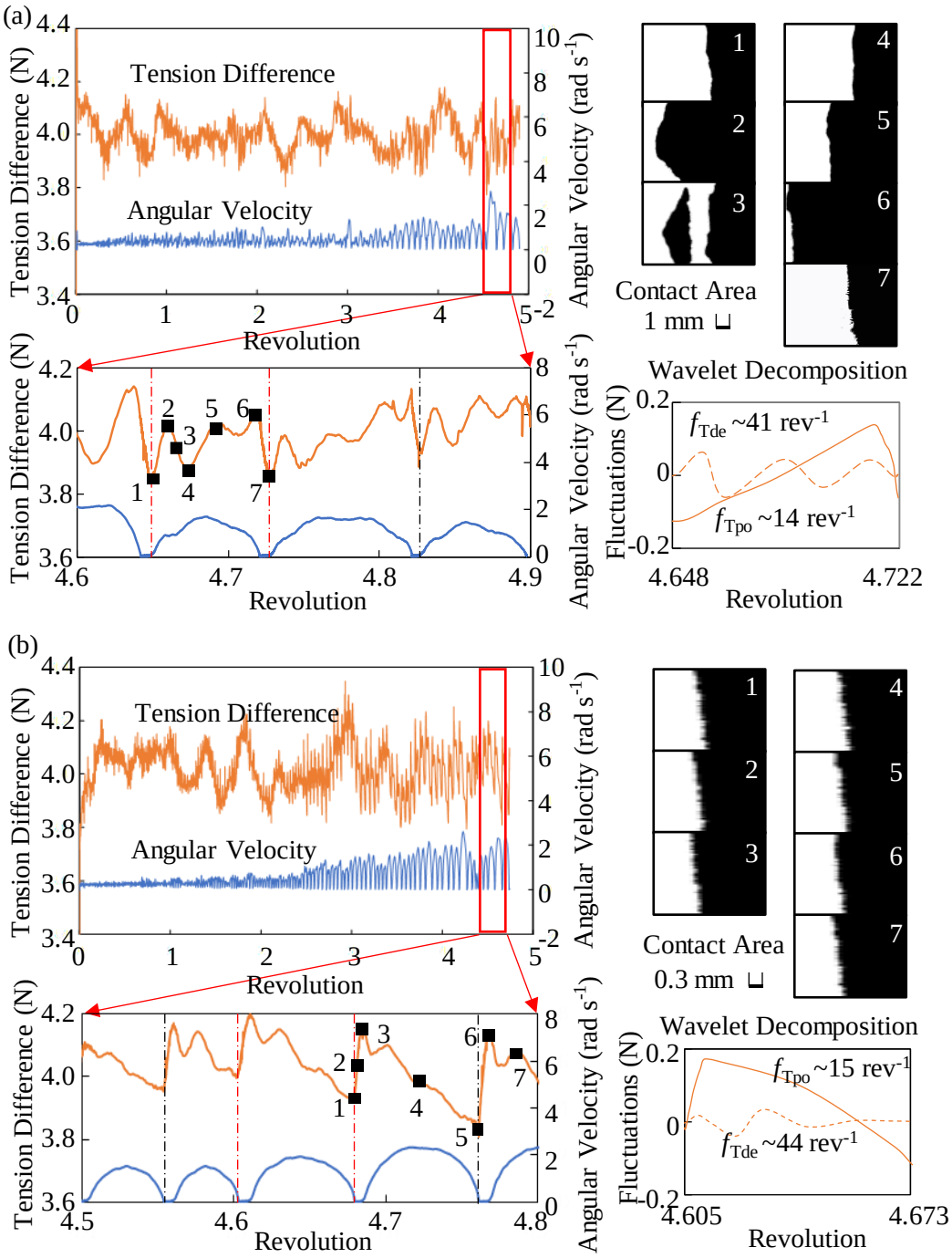

Figure 2-5. Tension difference, angular velocity and characteristic images representing evolution of the contact area (shown in black) in (a) the driver and (b) the driven cases. A wavelet decomposition exhibits the two primary components of the tension difference signal: fluctuations associated with detachment events (T_{de}) and fluctuations associated with pulley oscillations (T_{po}).

2.2.3 Oscillations in Pulley Angular Velocity

We believe the oscillation growth observed in both the tension difference and the angular velocity is due to a positive feedback mechanism as follows: contact instabilities in the belt exit zone excite rotational oscillations in the pulley, which in turn store a periodic belt tension pattern in the belt entry zone. This tension pattern then serves as an additional excitation source when released at the exiting side of the belt, further destabilizing the pulley angular velocity. Thus, local contact instabilities induce large changes in the system's global dynamics. Given that the dynamic response evolves in time, in the parametric studies to follow we chose to focus on the final pulley revolution where the self-excited oscillations are most evident.

2.3 System Behavior under Different Loading

2.3.1 Effects of Tension and Torque

The fluctuations in both the tension difference and the angular velocity were decomposed into two components related to detachment events and pulley oscillations. Their corresponding frequencies and amplitudes are shown in Fig. 2-6. The fluctuations in angular velocity resemble those in tension difference (especially in terms of frequency), which verifies the correlation between these two signals. The information on the fluctuations in the angular velocity associated with detachment events is missing for the driven case because of a low signal-to-noise ratio resulting in an inability to get reliable data.

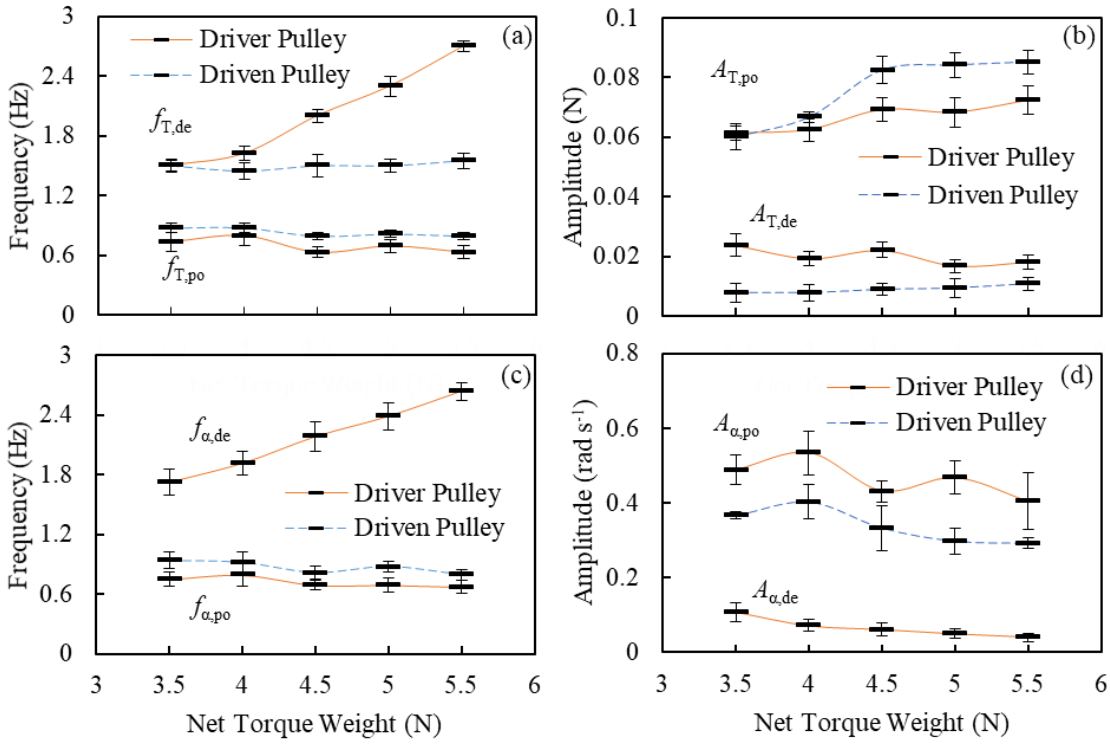

Figure 2-6. The frequency (*f*) and amplitude (*A*) of the fluctuations in the tension difference (T), (a) and (b), respectively, and in the angular pulley velocity (α), (c) and (d), respectively, associated with detachment events (de) and pulley oscillations (po), and presented as a function of loading conditions in both the driver and driven cases. The error bars show standard deviation.

The fluctuations in the tension difference associated with detachment events exhibit higher frequency and lower amplitude than those associated with pulley oscillations in both the driver and driven cases (Fig. 2-6a, and 2-6b). As the net torque weight increases in the driver case, the amplitude $A_{T,de}$ is barely affected (a statistically significant difference is observed only between torque weights 3.5 and 5.5 N, and between 3.5 and 5 N), whereas its frequency $f_{T,de}$ increases. This increase is consistent with the hypothesis that a traction-induced moment tends to lift the belt from the pulley, while the belt remains attached until the traction moment reaches a certain threshold. Increasing the net torque weight raises the traction applied to the belt and reduces the gap between the acting moment and the

threshold value. This leads to less time needed to reach the threshold value for detachment, resulting in increase of the fluctuation frequency. In the driven case, however, the frequency $f_{T,de}$ and the amplitude $A_{T,de}$ do not depend on the net torque weight (no statistically significant effect is observed). In this case, the traction-induced moment acts in the opposite direction, pressing the belt against the pulley. The detachment at the contact edge happens as a result of the thinning and peeling of the belt, and these mechanisms are not directly affected by the shear traction. The amplitude $A_{T,de}$ in the driver case is larger than that in the driven case because the scale of contact instabilities is much larger in the former case (Fig. 2-5).

The frequency of the tension difference fluctuations associated with the pulley oscillations ($f_{T,po}$) does not depend on the net torque weight (no statistically significant effect is observed). The torque weight adds inertia to the system, so, in principle, the frequency $f_{T,po}$ should decrease with increasing torque. The reason for not observing this effect can be an insufficient range of the torque change. A small difference between the frequencies $f_{T,po}$ in the driver and driven cases may result from a larger torque weight used in the driver case to attain the same net torque weight as in the driven case, which results in a larger system inertia. The amplitude of the tension difference fluctuations associated with the pulley oscillations ($A_{T,po}$) shows an inconsistent step-like increase with increase in the net torque weight from 4 to 4.5 N, while maintaining statistically indistinguishable values otherwise. This can be related to some issue that went unnoticed during the tests and is worth verifying based on the analysis of the angular velocity oscillations below.

The frequencies of the angular velocity fluctuation $f_{\alpha,de}$ and $f_{\alpha,po}$ (Fig. 2-6c) are almost identical to those of the tension difference fluctuations (Fig. 2-6a) because they

characterize the same response. Similar to $A_{T,de}$ in the driver case (Fig. 2-6b), the amplitude of the angular velocity fluctuation $A_{\alpha,de}$ (Fig. 2-6d) is nearly not affected by the torque increase (no statistically significant difference is observed between the torque weights 4, 4.5, 5 and 5.5 N). Analyzing the amplitude $A_{\alpha,po}$, we also see almost no effect of the torque weight (statistically significant difference is observed only between the torque weights 4 and 5.5 N in the driver case, as well as between the torque weights 4 and 5.5 N, 4 and 5 N, and 3.5 and 5 N in the driven case), which resembles the results obtained for $A_{T,po}$. Thus, based on a comparative analysis of the effect of torque, we can conclude that, to a first approximation, the only affected parameter is the frequency of waves of detachment in the driver case.

2.3.2 Effect of Driving Speed

In both the driver and driven cases, increasing driving speed accelerates the occurrence of contact instabilities (detachment events) and pulley oscillations regardless of the analyzed signal source, be it either tension difference or angular pulley velocity (Fig. 2-7a and 2-7c, respectively). Given that the formation of the stress pattern along the contact arc relies on the rotation of the pulley, the stress relaxation associated with detachment events at the belt-pulley interface takes less time as the pulley rotates faster. The pulley oscillations are mainly caused by contact instabilities, so when the latter occur more often, the former follow suit. Hence, all frequencies increase with increase in driving speed. It is also evident that the pulley oscillations in the driven case appear to be more sensitive to the driving speed, so the frequency $f_{T,po}$ increases more rapidly than that in the driver case. This can result from a larger system inertia in the driver case due to a larger torque weight used to obtain the same net torque as in the driven case.

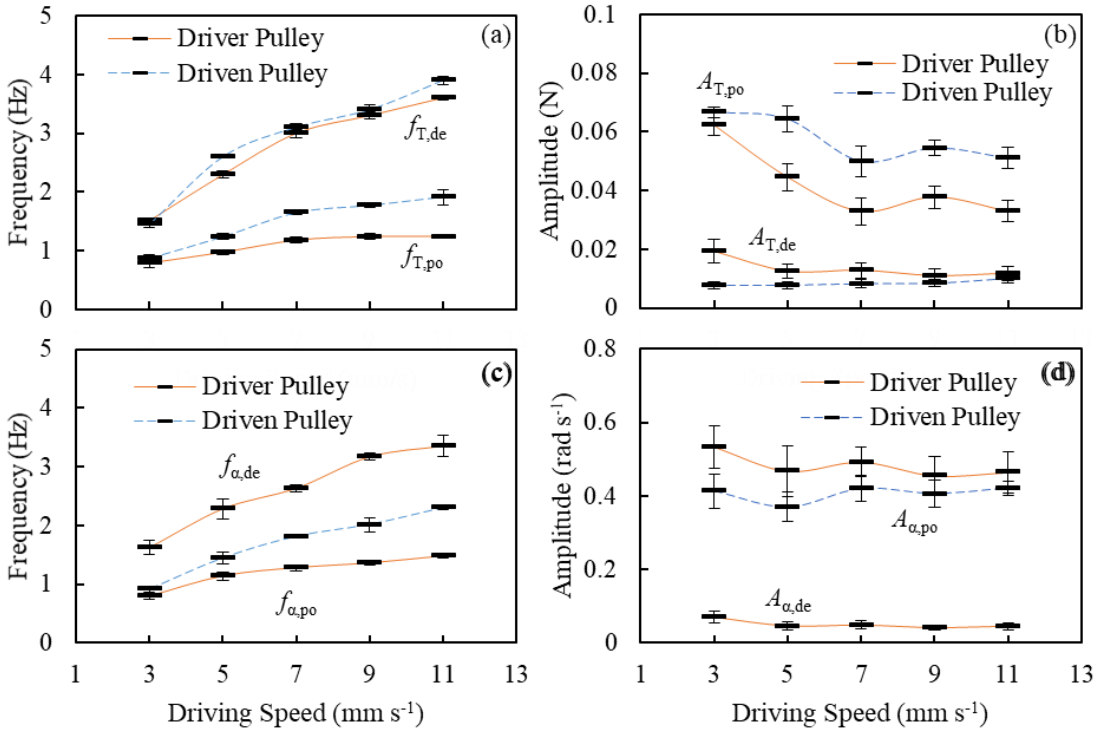

Figure 2-7. The frequency (*f*) and amplitude (*A*) of the fluctuations in the tension difference (T), (a) and (b), respectively, and in the angular pulley velocity (α), (c) and (d), respectively, associated with detachment events (de) and pulley oscillations (po), and presented as a function of driving speed in both the driver and driven cases. The error bars show standard deviation.

The amplitude of the tension difference fluctuations associated with the pulley oscillations ($A_{T,po}$, Fig. 2-7b) exhibits an inconsistent step-like decrease with increase in driving speed from 5 to 7 mm s^{-1}, while maintaining otherwise statistically indistinguishable values in the driven case. In the driver case, the effect of the driving speed on the amplitude $A_{T,po}$ is also not statistically reliable (no statistically significant difference is observed between the speeds 5 and 9 mm s^{-1}, 7 and 9 mm s^{-1}, 7 and 11 mm s^{-1}, 9 and 11 mm s^{-1}). The amplitude of the tension difference fluctuations associated with the detachment events ($A_{T,de}$, Fig. 2-7b) also does not demonstrate any clear effect of the driving speed. In the driven case, no statistically significant difference between different

amplitudes is observed at all, while in the driver case, only the amplitude obtained at the speed 3 mm s^{-1} differs from all other measurements.

The amplitude of the angular velocity fluctuations associated with the pulley oscillations ($A_{\alpha,po}$, Fig. 2-7d) has shown no statistically significant effect of driving speed in either the driver or driven cases. The effect of the driving speed on the amplitude of the angular velocity fluctuations associated with the detachment events ($A_{\alpha,de}$, Fig. 2-7d) is also negligible, with only the amplitude obtained at the speed 3 mm s^{-1} being different from all other measurements. Thus, based on a comparative analysis of the effect of driving speed, we can conclude that, to a first approximation, while the amplitudes of either the contact instabilities or the pulley oscillations are not affected, their frequencies grow with increase in driving speed. Note that the frequency versus speed relationship in our findings compares well with that found in sliding cases where an increasing speed also leads to an increased Schallamach wave frequency [55].

2.3.3 Effect of System's Inertia

As reported above, contact instabilities excite pulley oscillations, complicating the study of the contact mechanics. In an attempt to limit these oscillations, we increased the moment of inertia of the pulley by using two removable flywheels, whose moments of inertia are 9 and 99 times that of the pulley. These are referred to as Small and Large flywheels. Table 2-4 lists the conditions employed in assessing the effect of inertia.

An illustration of the effect of the pulley's moment of inertia on the tension difference and angular velocity is presented in Fig. 2-8. Looking at the tension difference curves, we conclude that the effect of the pulley's moment of inertia is identified clearly in

the fluctuations associated with the pulley oscillations (see the wavelet decomposition subfigure in Fig. 2-5 for comparison), while the fluctuations associated with the contact instabilities seem to be less sensitive to this parameter. Interestingly, increasing the pulley's moment of inertia results in much more violent oscillations in the tension difference, while the pulley oscillations become more restrained. This is explained by noting that larger difference between the tight and slack side tensions is needed to move a heavier pulley, which has larger moment of inertia and hence rotates more steadily.

Table 2-4. Experimental conditions for variation of the moment of inertia of the pulley.

Speed		3 mm s^{-1}	
Net torque weight		4 N	
Flywheel	None	Small	Large

Analyzing the frequencies and amplitudes of the fluctuations in the tension difference and the pulley's angular velocity (Fig. 2-9), we can draw similar conclusions. The frequencies of the fluctuations in both the tension difference and the angular velocity associated with the pulley oscillation ($f_{T,po}$ and $f_{\alpha,po}$, respectively) decrease with increases in the pulley's moment of inertia in both the driver and driven cases, which is the expected result. Notably, the discrepancy between the scale of the decrease in frequency and the scale of the increase in pulley's moment of inertia is due to that the total moment of inertia of rotary parts includes the contribution from the torque weight as well (as shown in Eq. 2.3). The amplitude of the tension difference fluctuations associated with the pulley oscillations ($A_{T,po}$) grows with increase in the pulley's moment of inertia in both the driver and driven cases, which results from higher belt tension being required to move (or

interfere with) the heavier pulley. The amplitude of the angular velocity fluctuations associated with the pulley oscillations ($A_{\alpha,po}$) decreases (as expected) with increasing the pulley's moment of inertia, but the changes are less pronounced (no statistically significant difference is observed between small and large flywheels in the driver case, as well as between no flywheel and small flywheel, and between small and large flywheels in the driven case).

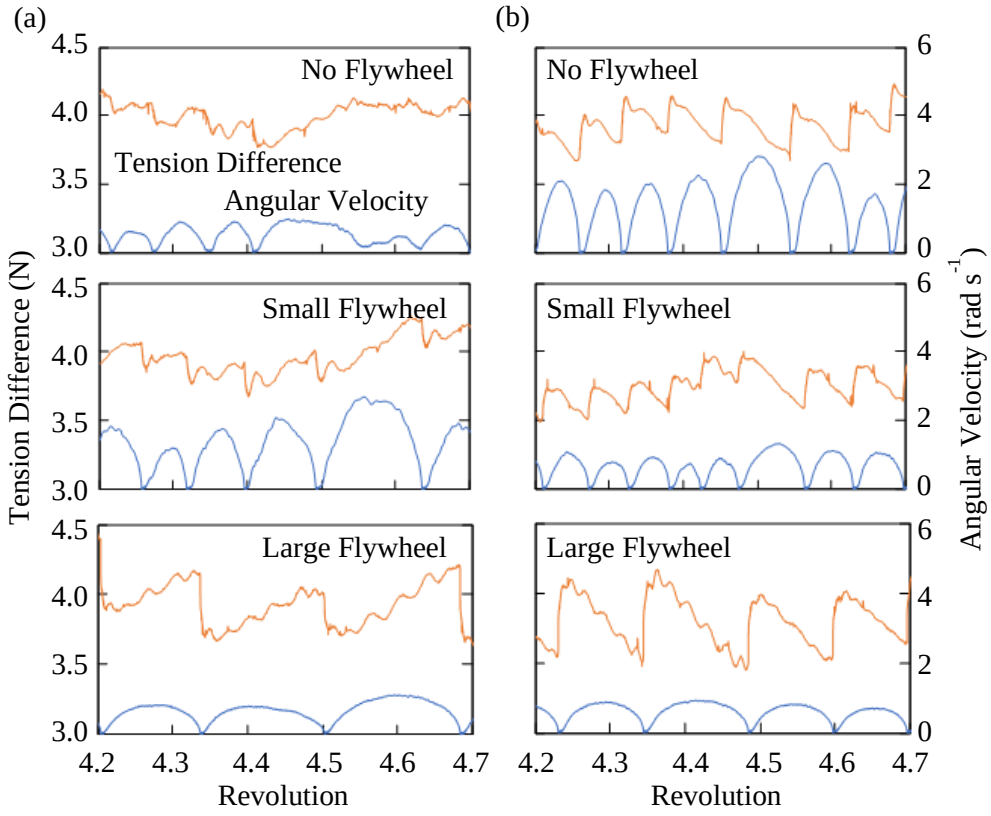

Figure 2-8. Tension difference obtained with and without flywheels in the driver (a) and driven (b) cases.

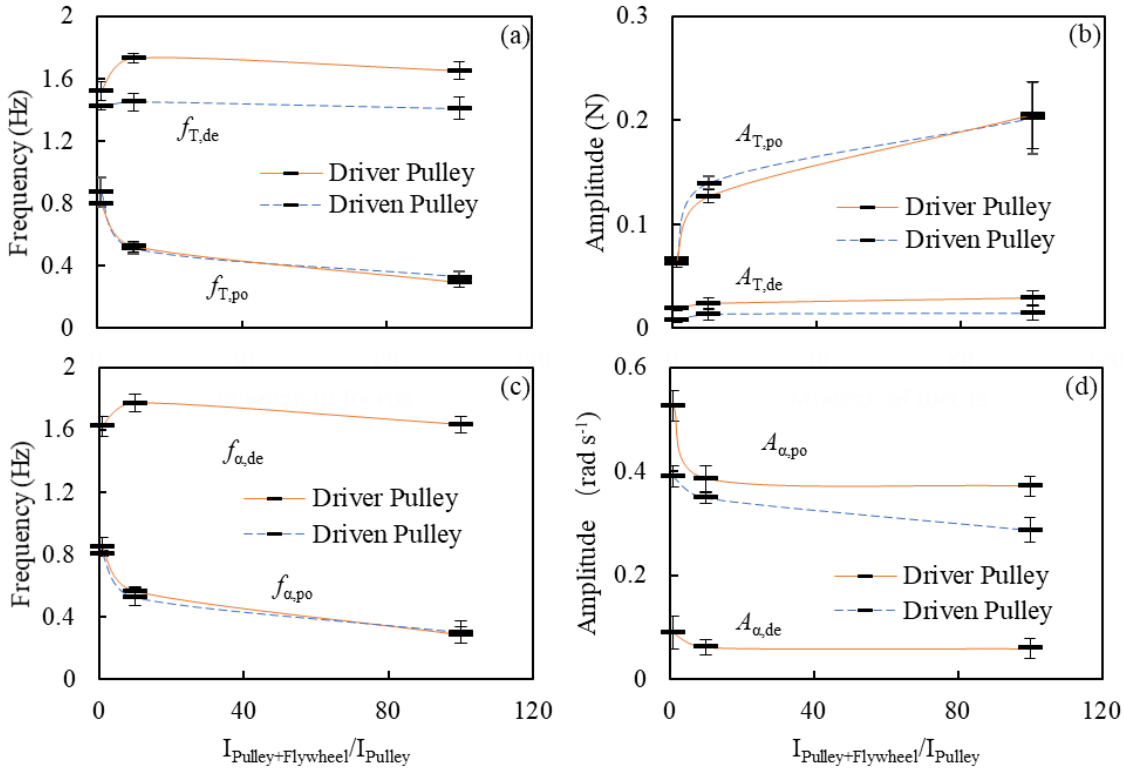

Figure 2-9. The frequency (*f*) and amplitude (*A*) of the fluctuations in the tension difference (T), (a) and (b), respectively, and in the angular pulley velocity (α), (c) and (d), respectively, associated with detachment events (de) and pulley oscillations (po), and presented as a function of the relative pulley's moment of inertia in both the driver and driven cases. The error bars show standard deviation.

The frequencies of the tension difference fluctuations and the angular velocity fluctuations associated with contact instabilities/detachment events ($f_{T,de}$ and $f_{\alpha,de}$, respectively) seem to be independent of the pulley's moment of inertia (no statistically significant difference is observed between any of the tested points in the driven case, as well as between force fluctuations with small and large flywheels, and between velocity fluctuations with no and large flywheel in the driver case). The amplitudes of the tension difference fluctuations and the angular velocity fluctuations associated with contact instabilities/detachment events ($A_{T,de}$ and $A_{\alpha,de}$, respectively) are nearly independent of the pulley's moment of inertia in all cases (statistically significant difference is observed only

between force fluctuations with no and large flywheel in the driver case). The amplitude $A_{T,de}$ in the driver case is larger than that in the driven case because a larger contact area is involved in the detachment events. Thus, based on a comparative analysis of the effect of the pulley's moment of inertia, we can conclude that, to a first approximation, while the force and velocity fluctuations associated with the contact instabilities are not affected, the force and velocity fluctuations associated with the pulley oscillations do depend on the pulley mass.

2.4 Analysis of System's Instabilities

2.4.1 Model of Belt Drive Dynamics

To verify whether contact instabilities can serve as a source of self-oscillation in our system, we developed a simple dynamic model designed in such way that tension difference fluctuations are used as a modulated input, and the pulley's angular velocity is computed as an output and then compared to experimental data. The following assumptions were made:

1) The belt is uniform and perfectly flexible, and it stretches in a quasi-static manner; the two spans of the belt are hence treated as massless linear elastic springs coupled with a massless damper.
2) The belt deformation along the belt width is decoupled from the belt deformation along the belt length.
3) Belt extension $s(t)$ resulting from detachment events is applied uniformly over the exiting portion of the belt.
4) The torque weight is applied to the pulley through an inextensible string.

5) The speed of the belt exiting span and the masses of the loading weights are taken from the experiment.

The diagrams of the model shown in Fig. 2-10 depict a lumped system with 2 degrees of freedom: the angular displacement $\alpha(t)$ of the pulley and the linear displacement $y(t)$ of the tension mass M. The motion of the torque mass m follows directly from the pulley motion at the attachment point. The linear motion of the exiting span of the belt is denoted as $x(t)$ and is prescribed using the constant speed employed in the experiment. Detachment-driven extension in the exit zone is approximated as $s(t)$. The frequency and amplitude of $s(t)$ is estimated based on experimental measurements with one set of loading parameters and then used for all other test points (see Section 2.4.2 for further details).

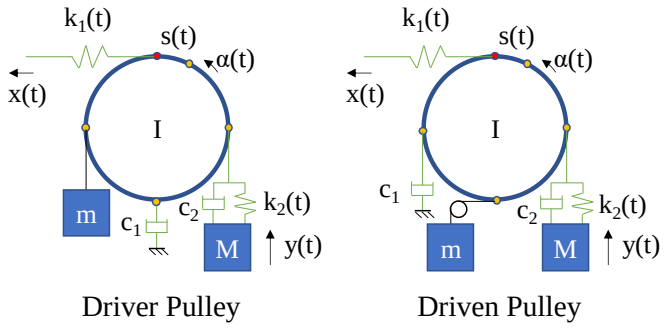

Figure 2-10. Diagrams of a simple belt-drive system defined for the driver and driven cases.

The elongation of the exiting span of the belt $\delta(t)$ can be defined as

$$\delta(t) = x(t) - R\alpha(t) - s(t) \tag{2.1}$$

where R denotes the radius of the pulley. The elongation of the entering span of the belt is the difference between $R\alpha(t)$ and $y(t)$. Hooke's law yields the span stiffness values, $k_1(t)$ and $k_2(t)$, for the exiting and entering belt spans, respectively,

$$k_1(t) = \frac{EA}{l_{01}+x(t)}\text{, and } k_2(t) = \frac{EA}{l_{02}-y(t)} \tag{2.2}$$

where E, A, l_{01} and l_{02} denote the belt elastic modulus, cross-sectional area, and the initial lengths of the exiting and entering spans, respectively. Assuming quasi-static belt stiffness changes, we can derive the governing equations for our belt-drive system (driver pulley, Eq. 2.3a; driven pulley, Eq. 2.3b) as

$$\begin{bmatrix} I+mR^2 & 0 \\ 0 & M \end{bmatrix}\begin{Bmatrix} \ddot{\alpha} \\ \ddot{y} \end{Bmatrix} + \begin{bmatrix} Rc_1+R^2c_2 & -Rc_2 \\ -Rc_2 & c_2 \end{bmatrix}\begin{Bmatrix} \dot{\alpha} \\ \dot{y} \end{Bmatrix} + \begin{bmatrix} R^2(k_1+k_2) & -Rk_2 \\ -Rk_2 & k_2 \end{bmatrix}\begin{Bmatrix} \alpha \\ y \end{Bmatrix} = \begin{Bmatrix} mgR+Rk_1(x(t)-s(t)) \\ -Mg \end{Bmatrix}, \tag{2.3a}$$

$$\begin{bmatrix} I+mR^2 & 0 \\ 0 & M \end{bmatrix}\begin{Bmatrix} \ddot{\alpha} \\ \ddot{y} \end{Bmatrix} + \begin{bmatrix} Rc_1+R^2c_2 & -Rc_2 \\ -Rc_2 & c_2 \end{bmatrix}\begin{Bmatrix} \dot{\alpha} \\ \dot{y} \end{Bmatrix} + \begin{bmatrix} R^2(k_1+k_2) & -Rk_2 \\ -Rk_2 & k_2 \end{bmatrix}\begin{Bmatrix} \alpha \\ y \end{Bmatrix} = \begin{Bmatrix} -mgR+Rk_1(x(t)-s(t)) \\ -Mg \end{Bmatrix}, \tag{2.3b}$$

where c_1 denotes the damping coefficient associated with the pulley oscillations (losses in the belt-pulley contact and bearings) and c_2 denotes the damping coefficient of the free spans of the viscoelastic belt. Both coefficients are assumed to be constant due to an approximately constant length of the contact arc in the first case and a constant total length of the belt in the second case.

2.4.2 Model Verification

The belt extension $s(t)$ in the detachment region is considered to correlate closely to the tension difference fluctuations associated with detachment events (bottom row in Fig. 2-5). Hence, $s(t)$ can be abstracted as a saw-tooth function for both the driver (Eq. 2.4a) and the driven cases (Eq. 2.4b). The frequency of the saw-tooth function is taken as

the frequency $f_{T,de}$ measured in the case with small flywheel for both the driver and driven pulleys. The duty cycles (loading phase fractions) of the saw-tooth function are 2/3 and 1/3 for the driver and driven pulleys, respectively, taken in accord with the tension difference fluctuations associated with detachment events. The amplitude of belt extension, A_s, cannot be defined based on our experimental data. To this end, we have determined A_s via the trial-and-error method: the amplitude of the angular velocity fluctuations ($A_{\alpha,po}$) is calculated by numerical integration of Eq. 2.3 (via Matlab's ode45 routine), while A_s is varied until the predicted $A_{\alpha,po}$ matches the $A_{\alpha,po}$ measured with the small flywheel in both the driver and driven cases. These values are applied to the cases of no and large flywheels to see whether the model can be predictive. The expressions used to describe $s(t)$ are

$$s(t) = \begin{cases} A_s \frac{3f_{T,de}}{4\pi} t, \ 0 \le t \le \frac{4\pi}{3f_{F,de}} \\ A_s \left(3 - \frac{3f_{T,de}}{2\pi} t\right), \ \frac{4\pi}{3f_{F,de}} \le t \le \frac{2\pi}{f_{F,de}} \end{cases} \tag{2.4a}$$

$$s(t) = \begin{cases} A_s \frac{3f_{T,de}}{2\pi} t, 0 \le t \le \frac{2\pi}{3f_{F,de}} \\ A_s \left(\frac{3}{2} - \frac{3f_{T,de}}{4\pi} t\right), \frac{2\pi}{3f_{F,de}} \le t \le \frac{2\pi}{f_{F,de}} \end{cases} \tag{2.4b}$$

All model parameters (Table 2-5) are taken from the experiment except for the two damping coefficients, c_1 and c_2, which were also chosen based on the trial-and-error method to obtain a good agreement between the theoretical and experimental results. The values c_1 and c_2, however, are verified to fall within a reasonable range for PDMS [98].

The equations of motion were numerically integrated using the ode45 function in Matlab, while the real-time belt span lengths updated the stiffness values according to Eq.

2.2. Wavelet routines in Matlab were used to post-process the data from both the numerical model and the experiment. The model was also used to compute the quasi-static vibration modes (eigenfrequencies and eigenvectors) as a function of time (with the instantaneous stiffness values).

Table 2-5. Parameters in the dynamic model.

Nomenclature		Value	
Symbol	Parameter	Driver Case	Driven Case
m	Torque weight, kg	0.4	0.4
M	Tension weight, kg	0.6	0.2
I	Moment of inertia of the pulley, kg·mm^2	15.2	15.2
R	Radius of the pulley, m	0.01	0.01
E	Young's modulus of PDMS, MPa	1.6	1.6
A	Cross sectional area of the belt, mm^2	16	16
v	Driving speed, mm/s	3	3
l_{01}	Initial length of exit span of the belt, m	0.04	0.04
l_{02}	Initial length of entry span of the belt, m	0.36	0.36
g	Gravity, m/s^2	9.81	9.81
c_1	Damping coefficient of the pulley, kg/s	0.04	0.04
c_2	Damping coefficient of the belt, kg/s	0.12	0.12
A_s	Amplitude of the belt extension, μm	10	5
$f_{T,de}$	Frequency of the detachment events, Hz	1.7	1.5

The development of the angular velocity fluctuations in the driver and driven cases is presented using wavelet scalograms in Fig. 2-11 and 2-12, respectively. Dotted white

traces provide the time-varying natural frequencies obtained from the model eigenanalysis. The corresponding vibration modes (at 1.8 min, as denoted by the red dash-dotted line) for the observed two frequencies are shown in Fig. 2-11a. For the lower frequency of the dominant vibration mode, the oscillations of the pulley and the tension weight are similar in scale, while for the higher frequency of the secondary vibration mode, the tension weight oscillations dominate the system response. It is also evident in all plots that the contact instabilities (detachment events) excite the lower frequency vibration mode, whose magnitude grows in time.

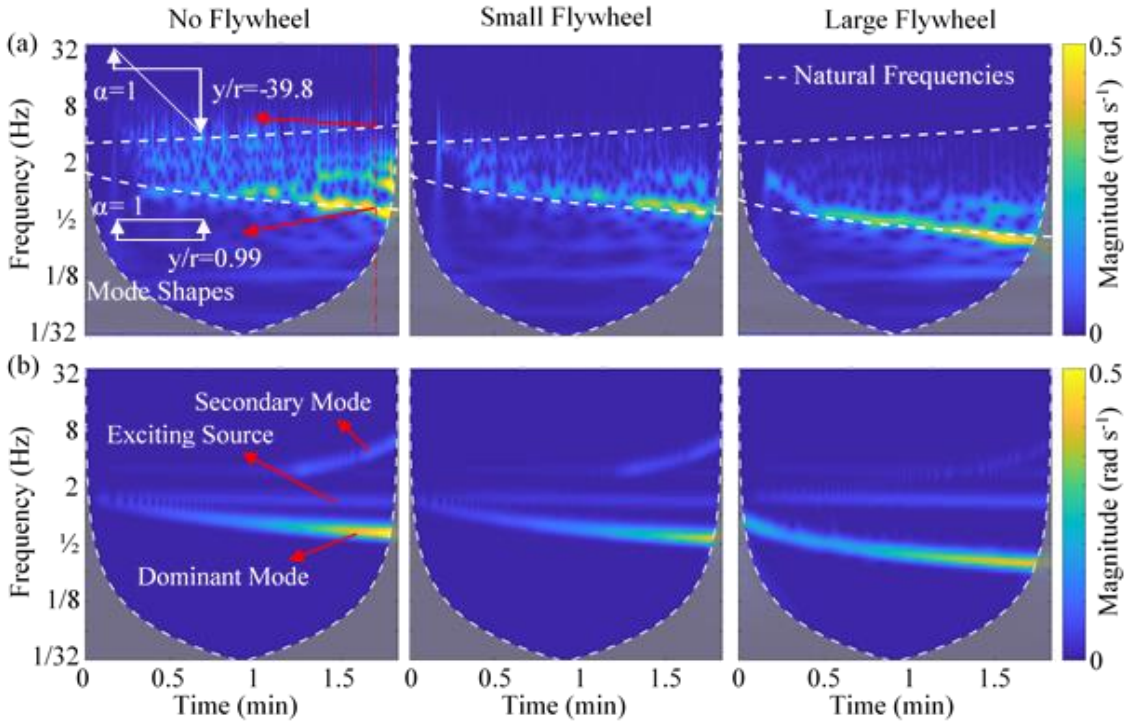

Figure 2-11. Wavelet scalograms of the angular velocity fluctuations obtained from (a) the experiment and (b) the numerical model for the driver pulley equipped with no, small and large flywheels.

The scalograms document strong agreement between the numerical model and the experimental results, and clearly explain the time-dependent frequencies observed in the

experiment. Both the model and the experiment demonstrate a frequency band between the low and high natural frequencies of the angular velocity fluctuations, which is associated with the contact instabilities in the experiment and with the excitation source $s(t)$ in the numerical model. This band is characterized by a fundamental frequency and higher harmonics in the experiment, while the model exhibits only a fundamental frequency due to a simple excitation function encoded in Eqs. 2.4a and 2.4b. Despite these differences and an overall simplicity of the model, the theoretical results match closely the experiment, which provides strong evidence that contact instabilities driven by unmodulated external power are the primary source of the studied system's self-oscillation.

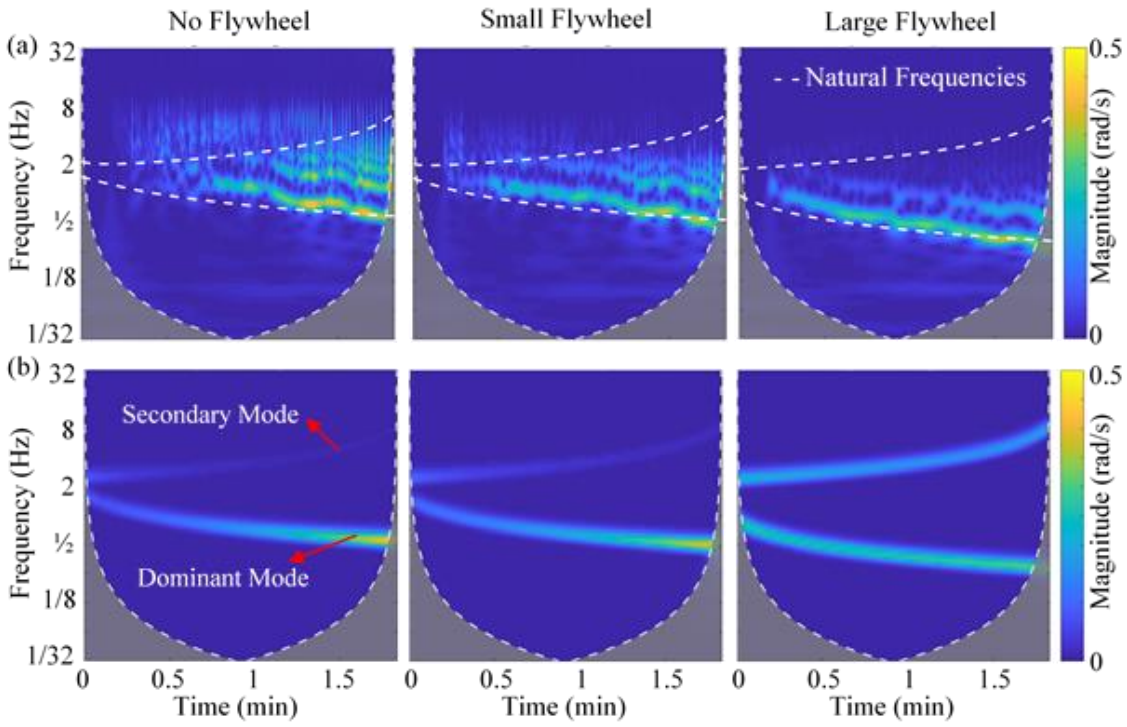

Figure 2-12. Wavelet scalograms of the angular velocity fluctuations obtained from (a) the experiment and (b) the numerical model for the driven pulley equipped with no, small and large flywheels.

As a final comparison, Figure 2-13 details the computational and experimental results obtained at the end of the 4th revolution of the pulley. Consistent with the results shown in Fig. 2-7c and 2-7d, the frequency and the amplitude of the computed angular velocity oscillation in both the driver and the driven cases decrease with increase in the system's inertia, while the maximum discrepancy between the theory and the experiment is less than 10%. Thus, having a formal description of local contact instabilities, we can predict the global dynamic behavior of our belt-drive system.

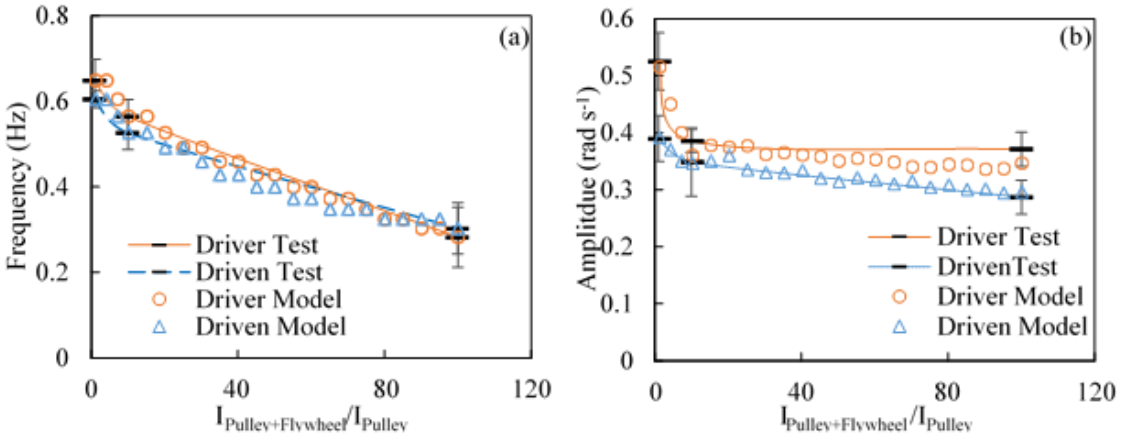

Figure 2-13. The frequency (a) and the amplitude (b) of the angular velocity oscillations obtained from the experiment and numerical model as a function of the relative pulley's moment of inertia in the driver and driven cases.

2.5 Concluding Remarks

To summarize, we highlight the key findings as follows:

1. Under the slow speed considered, no sliding is observed at the belt/pulley interface, and relative displacement between the elastomeric belt and the pulley is achieved by means of cyclic detachment, which calls into question the universal validity of the sliding-based approach to analysis of the belt drive contact.

2. Contact instabilities take place in both the driver and driven pulleys, though the scale of these events is much larger in the first case, which renders the driver pulley as the main source of noise and vibration.

3. The rolling contact mechanics is different in the driver and driven pulleys, which results in much different slip arc angles and calls into question the validity of the symmetric approach to analysis of the belt drive contact.

4. Waves of detachment are observed in the driver pulley, while in the case of the driven pulley, the contact instabilities result from the combination of the pulley rotation and the adhesion hysteresis.

5. A larger applied torque accelerates the occurrence of contact instabilities in the driver case, while all other studied system response quantities remain unaffected.

6. Increasing the driving speed results in an increase in the frequencies of the contact instability occurence and the pulley's angular velocity oscillations, while their amplitudes are essentially unaffected. The former suggests that as transmitted power increases, more power dissipates at the interface, as expected.

7. Surprisingly, increasing the pulley's inertia does not remediate the contact instabilities, but instead leads to more pronounced fluctuations in the belt tension.

8. Crosschecking, we draw similar conclusions based on a simple dynamic model, which provides strong evidence that contact instabilities driven by unmodulated external power are the primary source of the system's self-oscillation.

9. To this end, our main conclusion is that contact instabilities and, hence, the resulting global system's oscillation, most likely cannot be conditioned from outside and instead the main focus must be on the interface itself.

CHAPTER 3. BELT DRIVE MECHANICS

In this chapter, we present an experimental and theoretical investigation into frictional mechanics in a simple belt drive system. To estimate friction experimentally, we perform a thorough stress analysis based on spatio-temporal measurements of the belt tension, traction and contact area evolution. Subsequently, we develop a model taking into account both bulk and surface hysteretic losses for predicting friction in the absence of sliding, and we compare model predictions to experimental observations.

3.1 Method and Means

3.1.1 Apparatus and Operating Conditions

The test set-up (Fig. 3-1) is slightly different from the one described in Chapter 2. The driving system includes a releasing motor and a driving dead weight, which are connected by an inextensible nylon cable wrapped around a pulley, thus constraining the pulley to rotate at a prescribed constant speed. The loading system consists of two adjustable tension weights to control the tension of the belt. Notably, the set-up acts as a driver pulley when the tension weight at the exiting span is smaller than that at the entering span of the belt; otherwise, it acts as a driven pulley. The measurement system contains two cameras. The monochrome digital camera DMK 23UP1300 mounted above the trailing (exit) side of the belt/pulley contact zone, records the contact evolution. A second digital camera (Huawei Honor 8, Shenzhen, China), mounted to the side of the pulley, is used to track the normal and shear strains along the belt/pulley interface. All measurements are synchronized based on the absolute time when the pulley starts to rotate.

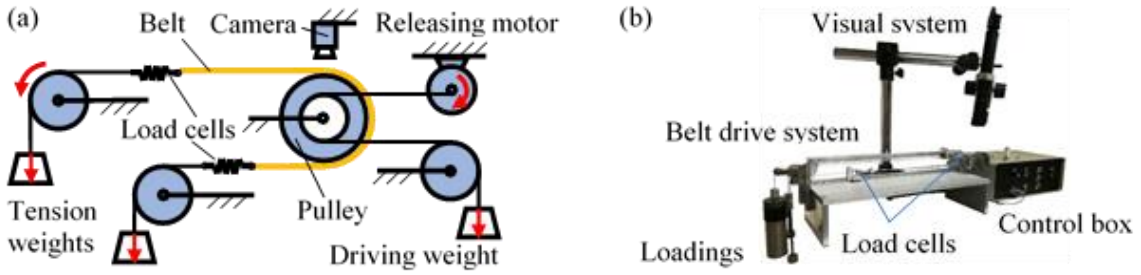

Figure 3-1. The experimental apparatus: (a) schematic and (b) system as built.

Limited by the strength of PDMS, we chose to work with a maximum allowable belt tension of 6 N. The tension on the slack span of the belt was adjusted to 2N. The driving speed and the travel distance of the belt were 3 mm s^{-1} and 300 mm (~5 revolutions of the pulley), respectively. Each test was repeated at least 10 times. The temperature and relative humidity in the laboratory were 20 °C and 10 %, respectively.

3.1.2 Belt Specimen Preparation

The belt specimens were produced by molding polydimethylsiloxane (PDMS, Sylgard 184, Dow Corning, Midland, MI), which is a transparent elastomer. A 10:1 mixture of Sylgard 184 pre-polymer and its cross-linker are cured for 14 h at 65 ^{o}C against a flat smooth template. The storage and loss moduli of PDMS are shown in Fig. 3-2 as a function of loading frequency at room temperature [99], from which the shear modulus can be determined based on its Poisson's ratio of about 0.5. To study the belt deformation while the system is in operation, evenly distributed tick marks with ~0.125 mm intervals were created on the belt sidewall during molding by using a custom template (Fig. 3-3). Finally, a belt specimen of 400 mm in length, 8 mm in width and 3 mm in thickness was cut from the mold.

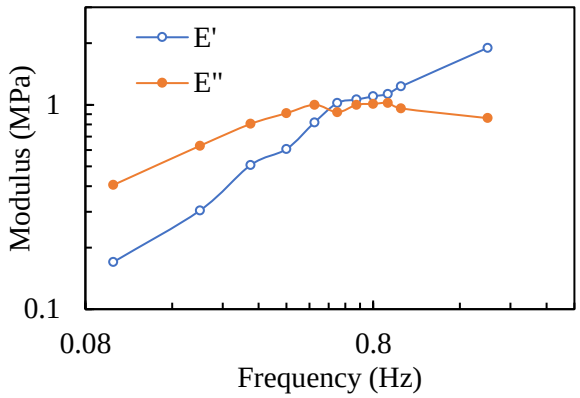

Figure 3-2. Storage modulus E' and loss modulus E" of PDMS obtained as a function of frequency at room temperature.

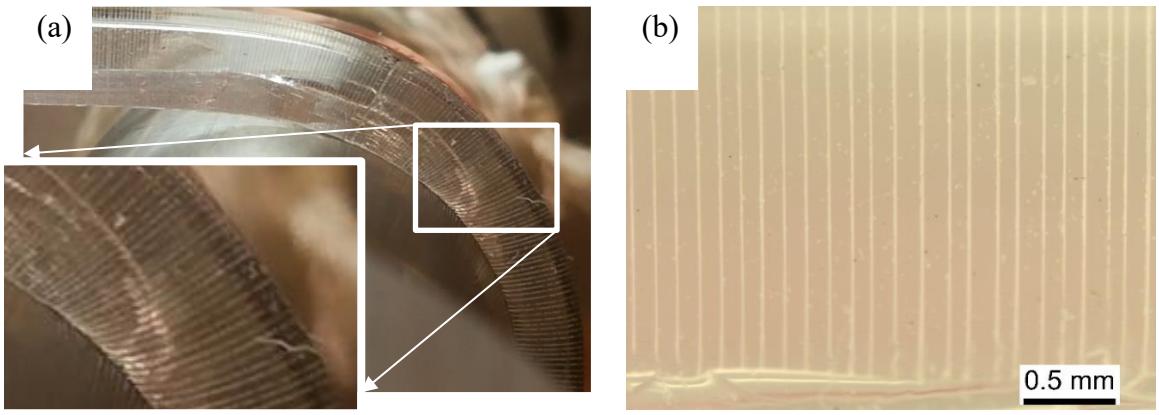

Figure 3-3. (a) Deformed and (b) undeformed tick marks created on the belt sidewalls for shear strain measurements.

3.2 Belt Deformation and Contact Behavior

3.2.1 Spatial Characterization

To analyze the belt-drive mechanics, we evaluate the shear strain, the longitudinal stretching strain, and the contact status of the belt as a function of position. An illustrative example of an instantaneous belt state is shown in Fig. 3-4. The shear strain is obtained by quantifying the deformation of the tick marks (Fig. 3-3a). The longitudinal stretching strain

is estimated based on the Poisson's effect while using the measured transverse strain (the difference between the deformed and undeformed belt thickness divided by its undeformed thickness). The contact status is determined by the light interference at the belt/pulley interface.

In the driver case, we analyze the instant at which a fold (the isolated non-contact region shown as a white strip in Fig. 3-4a) is formed at the exit zone. The distribution of shear (according to the usual sign convention, in our case, it is positive when the pulley drives the belt) and stretching strains correlates well with the contact area. The shear strains at the belt/pulley interface are observed from 25° to 85° and are zero elsewhere. Along the direction of the belt motion (see inset in Fig. 3-4a), the shear strain at the belt-pulley interface starts to develop gradually at 85°, then it grows dramatically from 52° to 40° and then it drops down to almost zero within the next 10°. Interestingly, the position of the maximum shear strain coincides with the right edge of the fold; hence, the fold and the region to its left is actually a relaxation zone, transmitting no tangential force regardless of whether this region is in contact or not. The variation of stretching strain takes place over a 30° arc immediately before the relaxation zone (yellow shade shown in Fig. 3-4a), where the shear strain maximum is also located.

In the driven case (Fig. 3-4b), the belt shows a much more stable behavior than in the driver case, with larger contact area and no waves of detachment observed at the belt-pulley interface. Similar to the driver case, the shear strains start building up close to the transition from the adhesion to the slip arc and then they relax abruptly when the belt detaches from the pulley. It is worth noting here that the detachment mechanisms for the two cases are different, with the balance between the traction and tension moments being

the reason of detachment in the driver case, and the combination of the pulley rotation and the adhesion hysteresis being the reason of detachment in the driven case. Although the shear strains (negative when the pulley is driven by the belt) are observed along a larger arc (from about 85° to 5°), their magnitude and peak width are much smaller than those in the driver case. Similar to the shear strains, the variation of the stretching strain (yellow shade shown in Fig. 3-4b) from the slack to the tight belt spans takes place over a smaller arc than that in the driver case.

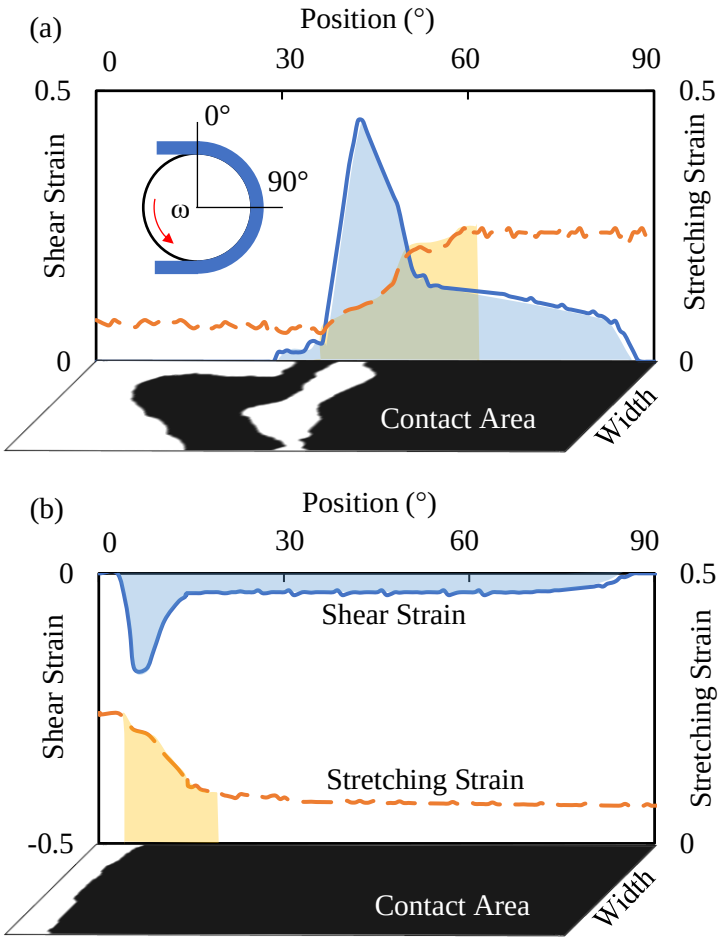

Figure 3-4. Instantaneous shear strain (solid line), stretching strain (dashed line), and the contact status (black area denotes contact) at the belt-pulley interface for (a) the driver and (b) the driven cases.

Interestingly, some negative shear is observed over a small region around the belt entry in both the driver and driven cases in the middle layer of the belt, which is visualized by an S-shaped geometry of tick marks (Fig. 3-5). Comparing one of the deformed tick marks to the reference radial lines (Fig. 3-5a), we see zero shear at the belt-pulley interface as well as in the outer layer of the belt, while an obvious shear is present in the middle layer of the belt. The explanation for this effect is that the outer layers of the belt have to accelerate in order to start moving with a higher tangential speed when the belt seats on the pulley. This acceleration is allowed by a gradual extension of the outer layers in a free span of the belt immediately prior to forming a contact with the pulley. Having different longitudinal extension along the belt thickness results in a longitudinal shear we observe in the transient zone of the belt/pulley engagement.

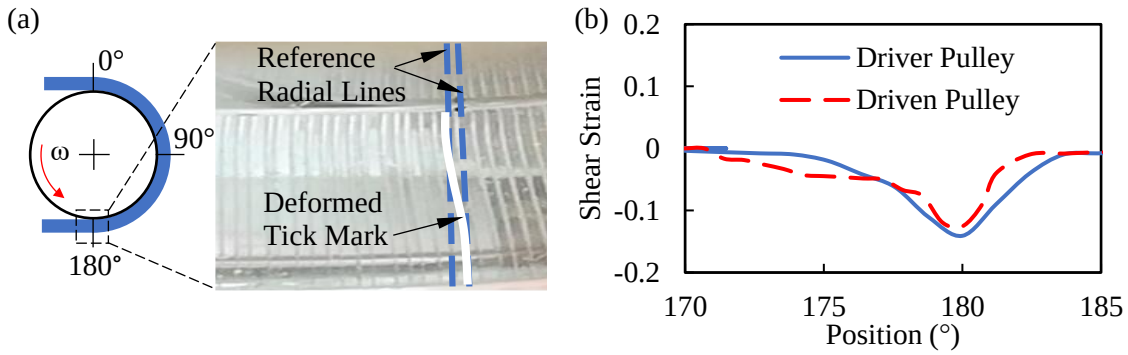

Figure 3-5. The visualization (a) and the distribution (b) of the negative shear strain at the middle layer of the belt at the entry zone.

To estimate mechanical losses due to rolling friction, we analyze free-body diagrams of the belt segment wrapped around the pulley in both the driver and the driven cases, as shown in Fig. 3-6. The sum of all moments around the pulley axis is zero as the distributed belt angular momentum does not change with time (steady operation). These moments result from normal and shear traction at the belt-pulley interface, and from normal

(tension) and shear forces together with moments that are applied at the free belt spans. The input moment needed to maintain rotational movement of the belt comes from the shear traction at the belt-pulley interface in the driver case, or from the normal (tension) force applied by the free belt spans in the driven case. The useful output moment results from the normal (tension) force applied by the free belt spans in the driver case, or from the shear traction at the interface in the driven case. All other moments sum to a cumulative moment that can be called the moment of rolling resistance, or the rolling friction moment. This cumulative moment is evaluated by substituting experimental data on the moment of shear traction and the moment of tension difference into the equation of moment equilibrium ($\Sigma M = 0$).

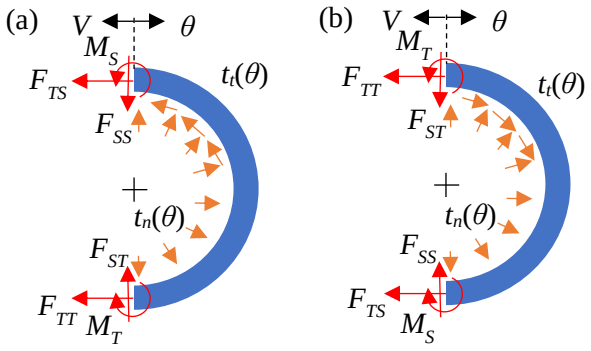

Figure 3-6. Free body diagrams of the belt segment in contact with (a) the driver and (b) the driven pulleys. F_{TT} and F_{TS} represent tension (normal) forces, F_{ST} and F_{SS} represent shear forces, and M_T and M_S represent moments at the tight and slack spans of the belt, and t_n and t_t represent normal and tangential (shear) traction at the belt/pulley interface.

Assuming a uniform shear strain distribution along the belt width, the total tangential traction can be estimated via integration of the shear strain multiplied by the shear modulus over the entire contact arc (see blue shades in Fig. 3-4). Due to the dependence of the shear modulus of PDMS on loading frequency, the shear moduli for the

driver and driven cases can be estimated as 0.51 and 0.52 MPa respectively from Fig. 3-2 with the average frequency of various loading modes to which the belt is subject (more details on loading modes are discussed in Section 3.3.1). This results in moments due to the tangential (shear) traction forces about the pulley axis of 0.070 N·m (input) and -0.034 N·m (useful output) for the driver and driven cases, respectively. The moment due to the difference in the tension forces is equal to -0.046 N·m in the driver case (representing the load/useful output when the pulley drives the belt) and to 0.047 N·m in the driven case (representing the power source/input when the pulley is driven by the belt). It is worth noting here that, in the driver case, the shear traction moment is responsible for driving the rotational motion of the belt, and thus its magnitude must exceed the tension moment magnitude if a resistance to rolling motion is present. In contrast, in the driven case, the tension moment drives the rotational motion, and thus its magnitude must be greater than the shear traction moment in the presence of rolling friction. Based on the moment equilibrium, the rolling friction moments are estimated to be -0.024 N·m and -0.013 N·m in the driver and driven cases, respectively. Interestingly, the rolling friction moment is much higher in the driver case; this results from the appearance of the waves of detachment that are characteristic for this case only and suggests that they represent a great energy sink.

3.2.2 Temporal Characterization

Since the contact state, as well as the contact instabilities (detachment events), develop in time, we herein conduct a spatio-temporal study on the shear traction and the contact evolution. A cluster of contact characteristics shown at different time frames is documented in Fig. 3-7 for both the driver and the driven cases. This figure highlights the formation, propagation and disappearance of detachment waves in the driver case. In

contrast to Fig. 3-4, which is a sub-plot extracted from Fig. 3-7 (frame 82:48 for the driver pulley and frame 84:00 for the driven pulley), the negative shear strain for the driven pulley is presented as an absolute value.

For the driver pulley, the shear and stretching strains change in accordance with the contact area evolution, with the detachment waves forming and disappearing. The shape of the shear distribution remains almost the same in time, while its peak moves back and forth together with the front of the adhesion zone, and the isolated re-formed contact region at the relaxation zone does not contribute much to traction. Studying the shear traction obtained via integration of the shear strains, we see that shear reaches a minimum when the belt is detached from the pulley at the relaxation zone (82:24, 83:00 and 83:48 in Fig. 3-7a), and it reaches a maximum when the belt is in contact with the pulley in the relaxation zone (82:44 and 83:28 in Fig. 3-7a). Interestingly, the drop in stretching strain is also tied to the adhesion arc front, and it moves together with the shear strain peak. For the driven pulley, the shear strain peak and the stretching strain rise are also tied to the adhesion zone front, and hence their location does not change appreciably due to the less violent detachment mechanism operating there.

Analyzing the time-related changes in the moments due to the tension difference and the shear traction, and the changes in the contact ratio (the ratio of the real contact area A_r, the area of a black zone, over the nominal contact area A_n, the area of a whole strip), we see a good correlation. This means that the detachment events affect both the tension difference and the shear traction. However, it is obvious that the fluctuations induced by the detachment events are much larger in the driver case, which is associated with a more violent character of the detachment waves that appear in this case only.

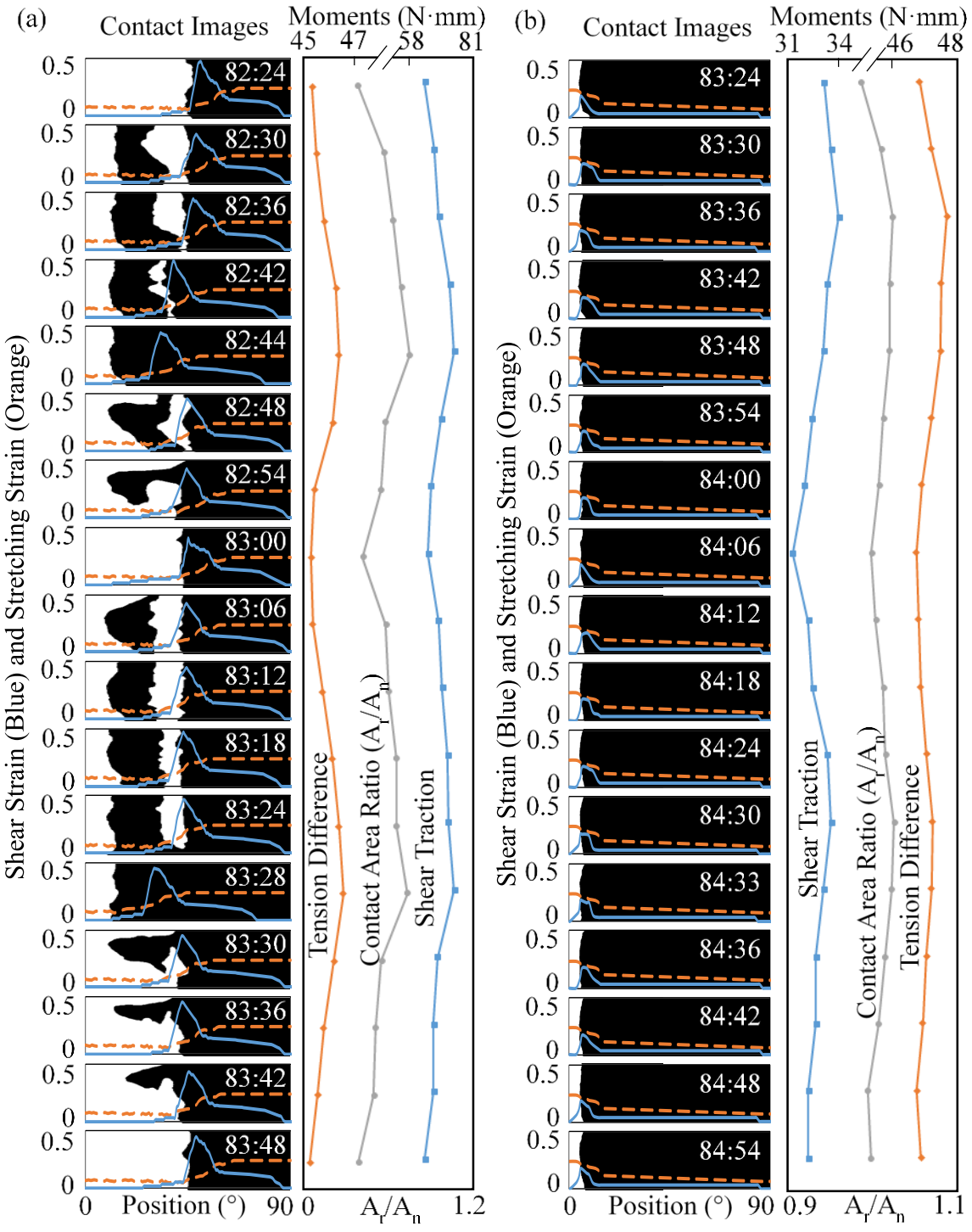

Figure 3-7. Plots of shear strain, stretching strain and contact area at the belt interface at several time frames as well as the correlation of corresponding tension difference, shear traction and contact ratio for both the (a) driver and (b) driven pulleys.

3.3 Analysis of Mechanical Losses

Energy can be dissipated as heat in the isolated belt mainly via two means: 1) viscoelastic deformation of the belt material and 2) detachment events at the belt-pulley interface. Both components are analyzed in this work to estimate the mechanical losses in both the driver and the driven cases.

3.3.1 Volumetric Hysteresis Losses

PDMS used as the belt material exhibits a viscoelastic behavior, leading to energy losses under cyclic loadings. The amount of energy lost in one complete cycle of loading/unloading is shown in Fig. 3-8 and it equals to $\oint \sigma d\varepsilon$ [100]. The dissipated energy per unit volume $\overline{W_V}$ can be approximated using the following formula:

$$\overline{W_V} = \pi E'' \varepsilon_a^2 \tag{3.1}$$

where E'' is the loss modulus of the belt material and ε_a is a given strain value for which the energy loss is calculated. The modulus of viscoelastic materials is generally expressed using the complex representation $E=E'+iE''$, where E' and E'' denote the storage and loss moduli of the material, respectively, while i is the imaginary unit, and both moduli are temperature- and frequency-dependent, $E= E(f, T)$.

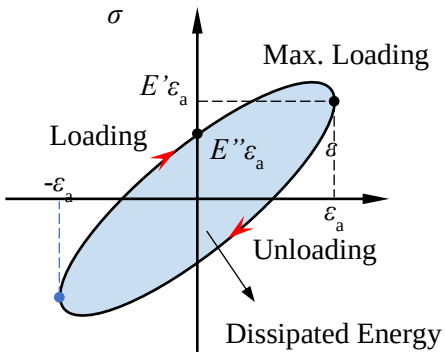

Figure 3-8. Energy dissipated by a viscoelastic material under cyclic loading.

Figure 3-8 shows the case of cyclic loading under which the strain varies within an interval (-ε_a, ε_a). However, in our case, the strain varies from null to ε_a (the direction of the load applied is constant). To this end, we can substitute ε_a in Eq. 3.1 with $\varepsilon_a/2$,

$$\overline{W_V} = \frac{1}{4}\pi E''\varepsilon_a^2 \tag{3.2}$$

Silva et al. [43] developed a model to estimate the power losses due to hysteresis in poly-V belt transmissions. Herein, the model is modified to include adjustments for a flat belt and for the hysteresis due to the detachment events at the belt-pulley interface. Five modes of cyclic loading were considered: bending, stretching, radial compression, shear and detachment-induced fluctuations in stretching. According to Eq. 3.1, the specific loss modulus and strain needed to be determined for each loading mode. The loss modulus was obtained as a function of frequency from a database [99], while both the characteristic frequency and maximum strain values were estimated based on our tests in accord with the corresponding loading modes. The characteristic frequency f of each loading mode was related to the region where it occurs, as follows:

$$f = \frac{V}{L} \tag{3.3}$$

where V is the travelling velocity of the belt and L is the length over which this load is applied.

Bending: The belt bends when it runs onto the pulley and straightens when it runs off the pulley. Hence, the transition regions, where the belt bending changes between none and final curvature, take place at the inlet and outlet of the belt rather than over the entire arc of contact. These transitions are associated with the arcs of approximately 10° at the low-tension span and 3° at the high-tension span. Based on beam theory, the bending strain ε_{a_b} is proportional to the distance from the neutral axis and the curvature of the neutral axis. For a homogeneous isotropic belt with rectangular cross section loaded in bending only (superposition assumption), the neutral axis is in the belt center as shown in Fig. 3-9. Hence, the bending strain ε_{a_b} can be expressed as

$$\varepsilon_{a\_b} = \frac{y}{R + t/2} \tag{3.4}$$

where t is the thickness of the undeformed belt, and y is the distance from the neutral axis (the bending-induced change in the belt thickness is neglected because the difference is small compared to the radius of the pulley).

The bending-induced energy loss per unit belt length, W_{V_b}, can be calculated via integration of Eq. 3.2 over the whole cross-sectional area

$$W_{V\_b} = \frac{1}{4}\int_{-\frac{t}{2}}^{\frac{t}{2}} \pi E"(f_b)\varepsilon_{a\_b}^2 B dy \tag{3.5}$$

where B denotes the belt width and $E"(f_b)$ is the loss modulus obtained for the bending frequency f_b.

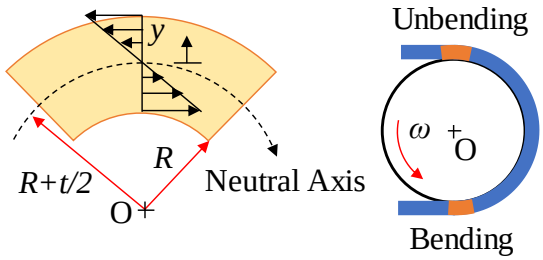

Figure 3-9. Schematic of the bending strain of a certain segment of the belt in contact with the pulley.

Stretching: Changes in stretching strain are visualized in Fig. 3-4 using yellow shades. These changes happen due to variation in tension ΔF_T. The stretching strain value ε_{a_st} can be calculated via Hooke's law:

$$\varepsilon_{a\_st} = \frac{\Delta F_T}{E'(f_{st})A} = \frac{F_{TT} - F_{TS}}{E'(f_{st})A} \tag{3.6}$$

where F_{TT} and F_{TS} are the tight and slack belt span tensions around the pulley, and $E'A$ is the strain stiffness along the belt, with $E'(f_{st})$ being the storage modulus in the longitudinal direction for the stretching frequency f_{st} and A being its cross-sectional area.

The stretching-induced energy loss per unit length of the belt, W_{V_st}, can be calculated as

$$W_{V\_st} = \frac{1}{4}\pi E''(f_{st})\varepsilon_{a\_st}^2 A \tag{3.7}$$

where $E''(f_{st})$ is the loss modulus obtained for the stretching frequency f_{st}.

Radial compression: The belt segment in contact with the pulley is subjected to radial compression, yielding the corresponding strain ε_{a_rc} which can be calculated using Hooke's law,

$$\varepsilon_{a\_rc} = \frac{t_n}{E'_{rc}(f_{rc})} \tag{3.8}$$

where t_n is the normal traction and E'_{rc} is the storage modulus adjusted for radial compression because of the plane strain conditions. This adjustment implies

$$E_{rc}(f_{rc}) = \frac{E(f_{rc})}{1-\nu^2} = \frac{E'(f_{rc})}{1-\nu^2} + i\frac{E''(f_{rc})}{1-\nu^2} \tag{3.9}$$

where ν denotes the Poisson's ratio of the belt material. The normal traction t_n, which is responsible for the radial compression-induced energy loss, is given as

$$t_n(\theta) = \frac{F_T(\theta) - F_C}{R \cdot B} \tag{3.10}$$

where the tension force F_T ranges from F_{TS} to F_{TT}, and F_C denotes the centrifugal force (neglected here due to the small belt inertia). Although the belt is compressed radially along the whole contact with the pulley, the loading/unloading process is assumed to take place mostly where tension changes (yellow shaded region shown in Fig. 3-4).

The radial compression-induced energy loss per unit belt length, W_{V_rc}, can be calculated as

$$W_{V\_rc} = \frac{1}{4}\pi E_{rc}^{"}(f_{rc})\varepsilon_{a\_rc}^{2}A \tag{3.11}$$

where the maximum strain value ε_{a_rc} is used.

Shear: As stated in Section 3.2.1, shear deformation at the belt/pulley interface was found in the belt exit zone only (see blue shaded region in Fig. 3-4). However, an additional small negative shear deformation was observed within the belt itself around the region of the belt engagement with the pulley in both the driver and driven cases (Fig. 3-5). This secondary shear zone appears as a result of the speed difference between the outer and inner layers of the belt when it seats on the pulley [23]. The two regions of shear strain contribute to the energy losses separately, since each of them forms a complete hysteresis cycle independently, and the maximum shear strains γ_a for both zones can be measured. Hence, the shear-induced energy loss per unit belt length at the entry zone, $W_{V\_sh\_en}$, and at the exit zone, $W_{V\_sh\_ex}$, can be calculated as

$$W_{V\_sh\_en} = \frac{1}{4}\pi A G_{en}^{"}(f_{sh\_en})\gamma_{a\_en}^{2} \tag{3.12a}$$

$$W_{V\_sh\_ex} = \frac{1}{4}\pi A G_{ex}^{"}(f_{sh\_ex})\gamma_{a\_ex}^{2} \tag{3.12b}$$

where the subscripts *ex* and *en* denote the exit and entry zones, respectively, and $G"$ is the shear loss modulus of the belt material, which can be obtained using the following formula for homogeneous and isotropic material

$$G" = \frac{E"}{2(1+\nu)} \tag{3.13}$$

Stretching fluctuation: Formation of the detachment waves at the exit zone results in relatively rapid fluctuations in stretching. Although the amplitude of the induced fluctuations in tension, ΔF_{T_dw}, is small, they can have considerable effect due to their high frequency. The corresponding strain value can be calculated from Hooke's law,

$$\varepsilon_{a\_dw} = \frac{\Delta F_{T\_dw}}{E'(f_{dw})A} \tag{3.14}$$

Then, the stretching fluctuation-induced energy loss per unit belt length, W_{V_dw}, can be calculated as

$$W_{V\_dw} = \frac{1}{4}\pi E"(f_{dw})\varepsilon_{a\_dw}^2 A \tag{3.15}$$

where the frequency of the detachment waves f_{dw} can be determined by analyzing the tension force data.

Once all components of the energy loss per unit belt length have been defined, given that all dissipative forces except shear act at the middle layer of the belt in the direction of

the belt length, while the shear traction acts at the belt-pulley interface, the equivalent dissipative moment M_V can be determined using the following equation,

$$M_V = \sum r \cdot F_V = R \cdot W_{V\_sh\_ex} + (R + \frac{t}{2}) \cdot \sum W_V \tag{3.16}$$

3.3.2 Surface Hysteresis Losses

The energy dissipation due to an adhesion (surface) hysteresis is the difference between the energy spent during detachment and the energy gained during attachment.

Detachment: The energy spent during detachment can be quantified by treating the detachment process as a fracture process taking place at the interface between two layers [63]. It is known that the energy required to create a unit area at the opening crack tip H_{oc} depends on the crack propagation speed and that it is larger than the work of adhesion H_0, so

$$H_{oc} = H_0 \left(\frac{v_{oc}}{v_0}\right)^{\alpha} \tag{3.17}$$

where v_{oc} is the speed of the opening crack tip, v_0 is a characteristic crack propagation speed and α is a constant; all related to the viscoelasticity of the material.

Attachment: The energy gained during attachment can be quantified by treating the attachment process as a healing process between two layers [101]. However, despite being dependent on the crack propagation speed as well, the energy per unit area gained at the closing crack tip H_{cc} is generally smaller than the work of adhesion H_0,

$$H_{cc} = H_0 \left(\frac{v_0}{v_{cc}}\right)^{\alpha} \tag{3.18}$$

where v_{cc} is the speed of the closing crack tip.

To simplify our model, we treat the adhesion hysteresis as follows. In both the driver and driven cases, the belt attaches to and detaches from the pulley with speeds that are equal to the speeds of the belt motion on the tight and slack sides. This results in the adhesion energy being gained or spent when the contact is formed or lost, and it serves as one source of adhesion hysteresis. In addition to this (normal) detachment/attachment, the belt experiences a fast and violent contact rupture when a wave of detachment forms in the driver case. The total energy dissipated due to adhesion hysteresis can be obtained by the superposition of the two components.

For the seating/unseating of the belt, to a first approximation, the associated speed of the opening and closing cracks is equal to the driving speed. However, finding the speed of the opening and closing cracks related to the detachment waves formed at the relaxation zone is much more difficult. To this end, we assume that (1) the edges of the contact area lost/gained due to detachment waves always propagate in the direction opposite to the belt motion, and that (2) the speed of the opening and closing cracks due to detachment waves, V_{dw}, is based on the contact area change in the relaxation zone (see Fig. 3-7):

$$V_{dw} = \frac{1}{B}\frac{\Delta A_c}{\Delta t} + V \tag{3.19}$$

where ΔA_c denotes the lost/gained contact area (positive when lost) between a specific frame and one frame after it, Δt denotes the corresponding time period, and the shape of the changed contact area is ignored to simplify the model. Since the contact area shown in Fig. 3-7 is imaged in the Eulerian frame of reference, the speed of the detachment waves with respect to the pulley is complemented by the driving speed V. Analyzing the propagation of the detachment waves, we associate positive speed with detachment and negative speed with attachment.

The power dissipated due to the adhesion hysteresis, P_{S_ER} and P_{S_EN} for the driver and driven pulleys, respectively, can be computed as

$$P_{S\_ER} = H_{dw}BV_{dw} + H_{sitting/unsitting}BV$$

$$= \begin{cases} H_0\left(\frac{V_{dw}}{v_0}\right)^{\alpha} BV_{dw} + \left[H_0\left(\frac{V}{v_0}\right)^{\alpha} - H_0\left(\frac{v_0}{V}\right)^{\alpha}\right]BV, V_{dw} \geq 0\,; \\ -H_0\left(\frac{v_0}{|V_{dw}|}\right)^{\alpha} BV_{dw} + \left[H_0\left(\frac{V}{v_0}\right)^{\alpha} - H_0\left(\frac{v_0}{V}\right)^{\alpha}\right]BV, V_{dw} < 0. \end{cases} \quad (3.20a)$$

$$P_{S\_EN} = H_{sitting/unsitting}BV = \left[H_0\left(\frac{V}{v_0}\right)^{\alpha} - H_0\left(\frac{v_0}{V}\right)^{\alpha}\right]BV. \quad (3.20b)$$

when the first term present in the driver case can be safely neglected in the driven case due to a less dramatic area fluctuation at the relaxation zone. Hence, given that the surface hysteresis losses happen at the belt-pulley interface, the equivalent dissipative moment M_{S_ER} and M_{S_EN} can then be computed as

$$M_{S\_ER} = R\frac{P_{S\_ER}}{V}$$

$$= \begin{cases} H_0\left(\frac{V_{dw}}{v_0}\right)^{\alpha} B\frac{V_{dw}}{V}R + \left[H_0\left(\frac{V}{v_0}\right)^{\alpha} - H_0\left(\frac{v_0}{V}\right)^{\alpha}\right]BR, V_{dw} \geq 0\,; \\ -H_0\left(\frac{v_0}{|V_{dw}|}\right)^{\alpha} B\frac{V_{dw}}{V}R + \left[H_0\left(\frac{V}{v_0}\right)^{\alpha} - H_0\left(\frac{v_0}{V}\right)^{\alpha}\right]BR, V_{dw} < 0. \end{cases} \quad (3.21a)$$

$$M_{S\_EN} = R\frac{P_{S\_EN}}{V} = \left[H_0\left(\frac{V}{v_0}\right)^{\alpha} - H_0\left(\frac{v_0}{V}\right)^{\alpha}\right]BR. \quad (3.21b)$$

3.3.3 Model Verification

Based on the above modeling, the dissipative moments in both the driver and the driven cases are obtained for the parameters shown in Table 3-1, which are either prescribed for/measured from the test or taken from Ref. [102] (the latter ones are marked in grey in Table 3-1). The storage and loss moduli of PDMS, shown in Fig. 3-2 as a function of loading frequency at room temperature [99], are also used in the model calculations.

The moments of rolling friction, which are estimated based on the moment equilibrium and computed based on the model described in Sections 3.3.1 and 3.3.2 when using the results shown in Figs. 3-4 and 3-5, are compared in Fig. 3-10. Yellow slices indicating the computed rolling friction are shown on top of the orange slices of the experimentally estimated rolling friction. A good match between them implies a reasonable prediction made by the model, with the relative errors for the computed rolling friction being equal to 17.4% and 13.8% for the driver and driven cases, respectively.

Table 3-1. Parameters used in the model.

Nomenclature		Value (Driver/Driven)
Symbol	Parameter	
F_{TS}	Tension at the slack span, N	2
F_{TT}	Tension at the tight span, N	6
R	Radius of the pulley, mm	10
v	Poisson's ratio	0.499
B	Width of the belt, mm	8
t	Thickness of the belt, mm	3
V	Driving speed, mm s^{-1}	3
A	Belt cross section area, mm^2	24
γ_{a_ex}	Max. shear strain at the exit zone	(0.45/0.18)
γ_{a_en}	Max. shear strain at the entry zone	0.16
f_{dw}	Detachment wave frequency, Hz	(1.43/1.33)
ΔF_{T_dw}	Tension fluctuation, N	(0.05/0.04)
H_0	Work of adhesion, mJ m^{-2}	44
v_0	Characteristic crack speed, μm s^{-1}	0.1
α	Exponent	0.33

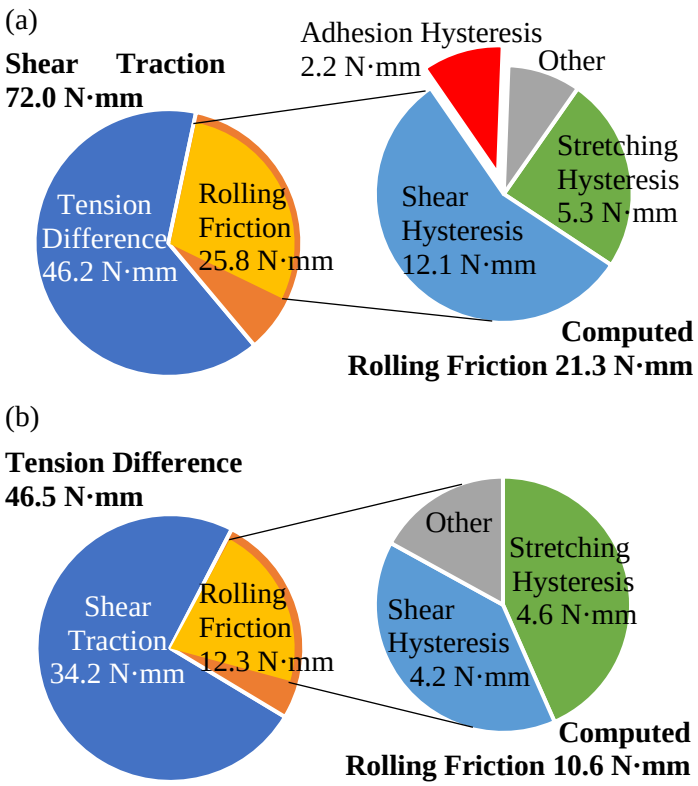

Figure 3-10. Moments applied to the belt wrapped over (a) the driver and (b) the driven pulleys.

Based on the effective match between the experimentally and theoretically obtained rolling friction, we can analyze the contributions of different energy sinks to the mechanical losses in the studied belt-drive. For both the driver and the driven cases, the volumetric hysteresis losses represent the greatest part of the energy losses, among which the shear- and stretching-induced losses dominate. It is worth noting that the surface hysteresis losses induced by the detachment waves play a significant role in rolling friction for the driver case, accounting for about 10% of the total losses. This result also supports our observation that a driver pulley generates more noise and vibration than a driven pulley. Thinking about practical applications and remediation of the problem, one may consider breaking edge-to-edge large-scale waves of detachment (Fig. 3-7) into small-scale events

by regular surface texturing (studied in Chapter 4), which was shown to reduce frictional fluctuations in sliding [89, 103] and may work similarly in rolling. Remarkably, some commercial belts that claim to "quiet" the belt during operation implement crosscuts on their contact side, which most likely represents a result of trial-and-error approach to solution of the problem. Our next work is devoted to the exploration and analysis of this topic.

Interestingly, the temporal evolution of the experimentally obtained mechanical losses can be also explained/modeled using the above approach. Repeating the computation for each time frame shown in Fig. 3-7, the modeled shear traction moments are obtained in accord with the moment equilibrium by adding/subtracting the corresponding computed rolling friction moments to/from the moments generated by the tension difference. The results are presented in Fig. 3-11 along with the experimental data. Although further work is needed to verify the efficacy of this model at higher speeds, the agreement between the model and the experiment is good for both the driver and the driven cases under the slow speed considered. An underestimation of the rolling friction moment in both cases can be associated with the oversimplification of the adhesion hysteresis analysis and with the neglect of the belt deformation in the direction of its width. In addition, Fig. 3-11 appears to be instrumental in demonstrating that the tension difference does not match the frictional forces (in contrast to a widely accepted misconception that can be traced back to the belt creep theory, as stated in [13]), and that the power is transmitted by the shear traction and is dissipated by the rolling friction.

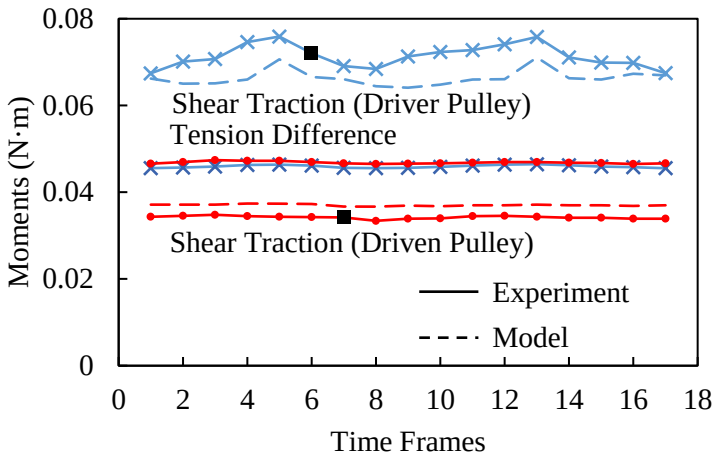

Figure 3-11. Comparison between the experimental and computational results for the evolution of the moments acting on the belt in the driver and driven cases. Black solid squares for both pulleys denote the specific frames extracted for the detailed plots shown in Fig. 24.

3.4 Concluding Remarks

To summarize, we highlight the key findings as follows:

1. The measured distribution of the shear strain at the belt-pulley interface shows a significant difference between the driver and the driven pulleys due to a unidirectional flow of power, while mechanical losses are much higher in the driver case.

2. The shear strains drop at the transition from the adhesion arc to the slip arc, and, in contrast to both the elastic creep and the belt shear theories, the slip arc practically does not contribute to power transmission (at least in the studied case).

3. Additionally, our model reveals that the contact area evolution correlates to the shear traction changes, and that the shear- and stretching-induced energy losses dominate in rolling friction for both the driver and driven cases. A significant contribution of the waves of detachment to the energy dissipation explains much higher mechanical losses in the driver case.

CHAPTER 4. SURFACE TEXTURING

Detachment waves may change due to the presence of asperities on elastomeric surfaces, which changes the shear stiffness of the surface. After knowing the detachment waves are related to the shear accumulation, adding artificial asperities to belt surface by texturing may help change the shear accumulation and reduce the detachment waves. Compared to a textured belt, a textured pulley is harder to fabricate and less effective in that the belt may be squeezed into the gaps between patterns. In this chapter, we explore the possibility of minimizing self-oscillations associated with detachment waves via texturing of the belt contact surface. In so doing, we answer the question of whether regular surface patterns known to reduce detachment waves in sliding [89, 103] can be also employed in rolling, and we compare their performance to that of irregular surface textures. Even though the belt drive is under low-speed operation in this study, the conclusion is assumed to be valid for rolling at high speeds since the mechanism for minimizing contact instabilities via texturing is agnostic to speed.

4.1 Method and Means

4.1.1 Apparatus and Operating Conditions

A custom-built tribometer used in this study is described in Chapter 2. Similar to our previous studies, the driving speed was set to 3 mm s^{-1} and the tension at the tight and slack sides of the belt was adjusted to 6 N and 2 N, respectively. The travel distance of the driving stage was 300 mm. The temperature and relative humidity in the laboratory during the tests were 23°C and 35%, respectively. All statistical tests were performed using one-

way ANOVA (all pairwise multiple comparison procedures (Holm–Sidak method), overall significance level 0.05) in the ORIGIN software package (OriginLab Corporation, Northampton, MA).

4.1.2 Belt Specimen Preparation

The belt specimens were made out of a transparent polydimethylsiloxane (PDMS, Sylgard 184, Dow Corning, Midland, MI) elastomer at a 10:1 mixture ratio of Sylgard 184 pre-polymer and its cross-linker. The mixture was cured in light vacuum (to ensure no air bubbles trapped inside the belt) for 14 h at 65 ^{o}C in negative molding templates prepared using a four-step molding technique (Fig. 4-1) [104] to replicate the topography of either regularly or irregularly textured surfaces (Fig. 4-2). Use of three additional materials (PU, PVS and Epoxy, see Fig. 4-1) was required to ensure clean demolding since none of these materials can be easily separated from both the replicated surfaces and PDMS. The textured belts were 400 mm in length, 3 mm in thickness, and 10 mm in width, while the reference flat belt was 7 mm wide to ensure similar apparent contact areas.

Figure 4-1. Schematic of transferring texture from an original surface onto a PDMS belt.

The replicated surfaces with regular topography (Fig. 4-2a-d) were 3D-printed out of Formlabs Clear Resin (Formlabs, Somerville, MA) to have hexagonal and square projections with height h, size D, and lattice constant a. These projections were polished with SiC 2000 grit abrasive paper (Struers, Cleveland, OH) to different heights and a

surface roughness R_a of less than 150 nm. Based on our previous studies on the size effects of regular topography [81, 89], all patterned surfaces shared the same area density, AD = $(D/a)^2 \approx 70\%$ (chosen to have good grip, while still being able to fabricate gaps between smallest texture elements), while the examined parameters were the lattice constant, a = 0.6, 1, 3 mm, the aspect ratio, AR = h/D = 0.1, 0.2, 0.3, 0.4, 0.5, and the pattern shape and orientation (Fig. 4-2a-d).

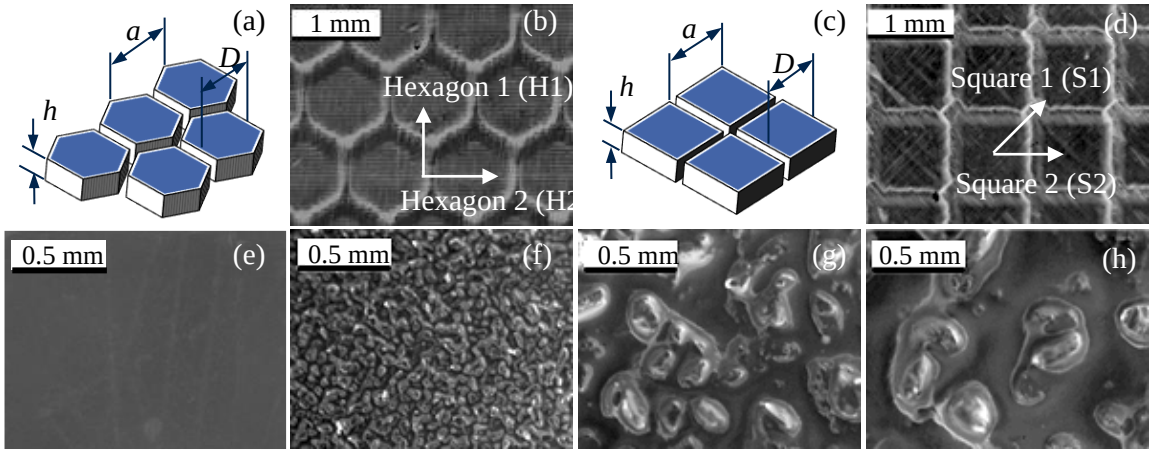

Figure 4-2. Schematic and optical microscopy images of replicated surfaces with regular and irregular topography. (a)-(d) 3D-printed hexagonal and square patterns. Arrows in the direction of rolling. (e) 3D-printed and polished surface. (f)-(h) 1200, 150 and 80 grit abrasive paper sheets, respectively.

The replicated surfaces with irregular topography (Fig. 4-2f-h) were SiC abrasive paper sheets of 2000, 1200, 800, 400, 200, 150, and 80 grit (Struers, Cleveland, OH; Lot Fancy Inc, San Francisco, CA). The surface profiles of abrasive papers were characterized using a Hommel Etamic W5 profiler (Jenoptik AG, Jena, Germany).

4.2 Regular Topography

The raw measurements of the difference in the belt tension and the pulley angular velocity obtained for the flat (reference) and hexagonally patterned belts in the driver case are plotted in Fig. 4-3 along with the characteristic images of the contact area. The effect of regular surface texture is obvious. With the reference flat belt, the self-oscillation of the pulley, which is generated due to contact instabilities and induces large-scale fluctuations in the belt tension difference (Fig. 4-3a), is so powerful that the pulley periodically halts, as follows from inspection of the angular velocity signal. When the patterned belt is used, the pulley rotates much more steadily, and only subtle fluctuations are observed around the prescribed angular velocity (~0.3 rad s^{-1}), which reflects also on the fluctuations in the belt tension (Fig. 4-3b). Looking at the evolution of the contact area, which visualizes the source of system instabilities, we can also clearly see the difference in the behavior of the flat and patterned belts. First, the size of the detachment zone is greatly reduced (from ~7 mm to ~0.5 mm) when a regular surface pattern is introduced. Second, the characteristic surface folds representing waves of detachment (isolated air-pockets within the contact area, such as the one seen on image 3 in Fig. 4-3a) are barely distinguishable for the patterned belt.

Detachment waves in the driver pulley case appear due to a shear-induced moment generated at the belt exit region. When the belt surface is split into multiple disconnected and independent sub-contacts via patterning, its stiffness is reduced such that a much smaller moment is needed to start detachment. To this end, since the shear-induced moment grows until it is relaxed by detachment, the detachment waves also have a smaller scale and are formed more often, leading to less violent excitation of the system. In light of this

rationalization, we may expect to be able to minimize the self-oscillation of the belt drive system by modifying the geometrical characteristics of the independent contact elements.

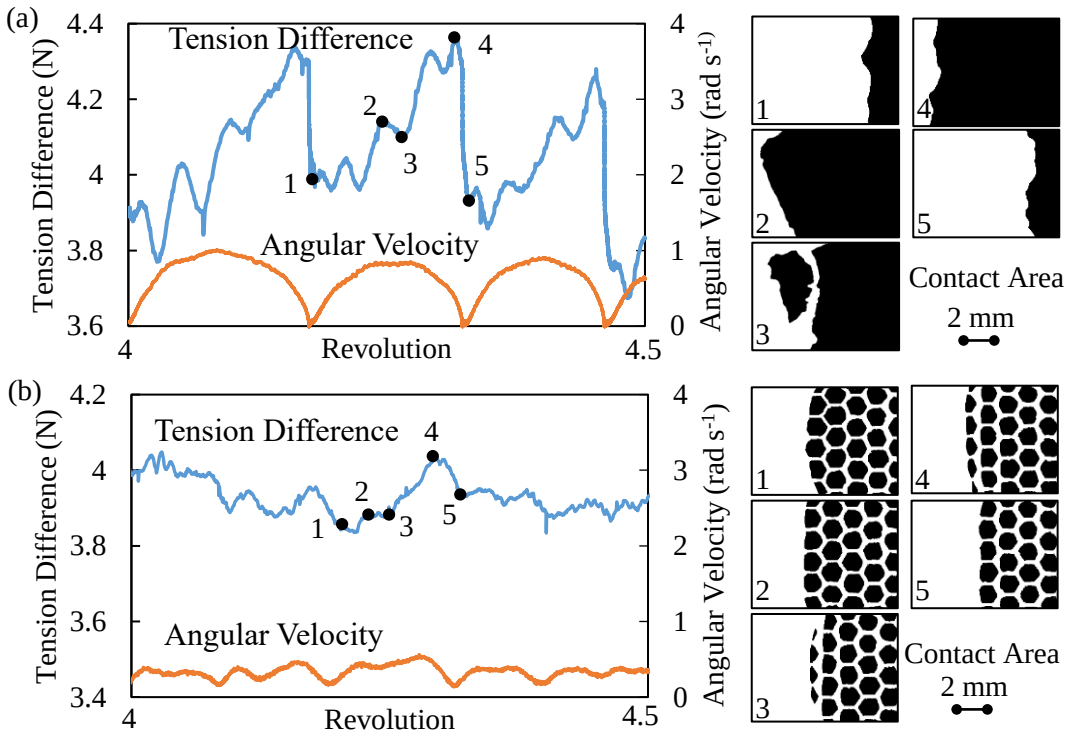

Figure 4-3. Tension difference and angular velocity measured on (a) reference flat belt and (b) hexagonally patterned (a = 1 mm, AR = 0.2) belt, and characteristic sequences of images representing evolution of the contact area (shown in black) in the driver case.

4.2.1 Effects of Shape and Orientation

Hexagon- and square-shaped patterns orientated differently with respect to the rolling direction (H1, H2, S1 and S2, as shown in Fig. 4-2) were tested and compared with the reference flat belt in terms of the frequency and amplitude of the belt and pulley oscillations (Fig. 4-3). The oscillations in the belt tension difference (as shown in Fig. 4-3)

were decomposed into small-scale and large-scale components associated with pulley motion and detachment events, respectively. Given that the characteristics of the pulley motion-related oscillations in the belt tension difference resemble those of the oscillations in the pulley angular velocity shown also in Fig. 4-3, only the detachment event-related oscillations in the belt tension difference are presented. The second order oscillations in the pulley angular velocity that correspond to detachment events are also not shown as they are similar to those in the tension difference signal.

Figure 4-4 demonstrates similar oscillation characteristics for all patterned belts regardless of the pattern shape and orientation in both the driver and driven cases, and no statistically significant difference between these patterns is observed either. This observation supports our hypothesis regarding the core mechanism of the disruption of detachment waves — the reduction of surface stiffness is independent of the pattern type (to a first approximation), so the belt can detach from the pulley more easily as long as its surface is split, while the shape and orientation of the contact patches are not important. This finding allows us to use just one representative shape, and the pattern H1 is chosen for the following study.

The effect of patterning, however, is different for the driver and driven cases. For the driver pulley, the amplitude of both types of oscillation is reduced by a factor of approximately 3, and the frequency is increased by a factor of approximately 1.5, while for the driven pulley, the observed effect is much weaker. This is explained by the difference in the mechanism of detachment. In the former case, the detachment is shear-driven, and surface conditions are vital, while in the latter case, it is stretch-driven, and the surface conditions are less decisive, as volume effects dominate. Another important observation is

that the oscillations in the driver case become even less pronounced than those in the driven case when the belt surface is textured.

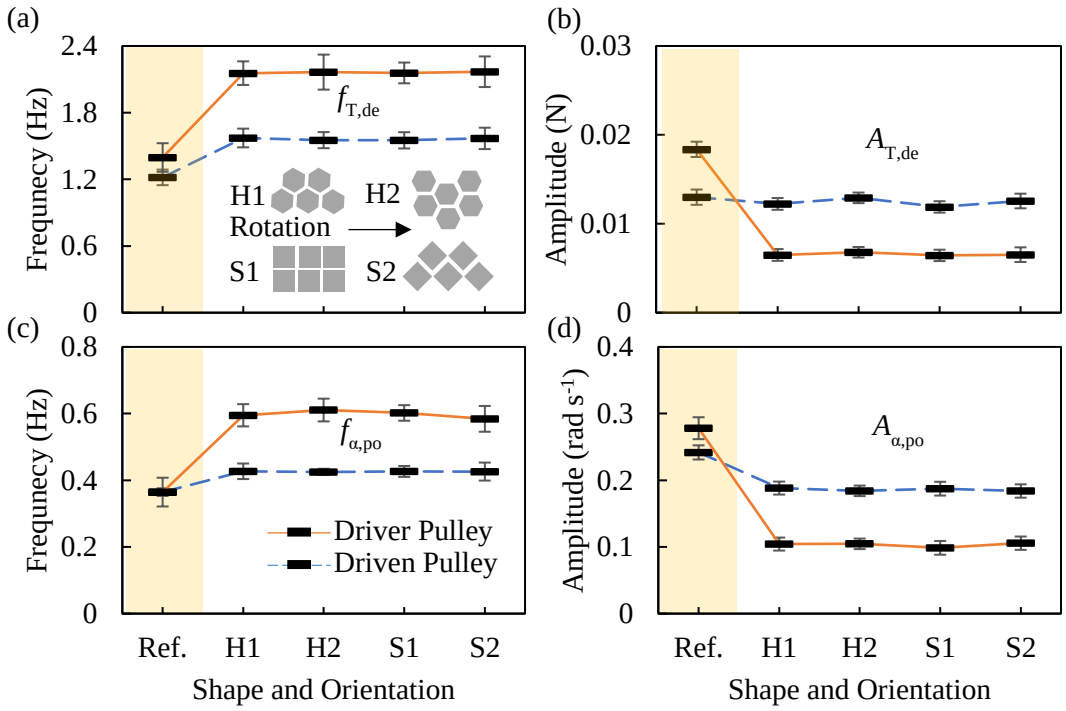

Figure 4-4. The effect of the pattern shape and orientation on frequency, *f*, and amplitude, *A*, of the fluctuations in the tension difference, *T*, (a), (b), respectively, and in the angular pulley velocity, *α*, (c), (d), respectively, in both the driver and driven cases. The fluctuations in the tension difference presented here correspond to detachment events only. All patterns share the same lattice constant and aspect ratio (*a* = 1 mm, *AR* = 0.2). The error bars show standard deviations.

4.2.2 Effect of Lattice Constant

Decreasing the lattice constant (i.e., increasing the number of individual sub-contacts per unit area) does show a small measurable effect, though no statistically significant difference is observed between different lattice constants in both the driver and

driven cases (Fig. 4-5). This agrees with observations made in other studies where the most significant effect is achieved during initial contact splitting, while further minimization of vibrations requires increasing the number of individual sub-contacts by several orders of magnitude [89], which may be considered impractical. Given that we were limited by the resolution of 3D printing in preparing the molding templates, our finest pattern was based on the lattice constant of 0.6 mm, which results in just 25 times more individual sub-contacts than in the case of our coarsest pattern with the lattice constant of 3 mm. Evidently, this change is not strong enough.

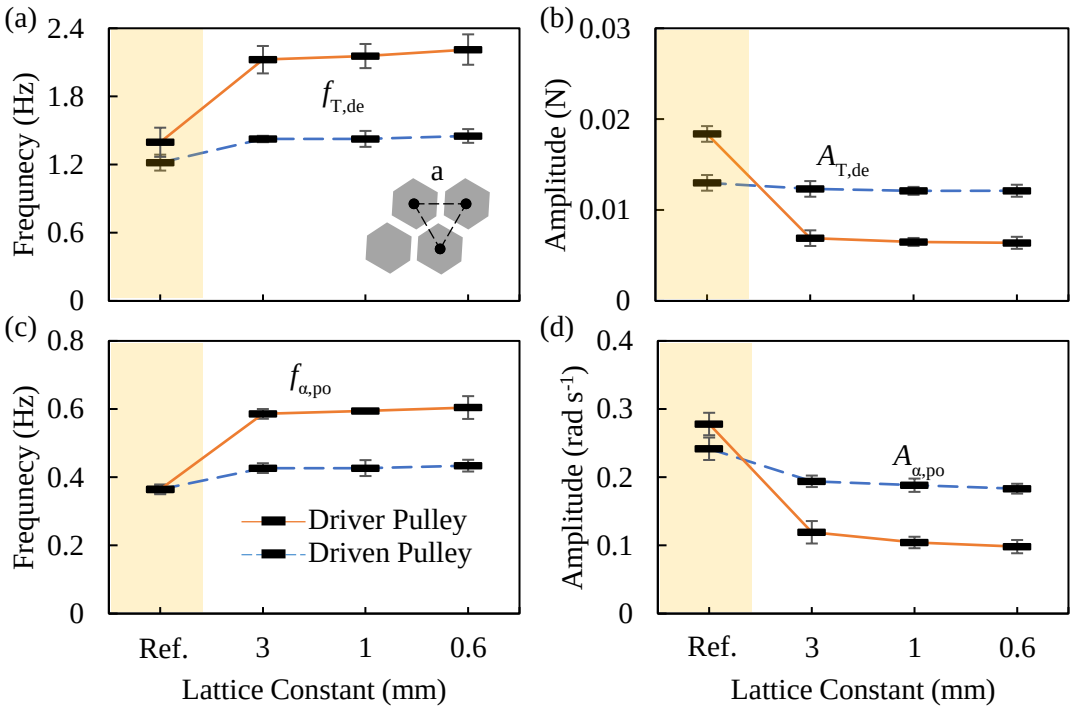

Figure 4-5. The effect of lattice constant on frequency, *f*, and amplitude, *A*, of the fluctuations in the tension difference, *T*, (a), (b), respectively, and in the angular pulley velocity, *α*, (c), (d), respectively, in both the driver and driven cases. The fluctuations in the tension difference presented here correspond to detachment events only. All patterns share the same aspect ratio (*AR* = 0.2). The error bars show standard deviations.

4.2.3 Effect of Aspect Ratio

The aspect ratio of the hexagonally shaped projections is next varied from 0.1 to 0.5. Increasing the aspect ratio from 0.1 to 0.4 led to an increase in frequency and to a decrease in amplitude of the oscillations in both the belt tension difference and the pulley angular velocity, as shown in Fig. 4-6. However, a statistically significant effect of aspect ratio was observed only in the driver pulley case, which results from the difference in the mechanisms of detachment in the driver and driven cases as discussed above. Interestingly, the belt patterned to have an aspect ratio of 0.5 was incapable of carrying the prescribed torque in either the driver or the driven pulley. These observations are explained in the following way.

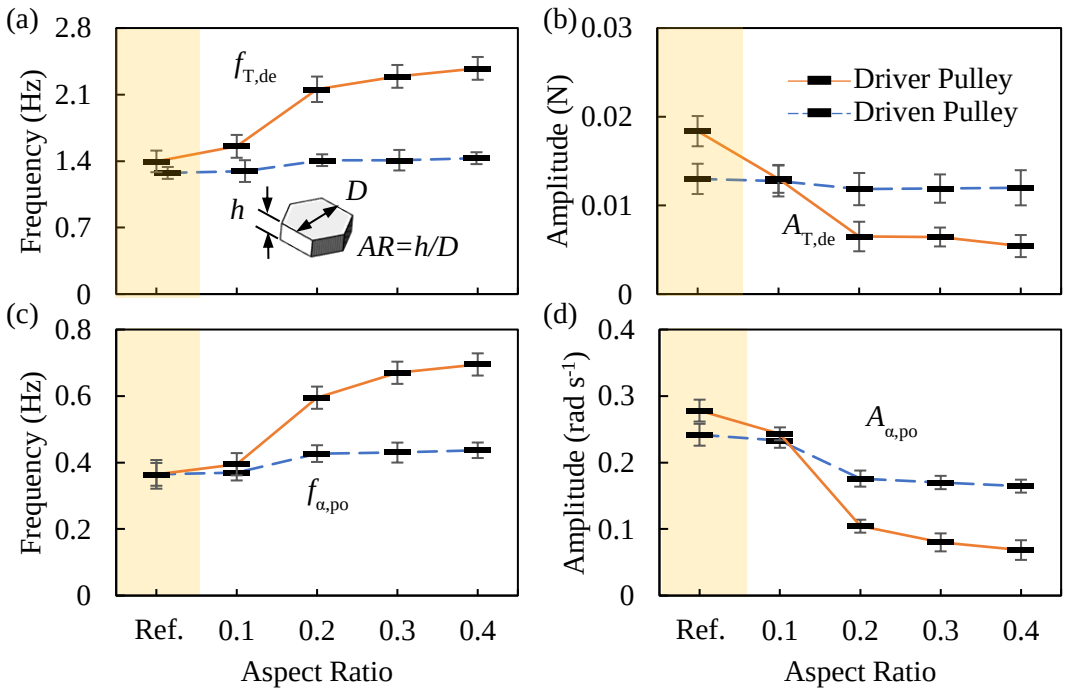

Figure 4-6. The effect of aspect ratio on frequency, *f*, and amplitude, *A*, of the fluctuations in the tension difference, *T*, (a), (b), respectively, and in the angular pulley velocity, *α*, (c), (d), respectively, in both the driver and driven cases. The

fluctuations in the tension difference presented here correspond to detachment events only. All patterns share the same lattice constant (a = 1 mm). The error bars show standard deviations.

As the aspect ratio increases, the bending stiffness of the hexagonal projections is reduced. As a result, these projections bend more easily under shear traction. Correspondingly, since the threshold for the formation of detachment waves is easier to reach, the detachment events initiated by the shear-induced moment in the driver case occur more frequently and have smaller range. However, with large enough aspect ratio, the projections bend to such a degree that their flat ends lose contact with the pulley [81] regardless of the shear direction. This leads to a great reduction in the real contact area and in the ability to resist shear. The so-called "slip" zone then grows until it consumes the entire belt-pulley interface in both the driver (Fig. 4-7) and the driven cases. At this moment, a global displacement between the pulley and the belt is established, and no further power can be transmitted. The resolution of our imaging system does not enable us to say whether bent hexagonal projections truly slide, or small-scale detachment waves allow for relative motion in the slip zone, but in any event they can move independently, and the scale of global belt drive oscillations is reduced due to scattering of local "slip" events over time and space [89].

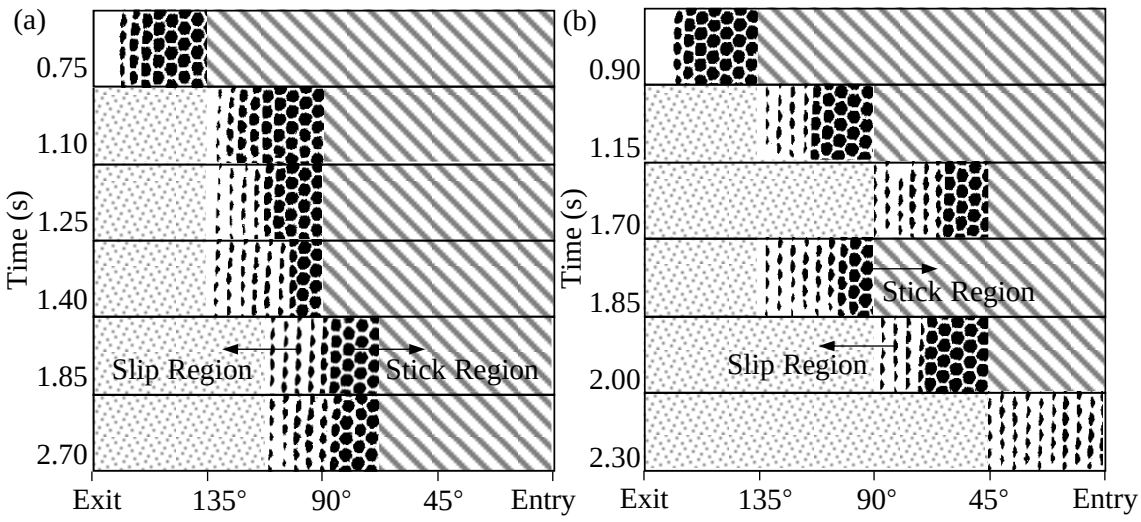

Figure 4-7. Evolution of the patterned contact area (shown in black) obtained in the driver case with a camera installed at different angular orientations. (a) *AR* = 0.4, torque is transmitted. (b) *AR* = 0.5, torque is not transmitted. Hatched areas represent the regions out of view.

4.3 Irregular Topography

Given that the aspect ratio of regular topography was found to be the dominant parameter affecting the belt drive oscillations, to study the effect of irregular surface topography, we have constructed a similar ratio of vertical and horizontal profile characteristics, R_a/S_m, where R_a and S_m are the standard roughness average and the mean spacing of profile irregularities, respectively. In this way, the effects of regular and irregular surface topography on the oscillation characteristics of textured belts can be plotted in one figure. Notably, similar to the regularly textured belts, the belts with irregular surface topography could not transmit the prescribed torque when the roughness ratio was too high ($R_a/S_m \approx 0.041$, for the belt cast against the roughest abrasive sheet of 80 grit). This allowed us to scale the horizontal axes of Aspect Ratio and R_a/S_m such that the data could be conveniently compared as shown in Fig. 4-9 – i.e., the far right-end of the R_a/S_m (bottom

horizontal axis; irregular textures) and Aspect Ratio (top horizontal axis; regular textures) domains both correspond to gross slip.

Studying the self-oscillation behavior of the irregularly textured belts, we see that it resembles that of the belts with regular topography, while the observed effects are generally weaker (Fig. 4-8). Most likely, this is because surface irregularities on rough belts have smaller contact area and less bending compliance than surface projections on regularly patterned belts, making the effect of texturing less pronounced. Further, while maintaining statistically indistinguishable values in the driven case, in the driver case the frequencies and amplitudes of the oscillations related to both the detachment events and the angular velocity signal change significantly as R_a/S_m increases up to 0.02 and then remain constant for larger values of R_a/S_m. This can possibly be related to the irregularly patterned belt surfaces having random shapes, sizes and distribution of asperities, so other characteristics can change simultaneously with the aspect ratio of surface asperities and lead to deviation from the expected effect of the aspect ratio alone.

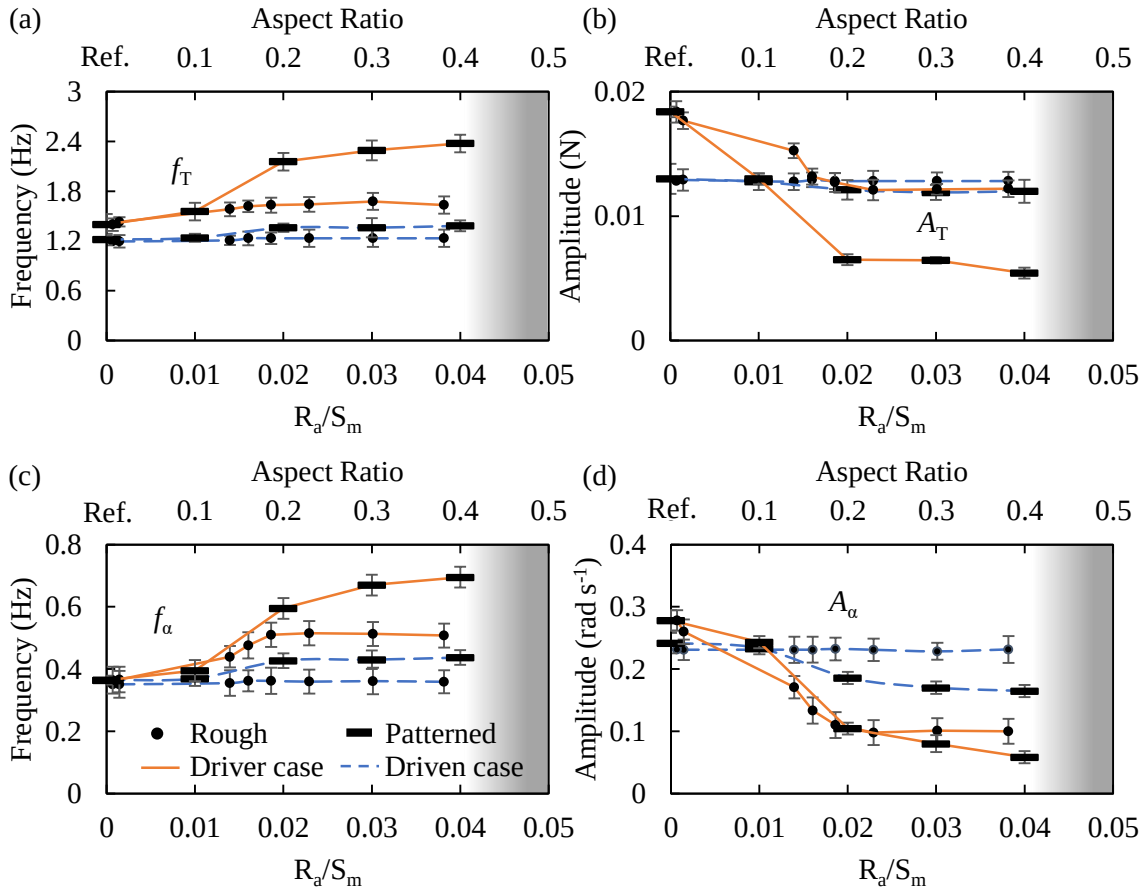

Figure 4-8. Comparison of the effects of surface roughness (irregular topography) and aspect ratio (regular topography) on frequency, *f*, and amplitude, *A*, of the fluctuations in the tension difference, *T*, (a), (b), respectively, and in the angular pulley velocity, *α*, (c), (d), respectively, in both the driver and driven cases. The fluctuations in the tension difference presented here correspond to detachment events only. The error bars show standard deviations.

In general, the similarity between the effects of regular and irregular surface texturing validates our hypothesis that splitting the contact area into disconnected sub-contacts helps minimizing detachment wave-induced oscillations in rolling. The regular surface texturing, however, has an advantage over the irregular surface texturing since the system's self-oscillations can be minimized to a greater extent, and both the driver and the driven rolling can be improved.

4.4 Concluding Remarks

The results obtained in this work allow us to draw the following conclusions:

1. Surface texturing can be successfully employed for minimizing local contact instabilities and global self-oscillations in belt drive systems, and the effect is much more pronounced in the driver case than in the driven case due to different mechanisms for formation of detachment waves.

2. Both regular and irregular surface topographies are useful in minimizing the belt drive vibrations, but regular surface textures provide a stronger effect.

3. The aspect ratio of surface projections is found to be the most important parameter, and the lattice constant is found to be marginally effective, while the pattern shape and orientation show no effect at all on the belt drive performance.

4. Too excessive texturing of the belt surface can cause the belt to lose its tractive capabilities.

CHAPTER 5. TENSILE CORDS

In this chapter, we present an experimental and theoretical study on the effects of belt cord inclusion on contact instabilities and frictional mechanics in a simple belt-drive system. The detachment waves are first examined, and the related system oscillations are studied and compared with those for the regular flat belt, a patterned belt and a patterned belt with tensile cords. The shear traction at the belt-pulley interface is then measured and compared with the Firbank shear model[13]. Lastly, frictional losses in the system for the belt with tensile cords are estimated via combination of experimental observations and a theoretical model.

5.1 Method and Means

5.1.1 Apparatus and Operating Conditions

The setup employed herein was configured with either speed control of the exiting span of the belt (Fig. 5-1a) or of the pulley (Fig. 5-1b). The former configuration enables study of pulley rotational oscillations excited by detachment events at the belt-pulley interface (the one used in Chapters 2 and 4); the latter configuration eliminates pulley oscillations, clarifying study of detachment waves (the one used in Chapter 3). Notably, in Fig. 5-1a, reversing the direction of the torque allows us to switch between the driver (solid lines) and driven cases (dashed line), and in Fig. 5-1b, the switch between the two cases can be achieved via adjusting the two tension weights.

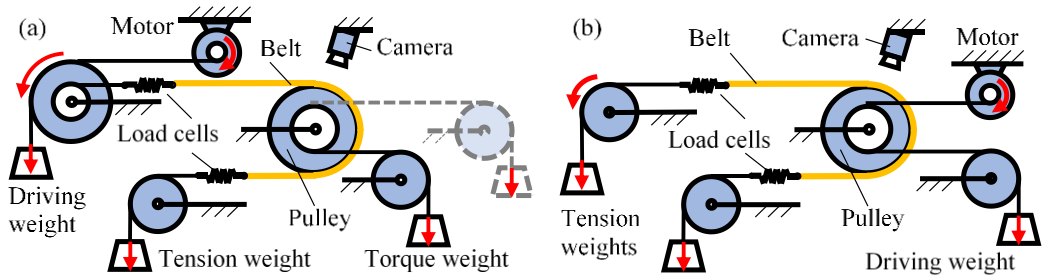

Figure 5-1. Schematics of the experimental apparatus with constant speed applied to (a) the exiting side of the belt and (b) the pulley.

Limited by the strength of the belt without cords (also referred as the reference belt herein), we choose to work with a maximum allowable belt tension of 6 N. The tension difference between the two spans of the belts is adjusted to 4 N. The driving speed and the travel distance of the belt are 3 mm s^{-1} and 300 mm (~5 revolutions of the pulley), respectively. Each test is repeated at least 10 times. The temperature and relative humidity in the laboratory were 20 °C and 10 %, respectively.

5.1.2 Belt Specimen Preparation

We fabricated the belt specimens using PDMS and also molded evenly distributed tick marks with ~0.125 mm intervals to the belt sidewall for the shear measurement (details can be found in Section 3.1.2). Finally, we cut a reference flat belt specimen of 400 mm in length, 8 mm in width and 3 mm in thickness from the molded form.

We fabricated flat belts with tension members by following the same process except that four cotton cords were placed on the template with 3 mm intervals under 0.1 N pre-tension before molding. The cured belts with tensile cords were then cut as designed in Fig. 2 with 400 mm in length. Additionally, a patterned belt with tensile cords (right one in Fig. 5-2c) was produced via a four-step molding technique replicating the topography of

regularly textured example surfaces (details can be found in Section 4.1.2). The patterned surface has an area density of AD = $(D/a)^2 \approx 70\%$ where a = 1 mm denotes the lattice constant and D denotes the diameter of the inscribed circle, and the aspect ratio, AR = h/D = 0.2 where h denotes the height of the projections (Fig. 5-2b). The four cotton cords are placed 2.75 mm above the patterned mold before the last molding.

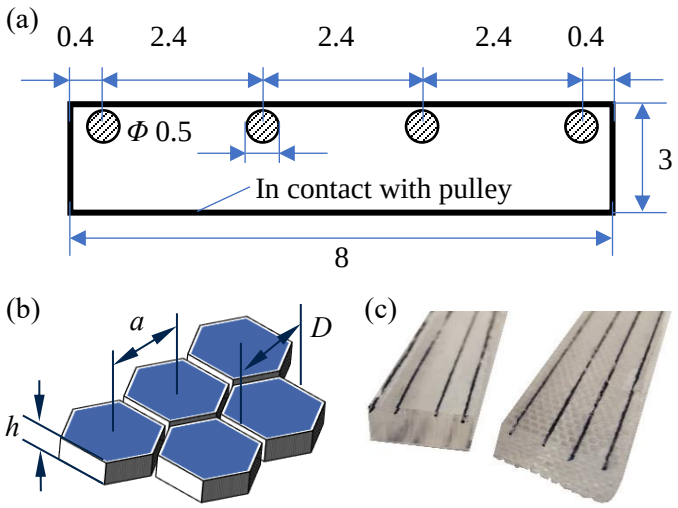

Figure 5-2. Design of the belt with tensile cords with the (a) cross-section drawing (unit: mm) and (b) schematic of the patterns for patterned belts with tension cords, and (c) picture of the as-molded belts.

5.2 Contact Instabilities and Self-Oscillations

Figure 5-3 plots the time-history of the tension difference between the two spans of the belt, and the pulley angular velocity, both measured using a corded belt for the driver and driven cases. The figure also provides images capturing time-evolution of the contact area. Similar to previous studies using reference flat belts in Chapters 2 and 3, the relative displacement between the corded belt and the pulley is achieved by means of cyclic detachment in both the driver and driven cases. As in Section 2.2.1, we observe more

pronounced detachment events in the driver case than in the driven case. They are manifested by isolated folds such as the one shown in image 3 of Fig. 5-3a, where the black region denotes contact area; such folds are missing in the driven case. Formation of these folds confirms the persistence of detachment waves also in belts with a composite cross-section, and adds to the evidence that such events are a ubiquitous feature of tension transition in belt-drives operating at low speed.

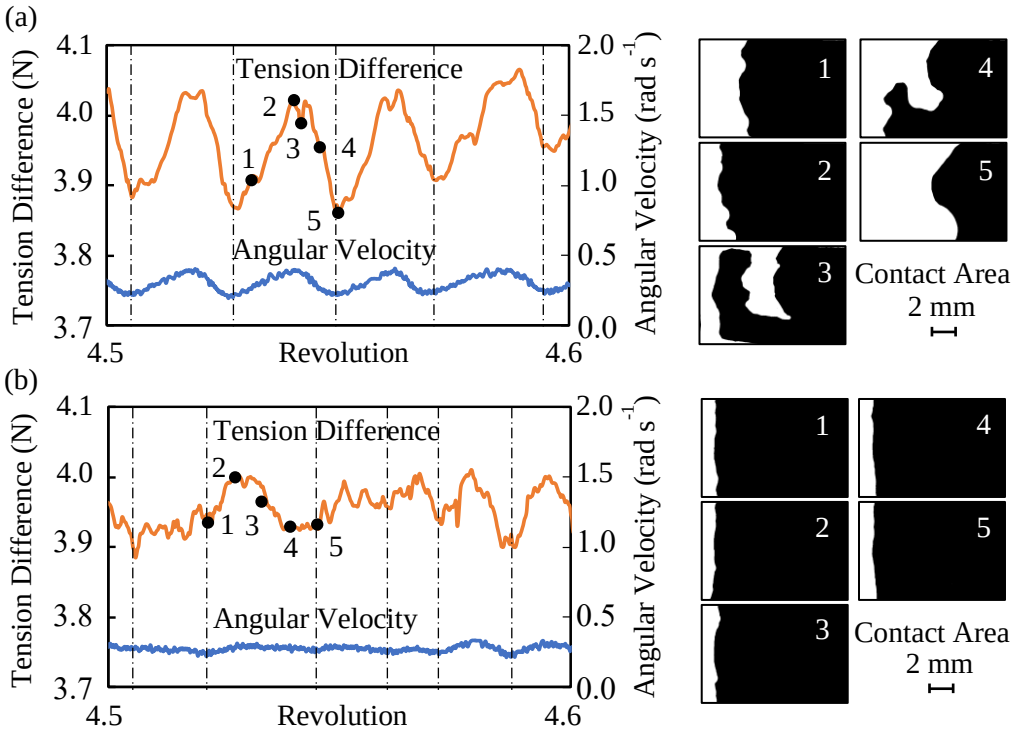

Figure 5-3. Tension difference and angular velocity measured using a belt with tensile cords, and characteristic sequences of images representing time-evolution of the contact area (shown in black) in (a) the driver case and (b) the driven case.

In order to characterize the effect tensile cords have on the character of the observed detachment events, the same tests as those described above have been conducted on a regular flat belt (Ref), a hexagonally patterned belt (Pattern), a regular belt with tensile cords (Cord), and a hexagonally patterned belt with tensile cords (Pattern-Cord). The

effects are documented in Fig. 5-4 based on the frequency and amplitude of oscillations in the tension difference and pulley angular velocity. Although the tension difference fluctuations are affected by both the contact instabilities and the pulley oscillations, as shown in Fig. 5-3, we can extract frequency and amplitude information of only detachment events (Fig. 5-4a,b) using a wavelet decomposition. For the pulley rotational oscillations, we simply apply a Fast Fourier Transformation (FFT) to the angular velocity signal to obtain the corresponding frequencies and amplitudes (Fig. 5-4c,d).

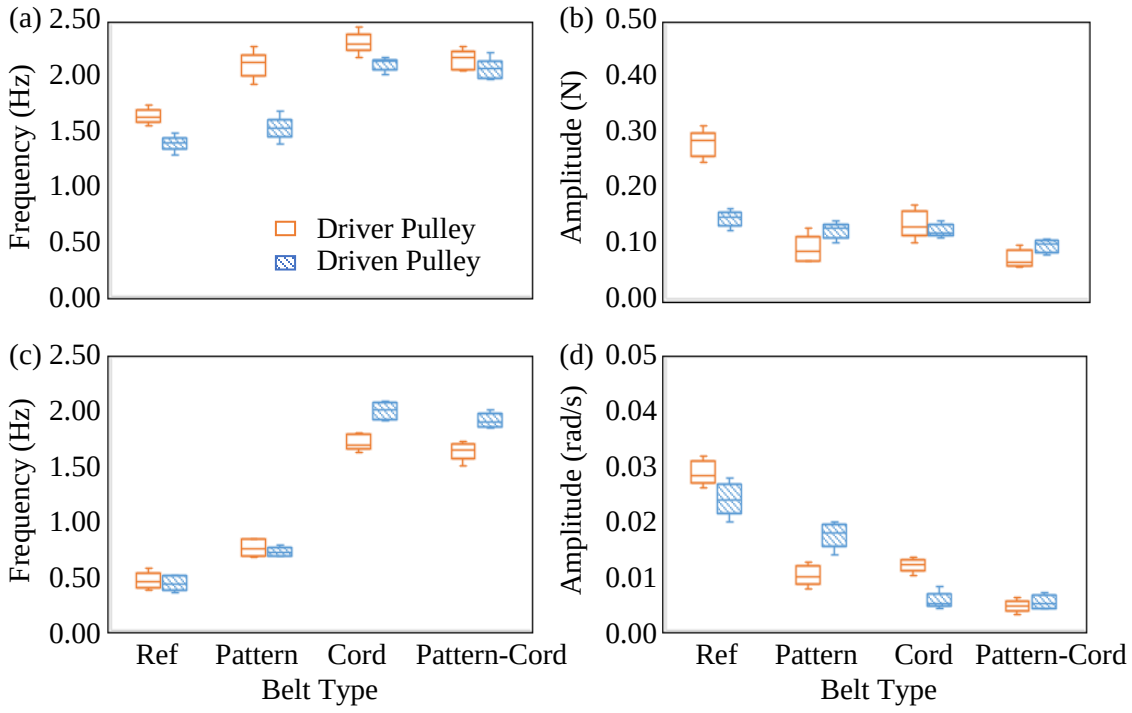

Figure 5-4. Frequency and amplitude of fluctuations in (a)-(b) tension difference and (c)-(d) angular velocity as a function of belt type for both the driver and driven cases. The fluctuations in the tension difference presented here correspond to detachment events only.

When comparing the belt with tension cords (Fig. 5-3) and the reference belt, we find that the presence of the belt cords results in steadier pulley rotations with only subtle fluctuations around the prescribed angular velocity. The rotational oscillations in both the

driver and driven cases have higher frequencies (Fig. 5-4c), but smaller amplitudes (Fig. 5-4d). These trends can be expected due to the significant increase in the belt stiffness provided by cords, which should act to increase oscillation frequencies and decrease deformations. In addition, the belt contact instabilities affect pulley rotation leading to a self-oscillation, as discussed in Section 2.2; i.e., the local contact instabilities serve as an excitation source for the pulley rotational response, which, in turn, stores a periodic tension pattern in the belt, further destabilizing the pulley rotation. The detachment waves, which cause the self-oscillation of the pulley, take place more frequently in a corded belt as compared to a regular flat belt (Fig. 5-4a). On the other hand, the corded belt, limited by the tension cords, can detach from the pulley to a smaller extent compared to a regular flat belt, leading to a decrease in the corresponding amplitude (Fig. 5-4b). This effect is not pronounced in the driven case since the detachment events happen mainly due to peeling, which is weakly affected by the presence of tension cords.

When we pattern the contact surface of the belt with tension cords, we expect to see additional benefits associated with disruption of the contact surface, as reported in Chapter 4. An important question then arises: does the combination of surface patterning and inclusion of tension cords eliminate contact and rotational instabilities? As documented in Fig. 5-4, the detachment events and pulley oscillations persist on a corded belt with patterns, confirming again their ubiquitous nature. However, the amplitudes of the contact and rotational instabilities (Figs. 5-4b and 5-4d) are minimized by the combination, while a small decrease in frequency for both can be noted (Figs. 5-4a and 5-4c).

5.3 Belt Drive Mechanics

5.3.1 Shear Traction

The presence of tensile cords in the belt results in a significant difference in the belt-drive mechanics, especially for the shear traction along the belt-pulley interface. Shear traction develops and accumulates in the belt from the start of the contact arc due to the speed gradient between the tension member and belt-pulley interface, as described first by Firbank [13]. Herein, we evaluate the shear strain along with the contact status of the belt as a function of position for the corded belt. The shear strain is obtained by quantifying the deformation using visual observation of the tick marks. The contact status is determined by the light interference at the belt/pulley interface. Unlike Chapter 3, the measurement of the longitudinal stretching strain is not feasible since the stretching strain is significantly smaller due to the larger stiffness of the composite belt.

In the driver case, the distribution of shear strain is correlated with the contact area at the instance when a fold (non-contact region in white separating two contact regions) is formed at the exit zone (Fig. 5-5a). The shear traction is defined as positive when the pulley drives the belt (the driver pulley). Along the direction of belt motion, as shown in the small schematic in Fig. 5-5b, the shear strain at the belt-pulley interface develops gradually from 180° (entry) to 62°, and then grows dramatically up to its peak from 62° to 37°, and then finally drops down to zero within 10°. Compared with a regular flat belt, the gradual growth of shear (180° to 62°) is unique to the corded belt, which, we believe, is due to the speed gradient in the belt. It is notable that the position of the maximum shear strain coincides

with the right edge of the fold; hence, the fold and the region to its left is a relaxation zone, carrying no traction regardless of whether this region is in contact or not.

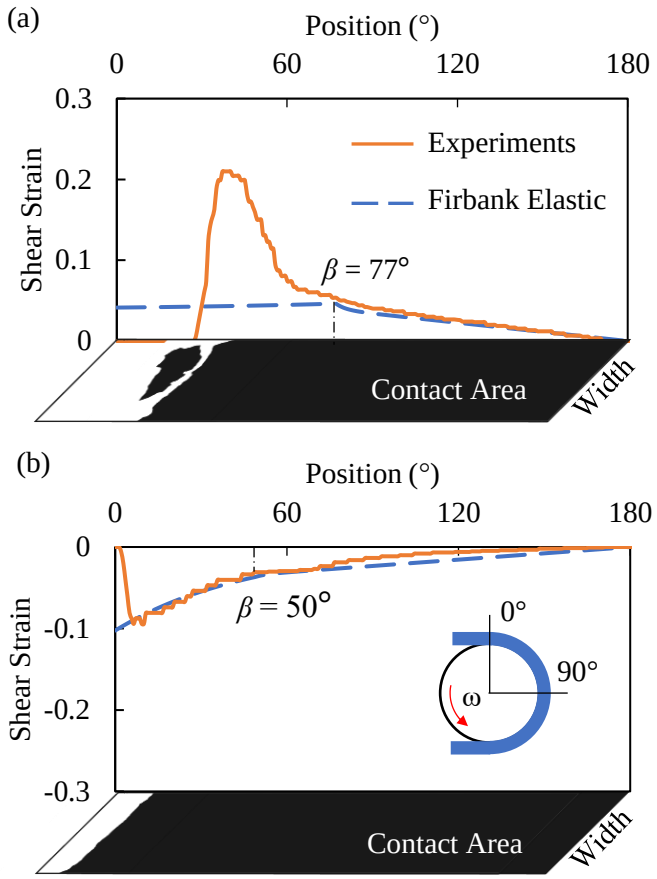

Figure 5-5. Comparison between the measurement of the shear strain at the corded belt–pulley interface (black area denotes contact) and the prediction by the Firbank model for both the (a) driver and (b) driven pulleys.

In the driven case, the belt transmits tension smoother than in the driver case, with no detachment waves at the belt-pulley interface. The contact area in the driven case is larger than that in the driver case, but the magnitude of the shear strain in the driven case is smaller than that in the driver case. The shear strain in the driven case is negative,

indicating that the belt drives the pulley. The shear strain develops gradually due to the speed gradient in the belt from entry until relaxation at around 10°.

Our experimental results for shear strain distribution are next compared with predictions by the Firbank model, which was proposed for belts with tension members. According to the Firbank model [13], the shear strain γ in the adhesion arc as a function of the angle θ measured from the entry point obeys

$$\gamma(\theta) = kR\theta + \frac{1}{t}\int_0^{\theta} \frac{\Delta F_T(\theta)}{E_t A_t} R d\theta \tag{5.1}$$

The first term in the expression represents the shear strain due to the speed differential between the pulley envelope and tension members. R denotes the pulley radius, and k the speed differential factor, $k = \frac{V_{cord} - V}{V}$. Here, $V_{cord} = (R + t) \cdot \omega_{pulley}$ is the cord speed at the entry point and $V = R \cdot \omega_{pulley}$, where ω_{pulley} denotes the angular velocity of the pulley. The second term represents the shear strain due to the contraction/extension of the belt, with $\Delta F_T(\theta)$ denoting the tension drop/rise along arc θ, which can be estimated by the tension distribution formula developed by Firbank [105] (driver pulley, Eq. 5.2a; driven pulley, Eq. 5.2b),

$$\frac{F_T(\theta)}{F_{TS}} = e^{\mu_k \beta}\left\{1 + \frac{\mu_s}{\lambda}\left[\frac{\cosh\lambda(\pi - \beta) - \cosh\lambda\theta}{\sinh\lambda(\pi - \beta)}\right]\right\}, 0 \le \theta \le \pi - \beta, \tag{5.2a}$$

$$\frac{F_T(\theta)}{F_{TS}} = e^{\mu_k(\pi - \theta)}, \pi - \beta \le \theta \le \pi.$$

$$\frac{F_T(\theta)}{F_{TS}} = 1 + \frac{\mu_s(\cosh\lambda\theta - 1)}{\lambda\sinh\lambda(\pi-\beta) - \mu_s(\cosh\lambda(\pi-\beta)-1)}, 0 \le \theta \le \pi - \beta, \quad (5.2b)$$

$$\frac{F_T(\theta)}{F_{TS}} = \frac{F_T(\pi-\beta)}{F_{TS}} e^{\mu_k(\theta-\pi+\beta)}, \pi - \beta \le \theta \le \pi.$$

where μ_s and μ_k are static and kinetic friction coefficients (both are set to be 1.3 for our system based on Ref. [106]), and $\lambda = \sqrt{\frac{GBR^2}{tE_tA_t}}$ is a parameter related to the geometry and material properties of the belt (provided in Section 5.3.2 and Table 5-1). Here, the slip arc angle, β, can be computed iteratively: β is varied until the ratio between the tension in the slack and tight spans of the belt, F_{TS} and F_{TT}, respectively, from Eq. 5.2 matches the ratio as prescribed during the experiment. Then, the shear strain distribution in the adhesion arc can be estimated using Eq. 5.1. The shear strain in the slip arc is obtained by computing the sliding friction per unit area via Coulomb's friction law (by multiplying the normal force per unit area, $\frac{F_T(\theta)}{RB}$, by the kinetic friction coefficient μ_k) and then converting the shear stress to shear strain using the shear modulus G (driver pulley, Eq. 5.3a; driven pulley, Eq. 5.3b),

$$\gamma(\theta) = \mu_k \frac{F_T(\theta)}{RB}\frac{1}{G} = \frac{\mu_k F_{TS}}{GRB} e^{\mu_k(\pi-\theta)}, \pi - \beta \le \theta \le \pi. \quad (5.3a)$$

$$\gamma(\theta) = \mu_k \frac{F_T(\theta)}{RB}\frac{1}{G} = \frac{\mu_k F_T(\pi-\beta)}{GBR^2} e^{\mu_k(\theta-\pi+\beta)}, \pi - \beta \le \theta \le \pi. \quad (5.3b)$$

Note that Eqs. 5.1 and 5.3 determine the shear strain from the entry point to exit point, which requires a change of the angular coordinate, $\theta \rightarrow \pi - \theta$, to compare directly with the experimental results.

The predicted shear strain for both the driver and the driven cases obtained using the Firbank model is plotted by dashed blue lines in Fig. 5-5. The most obvious difference between the experimental and theoretical results lies in the exit region. In the experiment, there is a significant accumulation of the shear traction followed by a rapid relaxation via detachment waves. The Firbank model fails to predict this relaxation. Instead, the exit region in the Firbank model is governed by Coulomb's friction law when the shear traction reaches the maximum static friction. In addition, the shear traction at the exit point predicted by the Firbank model is non-zero, which violates compatibility since the shear strain must be zero in the spans immediately next to the exit region. Nevertheless, the Firbank model makes decent predictions of the shear distribution in the adhesion arc for both cases, although there is more apparent conflict with the experimentally-obtained results in the driver case. This deviation results from the Firbank model's inaccurate estimation in the relaxation region, which influences the shear distribution in the adhesion region.

5.3.2 Mechanical Losses

Following the measurement of shear traction at the belt-pulley interface, we can estimate the mechanical losses due to rolling friction for corded belts according to the approach outlined in Chapter 3. For the belt segment in contact with the pulley, the sum of all moments about the pulley axis is zero due to conservation of angular momentum. These

moments include ones due to tension forces (concentrated on tension cords to a first approximation), shear traction at the belt-pulley interface (integration of shear strain over the contact arc multiplied with the shear modulus), and shear and tension forces together with moments applied at the free belt spans. As measured and computed (see Table 5-1), the moment due to the tangential (shear) traction forces about the pulley axis equals to 57.5 N·mm in the driver case (representing the power source/input when the pulley drives the belt) and to -43.7 N·mm in the driven case (representing the load/useful output when the pulley is driven by the belt). The moment due to the difference in the tension forces are -49.5 N·mm (useful output) and 48.3 N·mm (input) for the driver and driven cases, respectively. Notably, the moment due to the difference in tension forces is larger than that of a regular flat belt under the same loading condition since the tension forces in the composite belt, concentrated at the tension member, possess larger moment arms about the pulley axis. Based on the moment equilibrium, the rolling friction moments are estimated to be -8.0 N·mm and -4.6 N·mm in the driver and driven cases, respectively. The rolling friction moment is much higher in the driver case due to the appearance of detachment waves.

The rolling friction for a corded belt is quite small for both the driver and the driven case (Fig. 5-6a) compared with the rolling friction for a reference belt. A further calculation based on our model predicting the rolling friction can explain this behavior quite well. In the model, the mechanical losses result from both the viscoelastic deformation of the belt material and the detachment events at the belt-pulley interface. The viscoelastic deformation is due to five different types of cyclic loadings, including bending, stretching, radial compression, shear, and stretching fluctuation. The energy dissipation due to

detachment events is the difference between the energy spent during detachment and the energy gained during attachment. Here, the detachment/attachment hysteresis is treated as the fracture/healing process between two layers for the calculation of the associated spent/gained energy [63, 101]. The details about this model are provided in Chapter 3. The parameters needed for the calculation can be found either in Table 5-1 or in [102, 107].

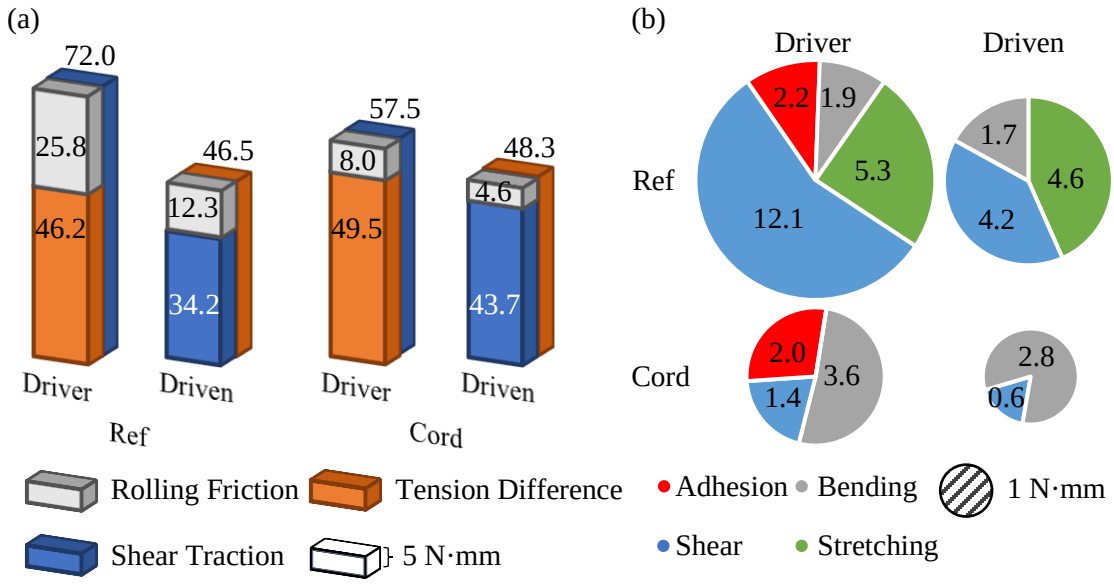

Figure 5-6. Moments applied to the belt wrapped over the driver and the driven pulleys. (a) Experimental data. (b) Model of rolling friction.

The rolling friction in the belt with tensile cords is mostly due to cyclic shear and bending, and for the driver case, there is an additional contribution from adhesion (Fig. 5-6b). Compared with the regular flat belt case (Ref), the contribution from cyclic stretching is absent and the rolling friction moment due to shear is much smaller. As a result, the rolling friction in the belt with tensile cords is much smaller. The contribution from shear is small here since the maximum shear strain and the frequency of the cyclic variation of shear deformation are both smaller than those in the reference belt.

Table 5-1. Model parameters.

Nomenclature		Value
Symbol	Parameter	(Driver/Driven)
F_{TS}	Tension at the slack span, N	2
F_{TT}	Tension at the tight span, N	6
G	Shear modulus of the belt, MPa	0.53
R	Radius of the pulley, mm	10
v	Poisson's ratio	0.499
B	Width of the belt, mm	8
t	Thickness of the belt, mm	3
V	Driving speed, mm s^{-1}	3
E_t	Elastic modulus of tension member, GPa	3.3
A_t	Tension member cross section area, mm^2	0.196
γ_{a_ex}	Max. shear strain at the exit zone	(0.24/0.10)
f_{dw}	Detachment wave frequency, Hz	(2.28/2.03)
H_0	Work of adhesion, mJ m^{-2}	44
v_0	Characteristic crack speed, μm s^{-1}	0.1
α	Exponent	0.33

5.4 Concluding Remarks

The results obtained in this work allow us to draw the following conclusions:

1. Detachment waves persist in the presence of belt tensile cords; however, the pulley rotates steadier due to the increased stiffness of the composite belt. The detachment events are weaker (i.e, amplitude is smaller) and occur at higher frequencies.

2. Shear strain accumulates in the adhesion arc due to a speed differential between the belt contacting the pulley surface and the tensile cords, and is relaxed at the exit region by detachment waves. The new understanding of the shear relaxation by detachment waves requires a re-assessment of the Firbank's shear model – this is proposed as future work.

3. Compared with a regular flat belt, the frictional losses are smaller in both the driver and driven cases for corded belts.

CHAPTER 6. CONCLUSIONS

6.1 Summary

We explored mechanics of a soft-rigid rolling contact using a custom-built tribometer aimed at measuring the response of a prototypical belt drive system. We found for the first time that, under the slow speed considered, the relative displacement between the elastomeric belt and the pulley is achieved by means of cyclic detachment instead of sliding, which contradicts the current state of knowledge. We observed that the rolling contact mechanics is different in the driver and driven pulleys, and that contact instabilities associated with cyclic detachment are more evident and larger in scale in the driver case than in the driven case. In addition, we determined that contact instabilities manifesting as periodic detachment waves induce pulley oscillations, which grow in time. We also explored the detachment waves and pulley oscillations as functions of the applied torque, the operating speed, and the system moment of inertia. Increasing the applied torque accelerated the occurrence of the detachment waves in the driver case. A larger driving speed increased the frequencies of both the detachment waves and the pulley oscillations. Surprisingly, increasing the pulley's inertia could not remediate the contact instabilities, but resulted in larger fluctuations in the belt tension. This result was validated by a theoretical dynamic model of the system, which proved that detachment waves are the primary source for the system's self-oscillation.

To understand and evaluate the system's energy losses, we conducted an experimental and theoretical investigation into frictional mechanics of our model belt drive. A thorough stress analysis based on spatio-temporal measurements of the belt

tension, traction and contact area showed that the contact area evolution correlates to the shear traction changes, and that the contact arc region associated with relative displacement (traditionally called ‘slip’ arc) practically does not contribute to power transmission; this in contrast to the elastic creep and the belt shear theories. We also found that a significant difference between the belt traction observed in the driver and driven cases can be attributed to a unidirectional flow of power from the driver to the driven pulleys. Crosschecking, we developed a model considering both the bulk and surface hysteretic losses for predicting friction in the absence of sliding. This model showed that much higher mechanical losses in the driver case is due to the significant contribution of the detachment waves to the energy dissipation, and that the shear- and stretching-induced energy losses dominate in rolling friction for both the driver and driven cases.

Since the local contact instabilites and the global system’s self-oscillations are not desired in belt drives, we investigated the techniques of texturing of the belt contact surface, aiming to minimize disturbances associated with detachment waves. We found that although both regular and irregular surface topographies were useful in minimizing the belt drive vibrations, the regular ones provide a stronger effect and the effect is much more pronounced in the driver case than in the driven case due to different mechanisms for formation of detachment waves. Studying the effects of different texture characteristics, we showed that the aspect ratio of the pattern projections is the key design parameter, while the pattern shape and orientation, and the lattice constant are of practically no importance. We also demonstrated that excessive texturing leads to a decrease in the tractive capacities of the belt drive system.

Lastly, we studied the contact instabilities and frictional mechanics of the belts incorporating tensile cords, which resemble the commercial industrial belts. With the tensile cords included in the belt, the pulley rotated steadier due to the increased stiffness of the composite belt. However, the detachment waves were still present, which provides strong evidence that such detachment waves can be considered universal in soft rolling contact. In accordance with Firbank's shear model, we observed that the shear strain accumulated in the adhesion arc, resulting from the speed differential between the belt contacting the pulley surface and the tensile cords. However, in contrast to the shear model prediction, the accumulated shear strain was relaxed at the exit region, which undermines the validity of Firbank's model over the 'slip' arc, where detachment waves are generated. In addition, compared with a regular flat belt, the frictional losses were smaller in both the driver and driven cases for corded belts.

6.2 Research Contributions

The work presented in this dissertation makes the following original contributions:

1. We developed a second-to-none tribometer for capturing the contact instabilities and the global dynamic response in a prototypical belt drive system. This machine allowed us to describe, visualize and examine a few aspects of soft-rigid contact mechanics in belt drives, which were overlooked by several generations of mechanical engineers.

2. We found for the first time experimental evidence that, in a simple belt-drive system under low speed operation, the displacement between the belt and the pulley is accommodated primarily by detachment events rather than sliding. This calls into question

the universal validity of the sliding-based approach to analysis of rolling friction of elastomeric surfaces.

3. We showed that contact instabilities associated with detachment waves can serve as a sole source of self-oscillation in the belt drive system and that, counterintuitively, the problem cannot be resolved by manipulating the system's inertia. This finding will help in searching solutions for self-oscillation problems in other systems involving soft rolling motion, which is ubiquitous in countless engineering applications.

4. We proposed a new measurement approach and a new model for the estimation of the frictional losses in rolling motion incorporating detachment events. The proposed model may be applied to the calculation of the dissipated energy in other systems involving soft rolling contact.

5. We demonstrated that the novel biomimetic surface patterning design proposed earlier for the elimination of detachment waves in sliding can be successfully implemented in rolling as well. Use of this surface-modification approach may also be instrumental for better understanding and possible reduction of energy losses, noise pollution, vibration-induced inaccuracies, wear, etc. associated with dynamic effects in rolling.

6.3 Recommendations for Future Work

Despite we found for the first time that, for the low speed operation studied, the relative displacement between belt and pulley is achieved by means of cyclic detachment instead of sliding, it is still of great interest to investigate the contact instabilities at belt pulley interface under high speed operation. As the system runs at relatively high speed, the effect of the belt inertia will no longer be negligible, and the viscoelastic properties of the belt materials may change greatly. If the detachment waves still exist in the system,

which we highly believe in, the belt inertia and the viscoelasticity of the belt materials may play a more important role in affecting the detachment events. Additionally, we found that the pulley got rusty after it had been used for a long time (Fig. 6-1), which coincides with the well-known fact that rubber materials can actually wear its rigid counterpart under dynamic contacts. We believe the rust is due to the fretting wear caused by the cyclic detachment events at the interface. Hence, one can also explore the effect of the detachment events on the wear of the pulley.

Figure 6-1. Rust on the pulley due to the cyclic detachment events while in rolling contact with elastomer belts.

The current state-of-knowledge regarding the modeling of soft contact dynamics is still based on the 300-year-old concept of a coefficient of friction, which was developed to represent global frictional behavior of rigid rough surfaces. This concept ignores local stick-slip instabilities that represent an important source of excitation for any dynamic system involving friction. Hence, a first-principle friction model is needed to predict instabilities in soft rolling contact. On one hand, the phenomenological principles formulated by Amontons and Coulomb for rigid body friction should be abandoned. On the other hand, the modern perception of soft adhesive contact behavior should be introduced into the model for a thorough understanding of dynamics of rolling friction in soft-rigid interfaces. This will enable further progress in simulation of dynamic response

of multibody systems incorporating soft contact and will help to couple stochastic local contact instabilities with deterministic large-scale disturbances.

Three different approaches can be applied to the modeling of the sheared contact: (1) perfect slip (no shear is transmitted; Hertz contact model); (2) frictional slip (shear stress is proportional to normal stress, Coulomb model, or shear stress is proportional to shear yield strength; Tresca model); (3) perfect stick (no sliding is allowed, shear stress can grow infinitely). Hereafter, the possibility of coupling between adhesive separation and either perfect stick or Tresca frictional slip can be explored. This will allow modeling of local contact instabilities as well as associated global self-oscillation of the system.

Additionally, experiments are needed to identify local and global stability thresholds, and to assess the effectiveness and accuracy of the model to be developed. Automotive tires can be picked as the prototypical system of investigation given that it is a more general case of soft rolling contact compared to a belt drive system. If the tire contact scheme is chosen, a new experimental device will be needed for exploring frictional instabilities and for studying their effect on the global system dynamics. Herein, the digital image correlation (DIC) techniques can help to improve the resolution of strain measurements (Fig. 6-2).

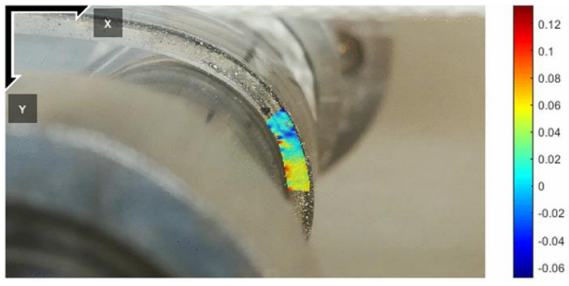

Figure 6-2. Shear strain at the sidewall of the belt measured using DIC.

One can also continue exploring the effects of adhesion, viscoelasticity, load, and speed on local contact instabilities and global system dynamics using different materials. It is of great significance to examine the capability of the model to predict experimental results and to assist in suggesting design changes that can lead to reduction in energy losses, noise pollution, loss of accuracy, wear, etc.

REFERENCES

[1] Zhang, S., and Xia, X., 2011, "Modeling and energy efficiency optimization of belt conveyors," Applied Energy, 88(9), pp. 3061-3071.

[2] Schallamach, A., 1971, "How does rubber slide?," Wear, 17(4), pp. 301-312.

[3] Johnson, K. L., 1987, Contact mechanics, Cambridge university press.

[4] Euler, M. L., 1762, "Remarques sur l'effect du frottement dans l'equilibre," Mémoires De l'Académie Royale Des Sciences, 18, pp. 265-278.

[5] Grashof, F., 1890, Theoretische Maschinenlehre, L. Voss, Leipzig.

[6] Fawcett, J., 1981, "Chain and belt drives, a review," Shock and Vibration Information Center The Shock and Vibration Digest, 13(5).

[7] Johnson, K. L., and Johnson, K. L., 1987, Contact mechanics, Cambridge university press.

[8] Bechtel, S., Vohra, S., Jacob, K., and Carlson, C., 2000, "The stretching and slipping of belts and fibers on pulleys," Journal of Applied mechanics, 67(1), pp. 197-206.

[9] Townsend, W., and Salisbury, J., 1988, "The efficiency limit of belt and cable drives," Journal of mechanisms, transmissions, and automation in design, 110(3), pp. 303-307.

[10] Leamy, M., and Wasfy, T., 2002, "Analysis of belt-driven mechanics using a creep-rate-dependent friction law," Journal of Applied Mechanics, 69(6), pp. 763-771.

[11] Oden, J., and Martins, J., 1985, "Models and computational methods for dynamic friction phenomena," Computer methods in applied mechanics and engineering, 52(1-3), pp. 527-634.

[12] Makris, N., and Constantinou, M., 1991, "Analysis of motion resisted by friction. II. Velocity-dependent friction∗," Journal of Structural Mechanics, 19(4), pp. 501-526.

[13] Firbank, T., 1970, "Mechanics of the belt drive," International Journal of Mechanical Sciences, 12(12), pp. 1053-1063.

[14] Gerbert, G., 1991, "Paper XII (i) On Flat Belt Slip," Tribology Series, 18, pp. 333-340.

[15] Gerbert, G., 1996, "Belt slip–a unified approach," Journal of Mechanical Design, 118(3), pp. 432-438.

[16] Alciatore, D., and Traver, A., 1995, "Multipulley belt drive mechanics: creep theory vs shear theory," Journal of Mechanical Design, 117(4), pp. 506-511.

[17] Kong, L., 2004, "Coupled belt-pulley mechanics in serpentine belt drives," The Ohio State University.

[18] Kong, L., and Parker, R. G., 2005, "Steady mechanics of belt-pulley systems," Journal of Applied Mechanics, 72(1), pp. 25-34.

[19] Kong, L., and Parker, R. G., 2005, "Microslip friction in flat belt drives," Proceedings of the Institution of Mechanical Engineers, Part C: Journal of Mechanical Engineering Science, 219(10), pp. 1097-1106.

[20] Kong, L., and Parker, R. G., 2006, "Mechanics and sliding friction in belt drives with pulley grooves," Journal of Mechanical Design, 128(2), pp. 494-502.

[21] Kong, L., and Parker, R. G., 2008, "Steady mechanics of layered, multi-band belt drives used in continuously variable transmissions (CVT)," Mechanism and Machine Theory, 43(2), pp. 171-185.

[22] Kim, D., Leamy, M. J., and Ferri, A. A., 2011, "Dynamic modeling and stability analysis of flat belt drives using an elastic/perfectly plastic friction law," Journal of Dynamic Systems, Measurement, and Control, 133(4), p. 041009.

[23] Wasfy, T. M., Wasfy, H. M., and Peters, J. M., "Prediction of the normal and tangential friction forces for thick flat belts using an explicit finite element code," Proc. ASME 2013 International Design Engineering Technical Conferences and Computers and Information in Engineering Conference, American Society of Mechanical Engineers, pp. V07AT10A070-V007AT010A070.

[24] Kim, D., Leamy, M., and Ferri, A., "Dynamic modeling of flat belt drives using the elastic-perfectly-plastic friction law," Proc. ASME 2009 International Design Engineering Technical Conferences and Computers and Information in Engineering Conference, American Society of Mechanical Engineers, pp. 483-491.

[25] Leamy, M., "Dynamics analysis of the time-varying operation of belt-drives," Proc. ASME 2003 International Design Engineering Technical Conferences and Computers and Information in Engineering Conference, American Society of Mechanical Engineers, pp. 399-408.

[26] Leamy, M., Barber, J., and Perkins, N., "Dynamics of belt/pulley frictional contact," Proc. IUTAM Symposium on Unilateral Multibody Contacts, Springer, pp. 277-286.

[27] Leamy, M. J., 2005, "On a perturbation method for the analysis of unsteady belt-drive operation," Journal of applied mechanics, 72(4), pp. 570-580.

[28] Leamy, M. J., and Wasfy, T. M., 2002, "Transient and steady-state dynamic finite element modeling of belt-drives," Journal of Dynamic Systems, Measurement, and Control, 124(4), pp. 575-581.

[29] Wasfy, T. M., and Leamy, M., "An object-oriented graphical interface for dynamic finite element modeling of belt-drives," Proc. ASME 2002 International Design Engineering Technical Conferences and Computers and Information in Engineering Conference, American Society of Mechanical Engineers, pp. 225-233.

[30] Wasfy, T. M., Yildiz, C., Wasfy, H. M., and Peters, J. M., 2016, "Effect of Flat Belt Thickness on Steady-State Belt Stresses and Slip," Journal of Computational and Nonlinear Dynamics, 11(5), p. 051005.

[31] Makris, N., and Constantinou, M., 1991, "Analysis of Motion Resisted by Friction. I. Constant Coulomb and Linear/Coulomb Friction∗," Journal of Structural Mechanics, 19(4), pp. 477-500.

[32] Meckstroth, R. J., Wasfy, T. M., and Leamy, M. J., 2004, "Finite element study of dynamic response of serpentine belt-drives with isolator clutches," No. 0148-7191, SAE Technical Paper.

[33] Leamy, M. J., and Wasfy, T. M., 2005, "Time-accurate finite element modelling of the transient, steady-state, and frequency responses of serpentine and timing belt-drives," International journal of vehicle design, 39(3), pp. 272-297.

[34] Leamy, M., Barber, J., and Perkins, N., 1998, "Distortion of a harmonic elastic wave reflected from a dry friction support," Journal of applied mechanics, 65(4), pp. 851-857.

[35] Leamy, M. J., and Wasfy, T. M., "Dynamic finite element modeling of belt-drives including one-way clutches," Proc. ASME 2001 Int Mech Eng Congress and Exposition.

[36] Gerbert, B. G., 1999, Traction Belt Mechanics: Flat belts, V-belts, V-rib belts, Machine and Vehicle Design, Chalmers University of Technology [Institutionen ….

[37] Ward, I. M., and Sweeney, J., 2012, Mechanical properties of solid polymers, John Wiley & Sons.

[38] Chen, T., Lee, D., and Sung, C.-K., 1998, "An experimental study on transmission efficiency of a rubber V-belt CVT," Mechanism and machine theory, 33(4), pp. 351-363.

[39] De Almeida, A., and Greenberg, S., 1995, "Technology assessment: energy-efficient belt transmissions," Energy and buildings, 22(3), pp. 245-253.

[40] Manin, L., Michon, G., Remond, D., and Dufour, R., 2009, "From transmission error measurement to pulley–belt slip determination in serpentine belt drives: Influence of tensioner and belt characteristics," Mechanism and Machine Theory, 44(4), pp. 813-821.

[41] Čepon, G., Manin, L., and Boltežar, M., 2010, "Experimental identification of the contact parameters between a V-ribbed belt and a pulley," Mechanism and Machine Theory, 45(10), pp. 1424-1433.

[42] Balta, B., Sonmez, F. O., and Cengiz, A., 2015, "Speed losses in V-ribbed belt drives," Mechanism and Machine Theory, 86, pp. 1-14.

[43] Silva, C. A., Manin, L., Rinaldi, R. G., Remond, D., Besnier, E., and Andrianoely, M.-A., 2018, "Modeling of power losses in poly-V belt transmissions: Hysteresis phenomena (enhanced analysis)," Mechanism and Machine Theory, 121, pp. 373-397.

[44] Manin, L., Lorenzon, C., and Liang, X., "Power losses prediction in poly-v belt transmissions: application to front engine accessory drives," Proc. International Gear Conference 2014, Woodhead publishing, pp. pp. 1162-1171.

[45] Grosch, K. A., 1963, "Relation between friction and visco-elastic properties of rubber," Nature, 197(487), p. 858.

[46] Kummer, H. W., 1966, Unified Theory of Rubber and Tire Friction, Pennsylvania State University.

[47] Kluppel, M., and Heinrich, G., 2000, "Rubber friction on self-affine road tracks," Rubber Chemistry and Technology, 73(4), pp. 578-606.

[48] Golden, J. M., 1975, "A molecular theory of adhesive rubber friction," Journal of Physics A-Mathematical and General, 8(6), pp. 966-979.

[49] Ludema, K. C., and Tabor, D., 1966, "The friction and visco-elastic properties of polymeric solids," Wear, 9(5), pp. 329-348.

[50] Persson, B. N. J., 1998, "On the theory of rubber friction," Surf Sci, 401(3), pp. 445-454.

[51] Rabinowicz, E., 1958, "The intrinsic variables affecting the stick-slip process," P Phys Soc Lond, 71(460), pp. 668-675.

[52] Best, B., Meijers, P., and Savkoor, A. R., 1981, "The Formation of Schallamach Waves," Wear, 65(3), pp. 385-396.

[53] Barquins, M., and Roberts, A. D., 1986, "Rubber-friction variation with rate and temperature – some new observations," Journal of Physics D-Applied Physics, 19(4), pp. 547-563.

[54] Rand, C. J., and Crosby, A. J., 2006, "Insight into the periodicity of Schallamach waves in soft material friction," Appl Phys Lett, 89(26), p. Artn 261907.

[55] Fukahori, Y., Gabriel, P., and Busfield, J. J. C., 2010, "How does rubber truly slide between Schallamach waves and stick-slip motion?," Wear, 269(11-12), pp. 854-866.

[56] Lindner, M., Kröger, M., and Popp, K., 2001, "Stick-slip vibrations of pneumatic seals," Machine Dynamics Problems, 25(3/4), pp. 121-130.

[57] Sheng, G., Lee, J. H., Narravula, V., and Song, D., 2011, "Experimental characterization and analysis of wet belt friction and the vibro-acoustic behavior," Tribology International, 44(3), pp. 258-265.

[58] Barquins, M., 1985, "Sliding friction of rubber and Schallamach waves—a review," Materials Science and Engineering, 73, pp. 45-63.

[59] Wu-Bavouzet, F., Clain-Burckbuchler, J., Buguin, A., De Gennes, P.-G., and Brochard-Wyart, F., 2007, "Stick-slip: Wet versus dry," The Journal of Adhesion, 83(8), pp. 761-784.

[60] Viswanathan, K., Mahato, A., and Chandrasekar, S., 2015, "Nucleation and propagation of solitary Schallamach waves," Physical Review E, 91(1), p. 012408.

[61] Maegawa, S., Itoigawa, F., and Nakamura, T., 2015, "Effect of normal load on friction coefficient for sliding contact between rough rubber surface and rigid smooth plane," Tribology international, 92, pp. 335-343.

[62] Maegawa, S., Itoigawa, F., and Nakamura, T., 2016, "Dynamics in sliding friction of soft adhesive elastomer: Schallamach waves as a stress-relaxation mechanism," Tribology International, 96, pp. 23-30.

[63] Yamaguchi, T., Ohmata, S., and Doi, M., 2009, "Regular to chaotic transition of stick–slip motion in sliding friction of an adhesive gel-sheet," Journal of Physics: Condensed Matter, 21(20), p. 205105.

[64] Czichos, H., 2009, Tribology: a systems approach to the science and technology of friction, lubrication, and wear, Elsevier.

[65] Romero-Sánchez, M. a. D., Pastor-Blas, M. M., and Martín-Martínez, J. M., 2001, "Adhesion improvement of SBR rubber by treatment with trichloroisocyanuric acid solutions in different esters," International Journal of Adhesion and Adhesives, 21(4), pp. 325-337.

[66] Mittal, K. L., 2004, Polymer Surface Modification: Relevance to Adhesion, Volume 3, CRC Press.

[67] Liu, C., Cui, N., Brown, N. M., and Meenan, B. J., 2004, "Effects of DBD plasma operating parameters on the polymer surface modification," Surface and Coatings Technology, 185(2-3), pp. 311-320.

[68] Noeske, M., Degenhardt, J., Strudthoff, S., and Lommatzsch, U., 2004, "Plasma jet treatment of five polymers at atmospheric pressure: surface modifications and the relevance for adhesion," International journal of adhesion and adhesives, 24(2), pp. 171-177.

[69] Paulussen, S., Rego, R., Goossens, O., Vangeneugden, D., and Rose, K., 2005, "Plasma polymerization of hybrid organic–inorganic monomers in an atmospheric pressure dielectric barrier discharge," Surface and Coatings Technology, 200(1-4), pp. 672-675.

[70] Verheyde, B., Rombouts, M., Vanhulsel, A., Havermans, D., Meneve, J., and Wangenheim, M., 2009, "Influence of surface treatment of elastomers on their frictional behaviour in sliding contact," Wear, 266(3-4), pp. 468-475.

[71] Etsion, I., Kligerman, Y., and Halperin, G., 1999, "Analytical and experimental investigation of laser-textured mechanical seal faces," Tribology Transactions, 42(3), pp. 511-516.

[72] Shinkarenko, A., Kligerman, Y., and Etsion, I., 2009, "The effect of elastomer surface texturing in soft elasto-hydrodynamic lubrication," Tribology Letters, 36(2), pp. 95-103.

[73] Verberne, G., Schroeder, A., Halperin, G., Barenholz, Y., and Etsion, I., 2010, "Liposomes as potential biolubricant additives for wear reduction in human synovial joints," Wear, 268(7-8), pp. 1037-1042.

[74] Gorb, S. N., 2009, Functional surfaces in biology: little structures with big effects, Springer Science & Business Media.

[75] Hanna, G., Jon, W., and Barnes, W. J., 1991, "Adhesion and detachment of the toe pads of tree frogs," Journal of Experimental Biology, 155(1), pp. 103-125.

[76] Gorb, S., Jiao, Y., and Scherge, M., 2000, "Ultrastructural architecture and mechanical properties of attachment pads in Tettigonia viridissima (Orthoptera Tettigoniidae)," Journal of Comparative Physiology A, 186(9), pp. 821-831.

[77] Scherge, M., Gorb, S. N., and Gorb, S., 2001, Biological micro-and nanotribology, Springer Science & Business Media.

[78] Barnes, W. J. P., Goodwyn, P. J. P., Nokhbatolfoghahai, M., and Gorb, S. N., 2011, "Elastic modulus of tree frog adhesive toe pads," Journal of Comparative Physiology A, 197(10), p. 969.

[79] Federle, W., Barnes, W., Baumgartner, W., Drechsler, P., and Smith, J., 2006, "Wet but not slippery: boundary friction in tree frog adhesive toe pads," Journal of the Royal Society Interface, 3(10), pp. 689-697.

[80] Ohler, A., 1995, "Digital pad morphology in torrent-living ranid frogs," Asiatic Herpetological Research, 6, pp. 85-96.

[81] Murarash, B., Itovich, Y., and Varenberg, M., 2011, "Tuning elastomer friction by hexagonal surface patterning," Soft Matter, 7(12), pp. 5553-5557.

[82] Tsipenyuk, A., and Varenberg, M., 2014, "Use of biomimetic hexagonal surface texture in friction against lubricated skin," Journal of the Royal Society Interface, 11(94), p. 20140113.

[83] Varenberg, M., and Gorb, S. N., 2009, "Hexagonal surface micropattern for dry and wet friction," Advanced Materials, 21(4), pp. 483-486.

[84] Chen, H., Zhang, L., Zhang, D., Zhang, P., and Han, Z., 2015, "Bioinspired surface for surgical graspers based on the strong wet friction of tree frog toe pads," ACS applied materials & interfaces, 7(25), pp. 13987-13995.

[85] Gupta, R., and Frechette, J., 2012, "Measurement and scaling of hydrodynamic interactions in the presence of draining channels," Langmuir, 28(41), pp. 14703-14712.

[86] Iturri, J., Xue, L., Kappl, M., García‐Fernández, L., Barnes, W. J. P., Butt, H. J., and del Campo, A., 2015, "Torrent frog‐inspired adhesives: attachment to flooded surfaces," Advanced Functional Materials, 25(10), pp. 1499-1505.

[87] Rand, C. J., and Crosby, A. J., 2009, "Friction of soft elastomeric wrinkled surfaces," Journal of Applied Physics, 106(6), p. 064913.

[88] Varenberg, M., and Gorb, S., 2007, "Shearing of fibrillar adhesive microstructure: friction and shear-related changes in pull-off force," Journal of The Royal Society Interface, 4(15), pp. 721-725.

[89] Kligerman, Y., and Varenberg, M., 2014, "Elimination of stick-slip motion in sliding of split or rough surface," Tribol. Lett., 53(2), pp. 395-399.

[90] Evensen, H., Jiang, H., Gotrik, K., Denes, F., and Carpick, R., 2009, "Transformations in wrinkle patterns: cooperation between nanoscale cross-linked surface layers and the submicrometer bulk in wafer-spun, plasma-treated polydimethylsiloxane," Nano letters, 9(8), pp. 2884-2890.

[91] Smith, D. P., 1998, "Tribology of the belt-driven data tape cartridge," Tribology international, 31(8), pp. 465-477.

[92] Varenberg, M., and Varenberg, A., 2012, "Table tennis rubber: tribological characterization," Tribology Letters, 47(1), pp. 51-56.

[93] Varenberg, M., and Tsipenyuk, A., 2014, "Testing peel adhesion of flexible films: banknote substrates," Journal of Adhesion Science and Technology, 28(6), pp. 630-634.

[94] Barquins, M., and Courtel, R., 1975, "Rubber friction and the rheology of viscoelastic contact," Wear, 32(2), pp. 133-150.

[95] Kendall, K., 1975, "Rolling friction and adhesion between smooth solids," Wear, 33(2), pp. 351-358.

[96] Hutchings, I., and Shipway, P., 2017, Tribology: Friction and Wear of Engineering Materials, Butterworth-Heinemann.

[97] Barquins, M., Maugis, D., Blouet, J., and Courtel, R., 1978, "Contact area of a ball rolling on an adhesive viscoelastic material," Wear, 51(2), pp. 375-384.

[98] Lin, T. R., Farag, N. H., and Pan, J., 2005, "Evaluation of frequency dependent rubber mount stiffness and damping by impact test," Applied Acoustics, 66(7), pp. 829-844.

[99] Lin, I.-K., Ou, K.-S., Liao, Y.-M., Liu, Y., Chen, K.-S., and Zhang, X., 2009, "Viscoelastic characterization and modeling of polymer transducers for biological applications," Journal of Microelectromechanical systems, 18(5), pp. 1087-1099.

[100] Meyers, M. A., and Chawla, K. K., 2008, Mechanical behavior of materials, Cambridge university press.

[101] Greenwood, J., 2004, "The theory of viscoelastic crack propagation and healing," Journal of Physics D: Applied Physics, 37(18), p. 2557.

[102] Emerson, J. A., OToole, E., Zamora, D., and Poon, B., 1998, "Comparison of three work of adhesion measurements," Sandia National Labs., Albuquerque, NM (United States).

[103] Varenberg, M., and Gorb, S. N., 2009, "Hexagonal surface micropattern for dry and wet friction," Adv. Mater., 21(4), pp. 483–486.

[104] Gorb, S. N., 2007, "Visualisation of native surfaces by two-step molding," Microsc. Today, 15, pp. 44-46.

[105] Della Pietra, L., and Timpone, F., 2013, "Tension in a flat belt transmission: experimental investigation," Mechanism and Machine Theory, 70, pp. 129-156.

[106] He, B., Chen, W., and Wang, Q. J., 2008, "Surface texture effect on friction of a microtextured poly (dimethylsiloxane)(PDMS)," Tribology Letters, 31(3), p. 187.

[107] Kharkova, G., Kononova, O., Krasnikovs, A., Eiduks, M., Machanovskis, E., and Dzelzitis, K., 2011, "Elastic properties of cotton fabric based polymer composities," Engineering for Rural Development (Latvia).